IFT

Instituto de Física Teórica
Universidade Estadual Paulista

DISSERTAÇÃO DE MESTRADO IFT–D.007/16

Electronic structure of two dimensional systems with spin-orbit interaction

Armando Arquimedes Pezo Lopez

Orientador

Dr. Alexandre Reily Rocha

Julho de 2016

Acknowledgments

I would like to start expressing my gratefulness to my advisor Alexandre, from whom I learned many things in the last two years, and who always was able to share his knowledge. He seems to be always aware of the current developments in the field which is something very valuable in this business.

I thank my family, mother and sisters, for the support, the work and sacrifice they made, this is really helpful when one needs to accomplish something. I'd also like to thank Getulio, Lesli and Juliano for the warm and very kind treatment I received from them in moments when I was fully invaded by dubiety.

In the IFT, I'd like to thank the members of the group, for the comments and suggestions they made all along this road that finally ends in this monograph. I also want to thank to the technical staff, in particular to the Seção de Pós-Graduação.

This work was supported by CAPES – Brazilian Federal Agency for Support and Evaluation of Graduate Education within the Ministry of Education of Brazil. I also want to thank to the Institutions where the calculations were performed, these were the HPC clusters at the Universidade Estadual Paulista (UNESP) and Instituto de Fisica-USP.

This dissertation is dedicated to Ge and Mari.

Resumo

A realização experimental do grafeno em 2004 abriu as portas para os estudos de uma nova geração de materiais, estes chamados materiais bidimensionais são a expressão final do que poderíamos pensar em material plano (monocamada) que, eventualmente, podem ser empilhados para formar o bulk.

O grafeno oferece uma grande variedade de propriedades físicas, em grande parte, como o resultado da dimensionalidade de sua estrutura, e pelas mesmas razões, materiais como Fosforeno (P), Siliceno (S), Nitreto de Boro hexagonal (hBN), dicalcogenos de metais de transição (TMDC), etc. São muito interessantes para fins teóricos, como para futuras aplicações tecnológicas que podem-se desenvolver a partir deles, como dispositivos de spintrônica e armazenamento.

Neste trabalho o estudo desenvolvido são as propriedades eletrônicas dos materiais apresentados acima (grafeno, fosforeno e $\mathrm{MoTe_2}$), e além disso, ja que o acoplamento spin-órbita aumenta à medida que o número atômico faz, espera-se que este parâmetro desempenhe um papel na estrutura eletrônica, particularmente para os TMDC's. Começamos descrevendo genéricamente esses três sistemas, isto é, para o grafeno, podemos usar uma abordagem tipo *tight binding*, a fim de encontrar a dispersão de energia para as quaseparticulas perto do nível de Fermi (Equação de Dirac). Usando cálculos DFT estudou-se de forma geral as propriedades desses sistemas com a inclusão do espin órbita.

Abordou-se cálculos para descrever os efeitos do acoplo spin órbita sobre os materiais isolados, tambem nas heterostruturas (duas camadas formadas por eles). Finalmente, tambem estudou-se a possibilidade de defeitos e sua possível influência sobre a estrutura eletrônica das heterostruturas.

Palavras Chaves: Grafeno, Fosforeno, Dichalcogenides de metais de transição, Sistemas Bidimensionais, Acoplamento Spin-orbita, Defeitos em Grafeno, Teoria Funcional da Densidade.

Áreas do conhecimento: Fisica da Matéria condensada.

Abstract

The experimental realization of graphene in 2004 opened the gates to the studies of a new generation of materials, these so-called 2 dimensional materials are the final expression of what we could think of a plane material (monolayer) that eventually can be stacked to form a bulk.

Graphene, the wonder material, offers a large variety of physical properties, in great part, as the result of the dimensionality of its structure, and for the same reasons, materials like phosphorene(P), silicene(S), hexagonal Boron Nitride (hBN), transition metal dichalcogenides(TMDC), etc. are very interesting for theoretical purposes, as for the future technological applications that we can develope from them, such as Spintronics and Storage devices.

In this dissertation we theoretically study the electronic properties of the materials presented above (graphene, Phosphorene and $\mathrm{MoTe_2}$), and besides that, since the spin-orbit coupling strength increases as the atomic number does, we expect that this paremeter plays a role in the electronic structure, particularly for the TMDC. We start describing generically those three systems using density functional theory including the effect of spin orbit.
We address calculations to describe the effects of spin orbit on the isolated materials as well as the heterostructures. Finally we also include the possibility of defects in graphene and their possible influence on the electronic structure of heterostructures.

Keywords: Graphene, Phosphorene, Transition Metal Dichalcogenides, Bidimensional systems, Spin-Orbit Coupling, Defects in graphene, Density Functional Theory.

Contents

List of Figures

List of Tables

Chapter 1

Introduction

The characterization of materials deals with many parameters and properties, being the dimensionality of the system one of the determinant points taken for such a procedure. The arrival of new technologies enhances the possibility of discovery and latter production of new kind of materials, this is what happened with graphene [2], the first 2 dimensional material synthesized in laboratory. For a long time it was believed that the realization of 2D materials was not possible. Theoreticians working in that subject like Landau [3] and Peierls [4] argued that any 2D crystal was thermodynamically unstable. It was not until 2004 when Andre Geim and Kostya Novoselov from Manchester University were able to isolate a graphene sheet containing a single layer of Carbon atoms using the so-called "Scotch tape" method. This achievement resulted in the Physics Nobel prize in 2010 [7].

The discovery of graphene, however, was just the beginning of the story related to these 2 dimensional materials. In fact, since its discovery a number of other 2D materials have been shown to exist such as Boron nitride [2] and more recently the transition metal dichalcogenides (TDMCs) [54]. In the latter case one has, not exactly, a single layer, but a three-layered material formed by a layer of transition metal atoms (usually Mo) sandwiched between two layers of atoms from the chalcogenide family (S, Se, Te) [54]. Finally, a material that was studied in the 1980's in bulk form has also staged a come back in two-dimensions; black Phosphorus has a strong layer dependent gap with possible uses in optoelectronics [45].

In parallel with the efforts on truly one-sheet systems, another research field has recently emerged and has been showing interesting results over the last three or four years. This new field deals with heterostructures and devices made by stacking different 2D crystal on top of each other. The idea is indeed very simple: taking monolayers and sticking them one upon the other in such a way that resembles a Lego game [13]. Strong covalent bonds provide in-plane stability of the 2D crystal whereas relatively weak van der Waals-like forces are sufficient to keep them together. The existence of such a system was demonstrated experimentally and has been reported [52,61]. Then we have the whole picture now, we'll try to obtain properties in 2D materials from a simple graphene mono-layer to a bilayer structure consisting in one graphene monolayer with defect and on top of it a monolayer of $MoTe_2$ or phosphorene.

At that same time graphene was discovered, experiments related to the quest for the so-called intrinsic spin Hall effect in semiconductors were proficient in demonstrating that it was possible to use a new degree of freedom for condensed matter systems, namely, the electron's spin [5]. The effects related to the inclusion of the spin-orbit coupling (SOC) made it then a natural choice to bring such a possibility and became one important aspect in this new branch of physics called spintronics [51]. Since the magnitude of the spin-orbit coupling increases with the atomic number, it consequently provides negligible contributions to the electronic structure in *light* systems such as the same graphene, contrary to materials with heavier atoms, for instance $3d$ ferromagnetic materials, where the impact is significant. It's responsible for magnetic anisotropies of the order of 10 to 100 μeV in bcc and fcc Fe, Ni and Co and it is also the primary interaction which gives rise for the most of the zero field splitting and other properties of magnetic molecules [12]. As it will be shown for the case of transition metal dichalcogenides (TMDC), spin-orbit interaction spin-splits the edges of the valence and conduction bands and then allows the electrical manipulation of the spin degree of freedom [63].

With all this in mind it is important to understand; in materials design, the effects of spin-orbit coupling in different 2D materials and some of their heterostructures.

Furthermore, as defects are ubiquitously present in large scale graphene, it is also interesting to address such issues as well. These are topics which will be covered in this dissertation.

This dissertation is structured as follows, in chapter 2, I will present a review on the properties of the isolated systems as well as the results of very recent works related to the effects obtained from some heterostructure systems. These have been thoroughly studied by others and I will go over the highlights these works reported. In chapter 3, I will present the methodology used for the calculations, namely density functional theory (DFT) with particular focus on spin-orbit effects. In chapter 4, I will show the results of this work and finally for chapter 5, I'll give my comments and conclusions.

Chapter 2

2D Materials

In this work we will focus on three different materials, namely: graphene, phosphorene and $MoTe_2$. Each of them shows peculiarities in their electronic structures that have been separately studied. In what follows I will discuss some of their properties.

2.1 Graphene

Carbon is one of the most abundant materials on earth and is of main importance for the description of biological systems and organic Chemistry. Due to its electronic properties (electronic configuration), it shows a large number of so called allotropes with equally numerous physical properties, some of these allotropes can be viewed in Fig. 2.1: graphene, graphite, carbon nanotube and fullerene. As it was mentioned before, the dimensionality of these structures is one of the reasons for those particular properties. Among all of them, Graphene, a truly 2-dimensional system, plays an important role for the understanding of the electronic properties in other allotropes [8].

Graphene is made out of a hexagonal honeycomb arrangement of carbon atoms, which can be visualized in Fig. 2.2. Graphite, a three dimensional allotrope of carbon, is a widely known material which is the result of the stacking of graphene monolayers bound to each other as the result of the van der Waals forces[6]. Even though graphite is abundant and widely known, its monolayer counterpart was only isolated

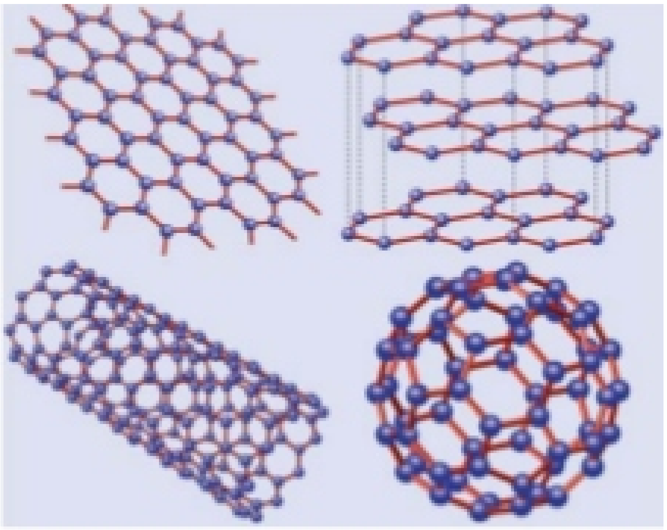

Figure 2.1: Allotropes of carbon: Graphene, Graphite ,carbon nanotube and fullerene.

(or perhaps noticed) 440 years after the invencion of pencils (made of graphite). This might be because, first of all, no one expected graphene to exist in its free form and even existed, there were no tools to search for one-atom-thick flakes among graphite debris covering macroscopic areas. Graphene can be considered as the precursor of the other structures shown in Fig. 2.1 as different arrangements (or cuttings) can lead to he other ones.

The flexibility of graphene is reflected on its electronic properties. The sp^2 hybridization between the s orbital and the two p orbitals leads to a trigonal planar structure with the formation of a σ bond between carbon atoms with a separation of approximately $1.42\mathring{A}$ [8], these bondings are responsible for the robustness of the carbon allotropes. In the electronic band structure, this bands belong to the deep part in the valence band. However, the other p orbital, which is perpendicular to the plane of the sheet, can bind covalently with neighboring carbom atoms, leading to the formation of a π band. Since every p orbital has one extra electron, the π band is half filled.

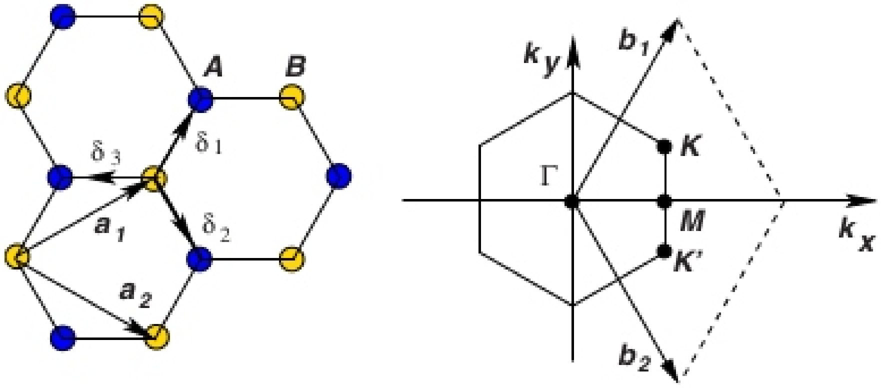

Figure 2.2: Graphene Honeycomb structure lattice and reciprocal lattice.

One of the most interesting aspects of Graphene is that its low-energy excitations are massless Dirac fermions. Dirac (massless) fermions behave in unusual ways when compared to ordinary electrons if subjected to magnetic fields, leading to unexpected phenomena such as the anomalous quantum Hall effect, which because of the large cyclotron energies, can be observed at room temperature [9]. Other curious effects that have been reported in this system are the Klein paradox and *Zitterbewegung*, such effects make graphene immune to localization effects, resulting in the large distances that can be covered by conduction electrons without scattering(μm) [10].

In order to simulate the low energy excitations of graphene, we can use a *tight binding* model and afterwards look for the spectrum in the whole Brillouin Zone. The hexagonal structure can bee seen as a superposition of two triangular sublattices, where the Carbon atoms are denoted in each sublattice as A (blue) and B (yellow) as shown if Fig. 2.2. Writing down the lattice vectors

$$\vec{a}_1 = \frac{a}{2}(3, \sqrt{3}), \quad \vec{a}_2 = \frac{1}{2}(3, -\sqrt{3}), \tag{2.1}$$

where a denotes the lattice parameter(carbon-carbon bond), then the reciprocal lattice vectors are given by [11]

$$\vec{b}_1 = \frac{2\pi}{3a}(1, \sqrt{3}), \quad \vec{b}_2 = \frac{2\pi}{3a}(1, -\sqrt{3}) \tag{2.2}$$

Looking at the Brillouin zone we can recognize two important points; the inequivalent K and K' points. They are at the corners of the Brillouin zone and because the linear dispersion takes place in those two points they are known as Dirac points. Setting the reference as before, we can write the coordinates of these points as

$$\vec{K} = (\frac{2\pi}{3a}, \frac{2\pi}{3\sqrt{3}a}), \quad \vec{K}' = (\frac{2\pi}{3a}, -\frac{2\pi}{3\sqrt{3}a}) \tag{2.3}$$

Taking the nearest neighbours and the second nearest neighbours, the Tight Binding Hamiltonian is given by

$$H = -t \sum_{<i,j>,\sigma} (a^{\dagger}_{\sigma,i} b_{\sigma,j} + H.c.) - t' \sum_{\ll i,j \gg,\sigma} (a^{\dagger}_{\sigma,i} a_{\sigma,j} + b^{\dagger}_{\sigma,i} b_{\sigma,j} + h.c.) \tag{2.4}$$

where the operator a (b) acts as a creation and $a^{\dagger}$ ($b^{\dagger}$) as an annihilation operator on positions $\vec{R}$ of the sublattice $A(B)$ with spin σ, with hopping t for nearest neighbours($< i, j >$) and t' as hopping for second nearest neighbours($\ll i, j \gg$). The solution of this two band model give the eigenvalues:

$$E_{\pm}(\vec{k}) = \pm\sqrt{3 + t^2 f(\vec{k})} - t' f(\vec{k}), \tag{2.5}$$

where

$$f(\vec{k}) = 2cos(\sqrt{3}k_y a) + 4cos(\frac{\sqrt{3}}{2}k_y a)cos(\frac{3}{2}k_x a), \tag{2.6}$$

Here the plus sign corresponds the upper band (π') and the minus sign is for the lower band (π), where can be seen that t' breaks the "particle-hole" symmetry and makes the band asymmetric around the zero energy. However, at low energies we can verify the linear dispersion about the zero point. Taking $\vec{k} = \vec{K} + \vec{q}$, and making an expansion around that K point (same for K'), we find the dispersion with little $\vec{q}$

$$E_{\pm}(\vec{q}) \simeq \pm v_F|\vec{q}| + O[(q/K)^2] \tag{2.7}$$

$\vec{q}$ is the momentum measured from the Dirac points and v_F is the Fermi velocity which is dependent on the system parameters. We also can obtain the energy values from second order expansion as

$$E_{\pm}(\vec{q}) \simeq 3t' \pm v_F|\vec{q}| - (\frac{9t'a^2}{4} \pm \frac{3ta^2}{8} sin(3\theta_{\vec{q}}))q^2 \tag{2.8}$$

where

$$\theta_{\vec{q}} = arctan(\frac{q_x}{q_y}) \tag{2.9}$$

In Fig. 2.3 the Electronic band structure all along the first Brillouin zone calculated using a tight binding Hamiltonian. There are the six points, the so-called Dirac points where the conduction and valence bands touch each other.

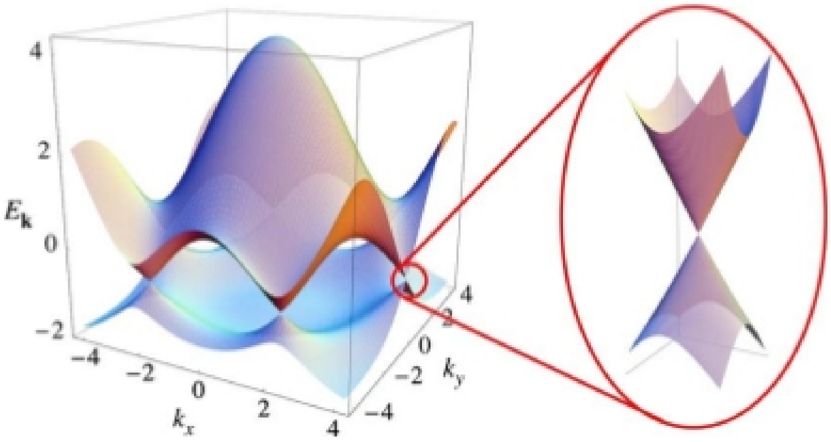

Figure 2.3: Graphene Electronic Band Structure near the Fermi Energy.

In addition in Fig. 2.4 we also present a plot of the band structure and Density of states using a more precise ab initio methods including more bands. There we can note the existence of just one orbital near the Fermi energy and the band resembles the obtained using the simpler Hamiltonian.

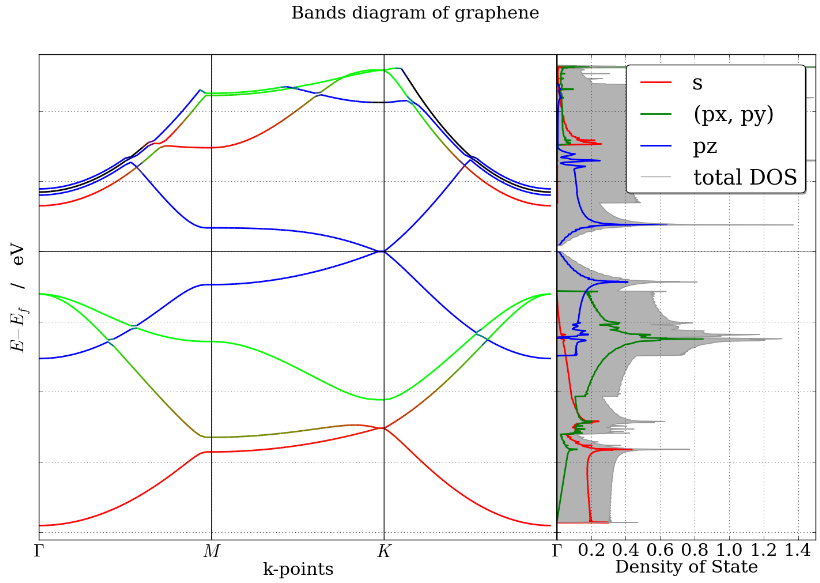

Figure 2.4: Ab initio Graphene's Electronic Band structure and PDOS [16].

If we take the TB Hamiltonian with $t' = 0$ and we Fourier transform the electron operators,

$$a_n = \frac{1}{\sqrt{N}} \sum_{\vec{k}} e^{-i\vec{k}\cdot\vec{R_n}} a(\vec{k}), \tag{2.10}$$

where N is the number of unit cells, and perform the same Fourier transformation around the K and K' points we can reproduce the previous fields(for each sublattice) as a superposition of two new fields, given by

$$a_n \simeq e^{-i\vec{K}\cdot\vec{R_n}} a_{1,n} + e^{-i\vec{K'}\cdot\vec{R_n}} a_{2,n}, \tag{2.11}$$

$$b_n \simeq e^{-i\vec{K}\cdot\vec{R_n}} b_{1,n} + e^{-i\vec{K'}\cdot\vec{R_n}} b_{2,n}, \tag{2.12}$$

Here the index $i = 1, 2$ refers to the points K and K', or the valley degree of freedom, and we assume that these fields vary smoothly over the unit cell. With this,we replace the fields in the tight binding Hamiltonian and expand the operators up to a linear order in δ, taking into account that $\sum_{\vec{\delta}} e^{\pm i\vec{K}\cdot\delta} = 0$ (this also happens for the K' point), obtaining

$$H \simeq -iv_F \int dxdy[\hat{\Psi}_1^\dagger(\vec{r})\vec{\sigma} \cdot \nabla\hat{\Psi}_1(\vec{r}) + \hat{\Psi}_2^\dagger(\vec{r})\vec{\sigma}^* \cdot \nabla\hat{\Psi}_2(\vec{r})] \tag{2.13}$$

where $\vec{\sigma} = (\sigma_x, \sigma_y)$, $\vec{\sigma}^* = (\sigma_x, -\sigma_y)$ and $\hat{\Psi}_i^\dagger = (a_i^\dagger, b_i^\dagger)$ for $i = 1, 2$. The two component electron wave function $\psi(\vec{r})$ thus, obeys the 2D Dirac equation

$$-iv_F\vec{\sigma} \cdot \nabla\psi(\vec{r}) = E\psi(\vec{r}). \tag{2.14}$$

In momentum space, the wave function around these inequivalent points is written as

$$\psi_{\pm,\vec{K}}(\vec{k}) = \frac{1}{2}\begin{pmatrix} e^{-i\theta_{\vec{k}}/2} \\ \pm e^{i\theta_{\vec{k}}/2} \end{pmatrix} \tag{2.15}$$

where the angle in the reciprocal space was defined before, the Hamiltonian is given by $H_K = v_F\vec{\sigma} \cdot \vec{k}$, and the signs correspond to the signs of the energies, or in other words as before, for the valence and conduction bands.

Around the K' point the wave function is

$$\psi_{\pm,\vec{K'}}(\vec{k}) = \frac{1}{2}\begin{pmatrix} e^{i\theta_{\vec{k}}/2} \\ \pm e^{-i\theta_{\vec{k}}/2} \end{pmatrix} \tag{2.16}$$

and the Hamiltonian is $H_K = v_F\vec{\sigma}^* \cdot \vec{k}$, note that K and K' are related by time reversal symmetry, that is, if we set the origin in the middle point between those inequivalent points-the M point-time reversal becomes equivalent to a reflection along the k_x axis, $(k_x, k_y) \to (k_x, -k_y)$, and from the definition of the wave 2-component functions , if the phase θ is rotated by 2π, the wave function changes sing indicating a phase of π (Berry's phase), this change of phase by π under rotation is characteristic of spinors.

There is another quantity that can be used to characterize the eigenfunctions which is the helicity, defined as the projection of the momentum operator along the (pseudo)spin direction, this operator has the following form

$$\hat{h} = \frac{1}{2}\vec{\sigma} \cdot \frac{\vec{p}}{p} \tag{2.17}$$

where p is the momentum norm. For the definition of this operator we can see that both functions in those two Dirac points are eigenstates of the helicity operator, and the eigenvalues have opposite signs. This means that near the Dirac point, these states have well defined *chirality* or helicity, which is a good quantum number as long as the Hamiltonian written above is valid. Thus, strictly speaking, we cannot obtain the same result for larger energies or if we include a second nearest neighbour hopping. The chirality of electrons in graphene leads to a peculiar modification of the Quantum Hall effect, and plays a role in phase-coherent phenomena such as weak localization [18].

2.1.1 Defects in Graphene

Disorder or defects are present in actual materials [20], then we can expect their existence in Graphene. As a matter of fact, true long-range order in $2D$ implies a broken continuous symmetry(translation), which violates the *Hohenberg-Mermim-Wagner* theorem [22,23], thus from this argument alone, one might expect some form of disorder to stabilize Graphene.

The potential effects of defects in carbon-based systems have been studied by theory in the last decade [24,25], predicting new functional properties like the opening gap at Dirac points, or aiming to explain the magnetic ordering observed in defective Graphene [26].

In fact Esquinazi et al [27], showed that when orientated pyrolytic graphite (HOPG) samples were irradiated by high energy proton beams, the samples acquired a magnetic moment, displaying long range ferromagnetic order up to temperatures above 300 K.

Defects in Graphene can range from a myriad of sources, from point defects such as vacancies [28], adsorbed atoms and molecules [29], chemisorbed species [27] and even extended defects [30]. In this aspect of point-wise dislocations and point defects the most likely is the Stone-Wales defect. The Stone-Wales (SW) defect is a well known and common defect in sp^2 carbon-based materials [37], and it consists in a 90 degree rotation of a carbon-carbon bond, this leads to the formation of two heptagons connected with two heptagons. Works dealing with this defect (Ma et al. [39]) suggest that a SW defect could produce a slight out-of-plane deformation, the reason for this is because the full sp^2 hybridized system becomes partially sp^3 hybridized near the defect, this might induce a spin-orbit coupling for the new orbitals hybridization as it has been predicted for the ripples.

Since most of the calculations this work develops are based in defects existing in Graphene, we think that a description of them can give us an idea on their electronic properties and how they could interact with other compounds. This thesis work took four of the most common defects that can take place in monolayer Graphene. A good approach for this is based on DFT calculations, in order to find the relaxed structures and after that find their electronic properties. Nevertheless, we must remember that this defects appearing in Graphene are distributed randomly, so even when DFT can provide us the information for periodic systems and we can take as big the unit cell as we want, the calculation results relies on how we set the parameters involved in the DFT calculation, such as the size of the cell itself, distance between defects, etc.

Although the SW defect is the one with the lowest formation energy, vacancies are not far behind. As its name suggests, this vacancies are just empty sites on the honeycomb lattice. When this happens two scenarios are possible: either the disrupted bonds remain as dangling bonds, or the structure undergoes a bond reconstruction in the vicinity of the vacancy [33].

Here we'll make a simple description of what happens to the electronic structure, instead of using a DFT approach (which will be used later), we just take a simple tight-binding(TB) model in order to explain the existence of the so-called zero mode state. We assume that the only effect of the carbon atom absence is removing the π_z orbital at this lattice point. Taking the general TB with two nearest neighbour hopping

$$H = -t \sum_{<i,j>} c_i^\dagger c_j - t' \sum_{\ll i,j \gg} c_i^\dagger c_j + h.c.. \tag{2.18}$$

When the distribution of vacant sites is different for both sublattices, and if we take the t' hopping as zero, we'll necessary obtain zero energy modes, a result that can be obtained from of linear algebra. If our wave function is written as

$$|\Psi\rangle = (\varphi_A, \varphi_B) \tag{2.19}$$

where the subscripts A and B are denoting a set of amplitudes in each of the N sites for each sub-lattice, the corresponding Schr$\ddot{o}$dinger equation in its matrix block form is the

$$H|\Psi\rangle = E|\Psi\rangle = \begin{pmatrix} \varepsilon_A \mathbb{I}_{N_A} & h_{AB} \\ h_{AB}^\dagger & \varepsilon_B \mathbb{I}_{N_B} \end{pmatrix} \begin{pmatrix} \varphi_A \\ \varphi_B \end{pmatrix} = E \begin{pmatrix} \varphi_A \\ \varphi_B \end{pmatrix}$$

where the identity matrix has the order of the number of sites for each sub-lattice, h_{AB} is a $N_A \times N_B$ matrix. Solving the system we obtain the following set of equations

$$h\varphi_B = (E - \varepsilon_A)\varphi_A \tag{2.21}$$

$$h^\dagger \varphi_A = (E - \varepsilon_B)\varphi_B \tag{2.22}$$

which reduces to

$$h^\dagger h \varphi_B = (E - \varepsilon_A)(E - \varepsilon_B)\varphi_B \tag{2.23}$$

the eigenvalues for H are

$$E = \frac{\varepsilon_A + \varepsilon_B}{2} \pm \sqrt{(\frac{\varepsilon_A - \varepsilon_B}{2}) + \lambda^2} \tag{2.24}$$

the value λ^2 is the positive eigenvalue of the operator $h^\dagger h$. From the solution it is visible the particle-hole symmetry ($t' = 0$). If we take $N_A > N_B$, since the block h_{AB} is a linear application from a vector space having $dim(A) = N_A$, onto a vector space $dim(B) = N_B$,

- $rank(h_{AB}) = rank(h^\dagger_{AB}) = N_B$
- $h_{AB}\varphi_B = 0$ has a solution than can only be the trivial one,
- $h^\dagger_{AB}\varphi_A = 0$ has a non-trivial solution which will be called φ^0_A.

From the linear algebra rank-nullity theorem

$$rank(h^\dagger_{AB}) + nullity(h^\dagger_{AB}) = N_A. \tag{2.25}$$

Hence the null space of $h^\dagger_{AB}$ has dimension $N_A - N_B$, which is the number of non-trivial zero modes.

As Pereira et al. [21] showed in such a procedure, the low energy zero mode has analytical expression,

$$\Psi(x, y) \simeq \frac{e^{i\vec{K}' \cdot \vec{r}}}{x + iy} + \frac{e^{i\vec{K} \cdot \vec{r}}}{x - iy} \tag{2.26}$$

This result shows that the amplitude of this zero energy state decays inversely proportional to the distance $(1/r)$, where the distance is taken from the vacancy

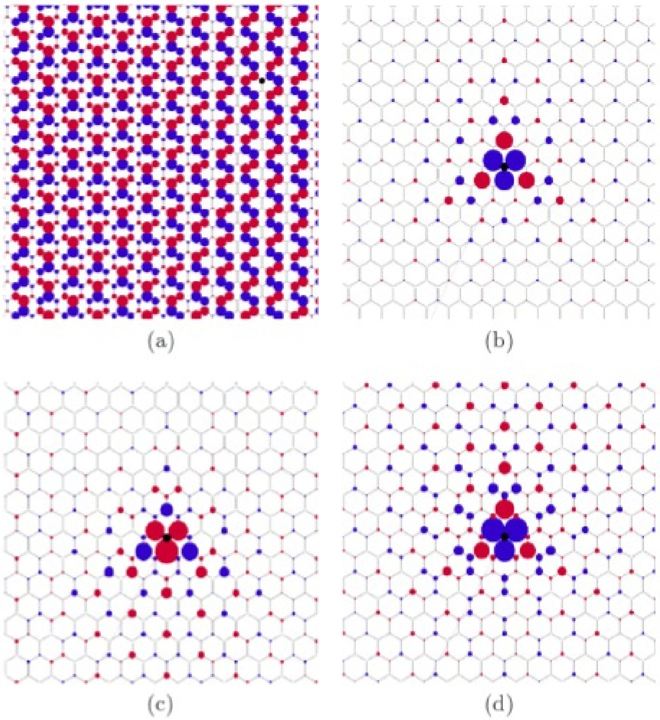
(a) (b) (c) (d)

Figure 2.5: Numerical low energy solutions. (a) shows the pristine Graphene and how the amplitudes are located in each sublattice labeled with red and blue colors. In (b) a vacancy is located at the black dot, the amplitudes decaying as they are far from the vacancy position. (c) and (d) are different plots for different t' values when a second hopping is addressed to the TB model [21].

site. This zero energy mode has a quasi-localized character (although strictly non normalizable) and appears at the Fermi level. If another vacancy is introduced in the same sub-lattice, we already know that another zero mode will appear, however the nature of the two zero modes will depend whether the vacancies are close or distant. For the case in those vacancies are far apart, the hybridization between them should be small on account of the $1/r$ decay, and we can expect two states of the given form above. This simple picture allows for the prediction of localized states when defects are present. In the particular case of simple vacancies this is

true. In the other cases, typically reconstruction of the defects will lead to saturated bonds, which means that defects might be present, but not necessarily.
As mentioned before the other three defects we are going to consider about are the Stone-Wales and the two more probable results after two atoms were taken off,the 2v-585 and 2v-555777 defects, which are divacancies.The presence of the three defects have already been experimentally reported by means of STM experiments [34,35] or TEM images [36].

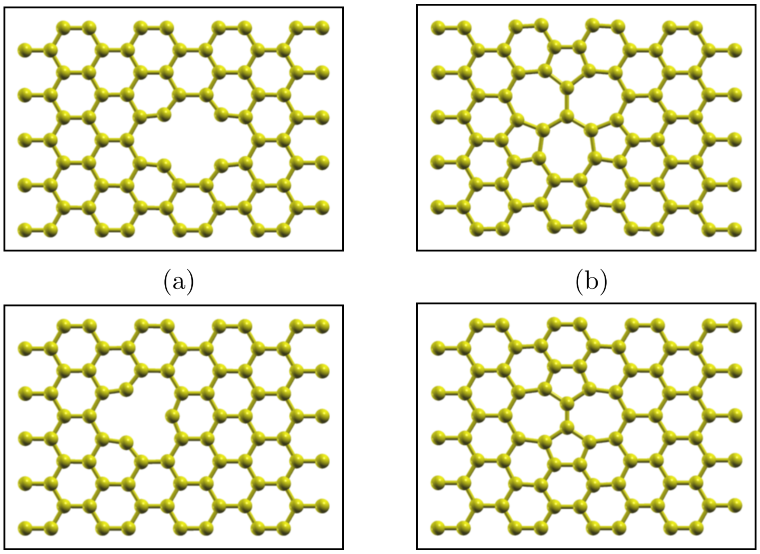
(a) (b)
(c) (d)

Figure 2.6: Top view of the (a) 2v-585, (b) 2v-555777, (c) single vacancy and (d) Stone-Wales defects in graphene.

Vacancies are created in many ways. They can be created by irradiating the graphene sheet with ions such as Ar^+ for instance [32]. These single vacancies can move easy in the graphene plane and are stabilized after they recombine with another one, as a result might create a divacancy. The two kinds of divacancies studied here are the following, a first one which its reconstruction yields the formation of two pentagons and one octagon named here after as 585, while the second one results after reconstruction in three pentagons and three heptagons, thus named

555-777. These defects are shown in Fig. 2.6.

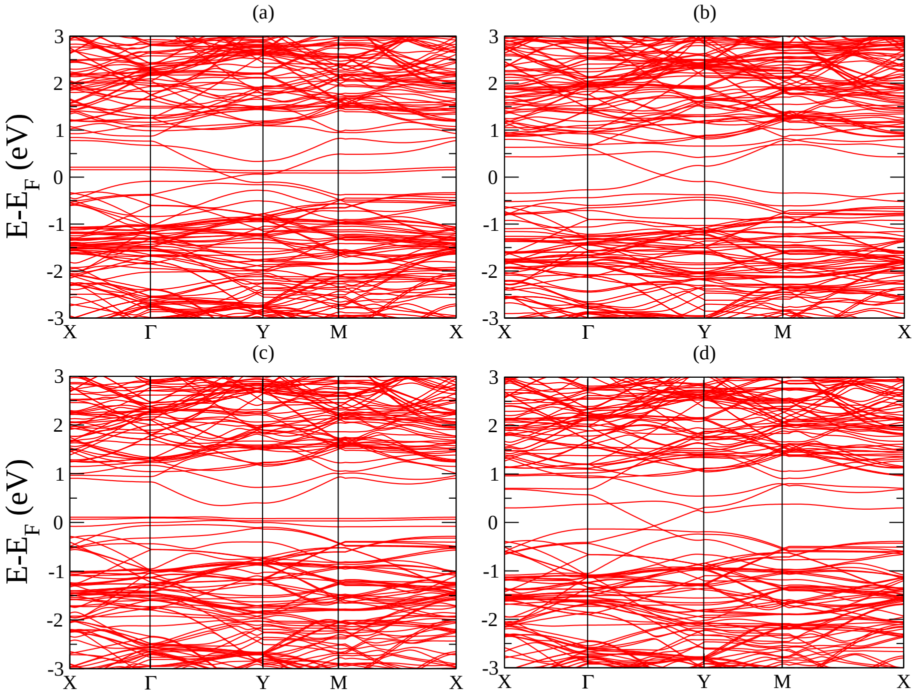

Figure 2.7: Electronic Band structure for (a) 2v-585, (b) 2v-555777, (c) single vacancy and (d) Stone-Wales defects in graphene.

For the sake of comparison between band structures in these four systems, the Fermi energy has been set to the point where in pristine Graphene was the band crossing. For the defect $555-777$, its band structure shows a p-type doping character since the Fermi energy has been shifted below the position of the Dirac point. However the magnitude of the shift is related to the concentration of defects on the structure. For the case of the defect 585, the Dirac point energy is located above the Fermi energy which also implies a p-type character, this does not happen for the Stone-Wales defect which shows the Fermi level at the same energy where the Dirac point is located, this means that this defect has no doping character and it is what happens with the single vacancy as well, where the zero energy mode is shown lying just in between the *pseudo* gap open at the "*Dirac point*" which is located for all the cases in a certain point between the high symmetry points Γ and Y.

Looking for symmetries in this defects, it can be seen that $555 - 777$ defect possesses the same point group symmetry D_{3h} present for the K point in pristine Graphene. Even if very close to the Dirac point energy, the cone is isotropic and for higher energies it has been demonstrated that the so-called trigonal warping appears [34]. This effect is a signature of the symmetry on a single Dirac cone related to the existence of two inequivalent triangular sublattices. The symmetry related to the SW and 555-777 defects is reduced to D_{2h}, since there are only two symmetry axis that can be used for the symmetry operations to be performed, whereas for the case of the single vacancy there is only one symmetry axis.

2.2 Phosphorene

Phosphorus is a pnictogen and then we expect it forms three bonds. This means that it is possible to generate a plane of phosphorus atoms, where every atom has three neighbours and in fact this occurs with the black phosphorus but we can find one structural difference between the black phosphorus and grahite, namely, the layers forming the structure are not perfectly flat, instead, we have a puckered surface due to the sp^3 hybridization. Such a layer is shown inf Fig. 2.8.

Phosphorene is a promising 2D semiconducting material with a direct band gap and high carrier mobility. This material is the monolayer form of black phosphorus, since the bulk is formed by the van der Waals interactions between monolayers, we can obtain the sheet from the exfoliated bulk structure [42]. It has been demonstrated that phosphorene-based transistors posses a larger current on/off ratio compared to graphene-based transistors and higher charge mobility than MoS2-based devices[43]. Furthermore, a tunable gap depending on the number of layers was predicted for this material, which could result in good electronic and/or optoelectronic devices.

Looking to white Phosphorus can give us an idea of the behaviour of the monolayer structure. Due to the electronic configuration of Phosphorus, there are three bonds and a lone pair which results in the sp^3 hybridization of the $3s$ and $3p$ atomic orbitals. Typically, for such a hybridization is found that bonds and lone pairs stemming from an atom form angles of about 109.5°. However because of the molecular structure of P_4, the bonds angles are 60°, showing then the instability of white phosphorus while a strain is applied. Black phosphorus is obtained from the application of high pressures in its white allotrope, where we find a *tripod*-like shape, when three out of six bonds are broken. It's because the increase of the angles the this structure becomes the most stable allotrope of the element. Despite the partial flattening of the four-atom P clusters, they still retain the sp^3 hybridization character of the tetraphosphorus. This explains why when they are linked together, the clusters do

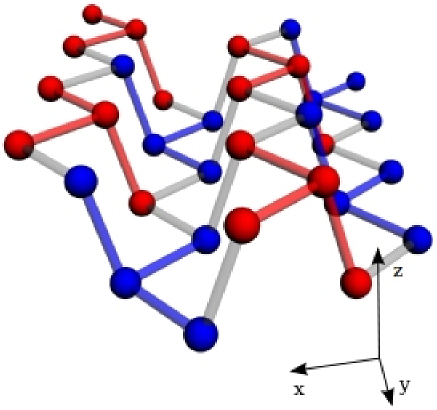

Figure 2.8: Black Phosphorus monolayer lattice, the colors represent two different orientations of the flattered P_4 clusters [44].

not form a flat layer and instead this results in a puckered structure showed in Fig. 2.9.

The illustration shows that the phosphorene monolayer is composed of two different orientations of flattened P_4 structures, denote by two colors. A single buckle is made of alternating P_4 components, and the total lattice is built by replicating that primary structure all along the x direction. In some sense this is similar to the staggered graphene structure, but since it's not a really plane structure, we can relate this difference to the different electronic band structures they show.

Now we can make the difference between the in-plane σ bonds and the out of plane π bonds that exist in graphene. In phosphorene the hybridization results in orbitals that are composed of s and p components. In addition, the puckering breaks the reflection symmetry in z and x directions. This means that while graphene is described by the D_{6h} point group, phosphorene has the C_{2h} symmetry where the principal axis runs along the puckering steps.

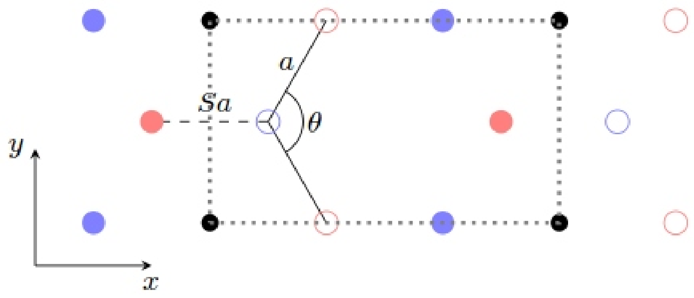

Figure 2.9: Projection of the black Phosphorus lattice onto the $x-y$ plane. Empty circles represent atoms at the bottom, and the filled ones are at the top of the buckled structure [44].

Calculations gave us the band structure of the black phosphorus monolayer showing a semiconductor with a direct band gap around 1.0 eV in the Γ point, which is about 3 times larger than the value found for the bulk counterpart. Experiments and computational methods predict a highly strain dependence on the electronic structure of this material, as also the dependence on the number of layers which are stacked because the the presence of VdW interactions. This featuring lead us to think that we can tune the electronic properties of this system.

On the issue related to the strain dependence, we can show two results exposing this dependence. The first one is a work done by Han Liu, et. al. [42], where besides the discover of the band gap dependence on the number of layers, where E_g scales as the inverse of the number of layers, they showed the sensitive dependence of the gap on in-layer strain along the two different directions, as shown in Fig. 2.11.
We need to point out that in our work we are interested in heterojunctions, which will invariably lead to strain. Thus the horizontal and vertical distances between Phosphorus atoms is modified, probably resulting in a modification of the electronic band structure.

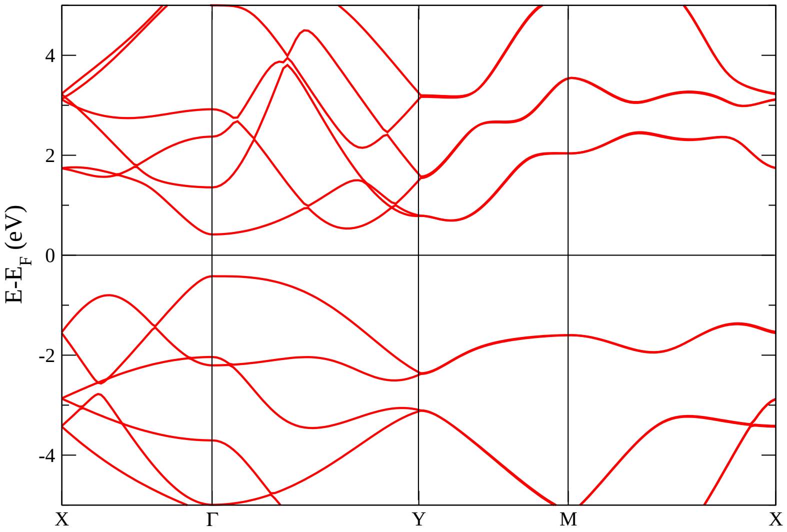

Figure 2.10: Phosphorene electronic band structure.

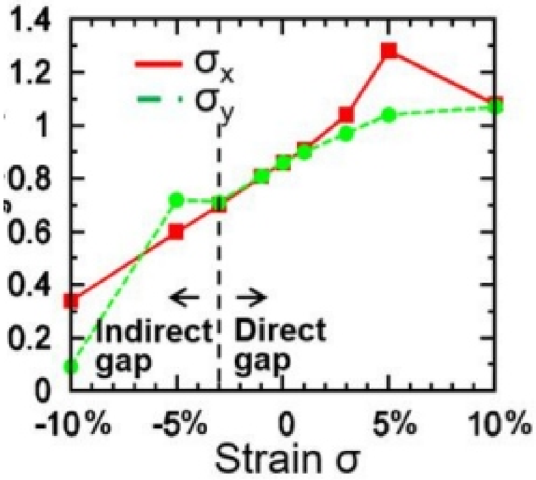

Figure 2.11: Band gap dependence on the two different in-plane strain applied on the layer [41]

A second result obtained by A.S. Rodin et.al [45]., based on a low energy effective Hamiltonian and symmetry arguments, it's shown how an applied strain can modify the electronic band structure, therefore, using *ab initio* calculations they obtained quantitatively the transition between direct and indirect gap, or even between a metallic and a semiconductor behaviour for monolayer phosphorene.

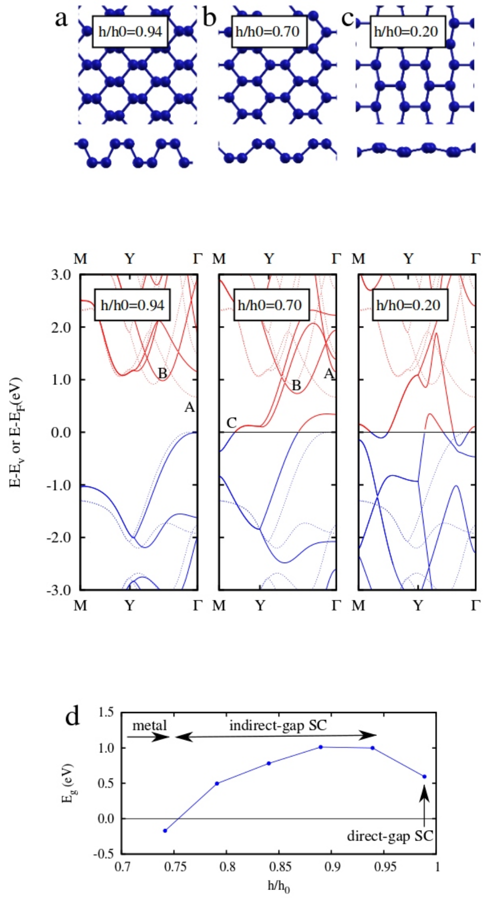

Figure 2.12: Band gap modification as the result of a strain along the z direction, h_0 is the distance between atoms on the upper and lower layers for the relaxed structure, while h is the modification values in order to represent the structure under strain [44].

2.3 Transition Metal Dichalcogenides

As in the phosphorene case, we again have for these materials a difference between the behaviour of the bulk system and its monolayer counterpart. Particularly, here again we have the modulation of the band gap for the bulk which is indirect and turns to a direct band gap for the monolayer system. Monolayer TMDC's have already been implemented in field effect transistors, showing a n-type behaviour in contrast to the phosphorene p-type behaviour [45,46].
Like in graphene case, in transition metal dichalcogenide we also have the honeycomb lattice structure, with three atoms instead. The transition metal dichalgonides are another class of layered materials, which has received considerable attention as it can be exfoliated down to its monolayer form. The unit cell is formed with the chemical composition MX_2 where $M = Mo$ or W and $X = S, Se$ and Te. One position is occupied by one metal atom which is located in the middle plane, whereas the other two atoms belong to different planes as the Fig. 2.13 shows. Works related to the electron-phonon coupling showed that single layers of TMDC's MoS_2, MoSe_2, WS_2 and WSe_2 are dynamically stable [55].

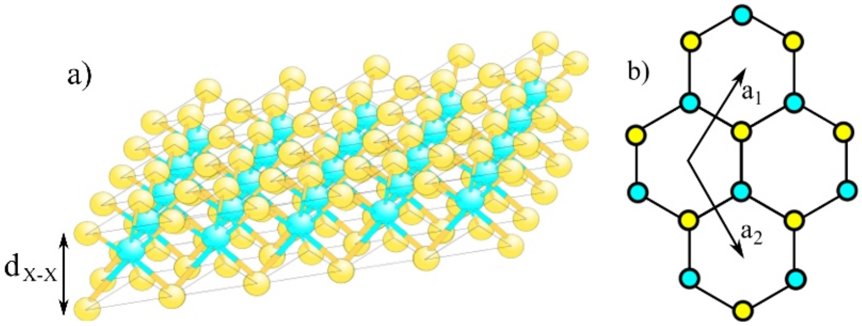

Figure 2.13: Monolayer structure of a TMDC. (a) side and (b) top views. The vectors with lattice parameter $|\vec{a}_1| = |\vec{a}_2| = a_0$ and the d_{X-X} distance between X's atoms are also shown.

Another difference here is related to the gap in the electronic band structure. Since the inversion symmetry is broken, due to the different species located in the unit cell, it produces a gap where in the graphene's case we'd have a Dirac Cone. However the properties present in graphene, as *chirality* and the helicity, also find their place in these systems, because different from the massless Dirac equation in graphene, we have a massive Dirac equation instead [47]. The previous property besides the existence of a large SOC, produces nice features for these $2D$ systems, some of which we will address in what follows.

In order to understand the electronic properties of TMDC's, we use results from DFT together with a perturbative $k \cdot p$ approximation, which takes into account low energy effective models to reproduce certain characteristics of the band structure using some fits obtained from previous *ab initio* calculations. We can use some Group theory techniques to find transition rules, and reduced the effort for the calculation of the Hamiltonian Matrix elements. Here we'll not explain the whole treatment, we'll give the main results instead, and because the theory is a local approach, we can learn more about the band dispersion near the high symmetry points.

The direct band gap is located at the K and K' points in the Brillouin zone as Fig. 2.14 shows, we can see that due the lack of inversion symmetry (different from Graphene), all bands are split by the intrinsic SOC except at the time-reversal points M and Γ [54]. The spin-splitting values for both bands are denoted by $2\Delta_{vb}$ and $2\Delta_{cb}$ for valence and conduction band respectively. It's important to mention the existence of another six points in the whole Brillouin zone, which exhibit minimum values for the conduction band and also a large spin-splitting, these six point are located between the Γ and $K(K')$ points, and are related, for example, to transport or relaxation processes in certain compounds.
Several works have found that different atomic orbital composition can explain easily the difference in the spin-splitting magnitude of the CB and VB at the K point [58]. The orbital composition in the electronic band structure is shown in Fig. 2.15. The plot shows that for the d orbitals from the metal atom and the p orbitals from the chalcogen. Looking at this projected orbitals onto the band structure, we find that in general more than one type of atomic orbital changes throughout the Brillouin

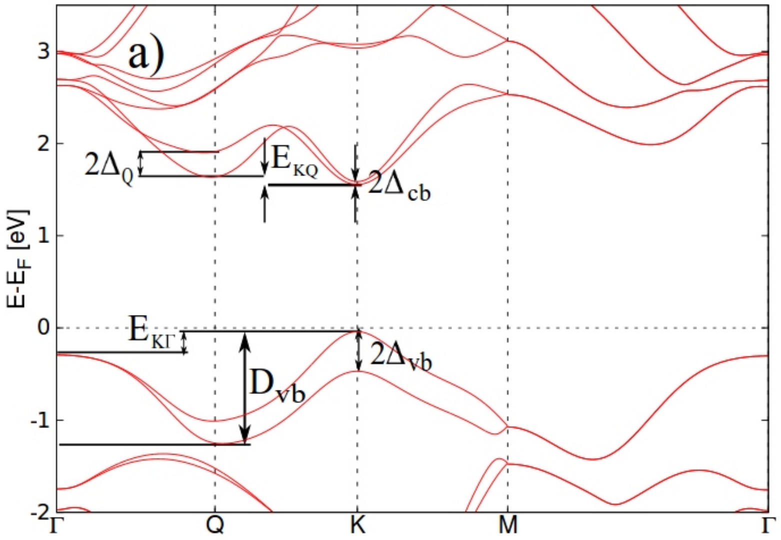

Figure 2.14: MoS_2 band structure with SOC. Δ_x is the Split size at point x, E_{ab} is the energy difference at a and b points, and D_{vb} is the difference between the top and bottom in the highest valence band [54].

zone. Therefore, a tight-binding treatment is more complicated than in Graphene's case.

In this part we make a description of the K and K' points in the band structure, which resembles to the low energy linear dispersion in graphene, and for that reason they has attracted the most attention both experimentally and theoretically. This is related to the exciting optical properties of these materials at direct band gap [52], moreover, the effect of SOC is strong at this point in the Brillouin Zone, leading to spin-split and spin polarized bands. These two points are connected by time reversal, then the polarization of the bands has to be opposite at both K and K', i.e., the spin and the valley degrees of freedom are coupled, this gives rise to a new effect, the so-called $Valley\ Hall\ Effect$ [57].

The results from DFT calculations have shown a difference in the split conduction band by the SOC inclusion in MoX_2 and WX_2 materials [54], this is important in the

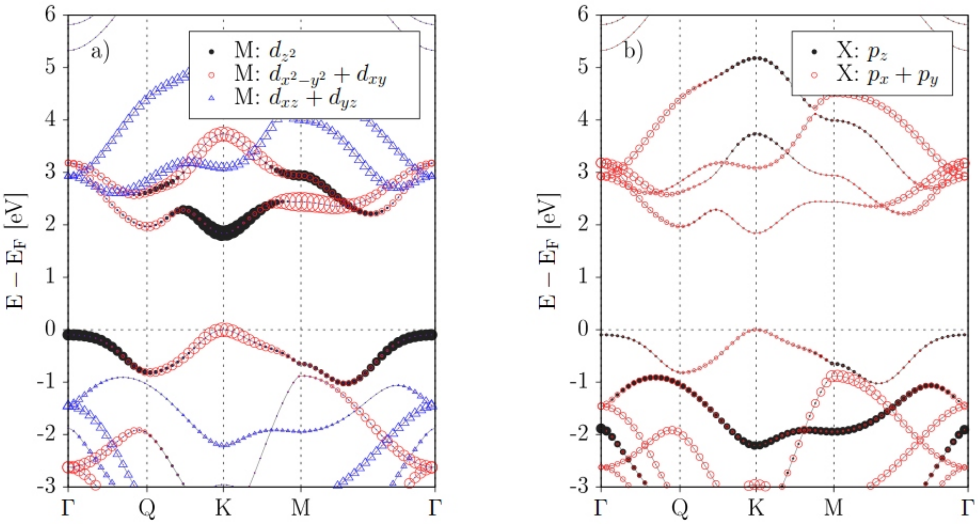

Figure 2.15: Orbital projection for M (a) and X (b) chemical species [54].

interpretation of experiments where properties of A and B excitons are compared. Experimental results in the energy difference between A and B excitons give an explanation for the spin-splitting of the VB too [49]. From the Band structure we can see that the SOC in CB at this point is a more subtle effect that in the VB, this can be explained using the $k \cdot p$ approach, if we take just the d_{z^2} as the only contribution, by symmetry arguments, the SOC effect vanishes. However, DFT calculations show a finite splitting in CB, this means that we have to introduce other orbitals contributions at this point.On the other hand, we can see that for MoX_2 systems(except for $MoTe_2$) the band with the lighter effective mass is lower in energy, leading to band crossing of the two split-bands in near the $K(K')$ point, whereas for WX_2 the lighter spin-split band is higher in energy and then we don't have band crossing.

The energy dispersion at the K point can be approximated as [48]

$$E_K(\vec{q}) = \frac{\hbar^2 q^2}{2m_{eff}} + C_{3w}|q|^3 cos(3\varphi_q), \tag{2.27}$$

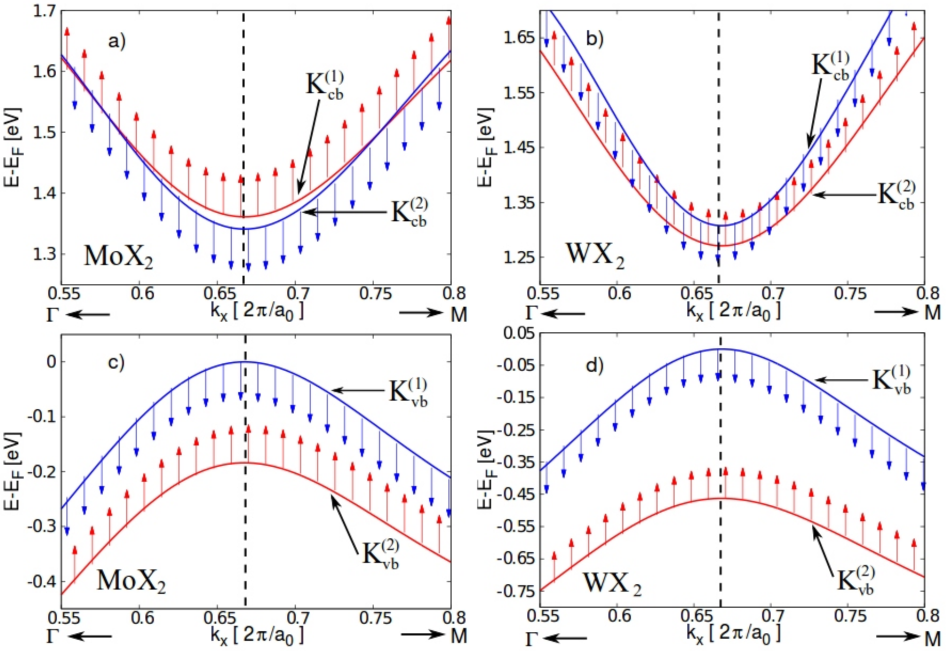

Figure 2.16: Spin-splitting in bands caused by the Spin-Orbit Coupling. (a) and (c) show the band splitting (for conduction and valence bands respectively) at the K point for MoX$_2$ type materials, (b) and (d) show the band splitting equally for the WX$_2$ type materials [54].

Where the wavevector $\vec{q} = (q_x, q_y)$ is measured taking the K point as the origin, $\varphi_q = arctan(q_y/q_x)$, m_{eff} is the effective mass for the given band, and C_{3w} is a parameter describing the TW. This expression was obtained taking a multi-band $k \cdot p$ approach, using second order approximation, since at first order we just obtain a quadratic dispersion. This resembles in a way to the expression of the energy around K for Graphene, where the TW is present too [1].

Now we introduce the low energy $k \cdot p$ Hamiltonian which explains the coupled dynamics between valence and conduction bands, where the approximation can be as accurate as more bands we take into the calculation. For this case to be accurate, the calculation requires a model involving seven bands [54]. From a procedure called *Lowdin* partitioning [83], using perturbation theory we expand up to third order, where terms as the Trigonal Warping appear as we can see in Eq. 2.27. We use a spinful basis $\{|\Psi^{vb}\rangle, |\Psi^{cv}\rangle\}$, where $|\Psi\rangle$ are the spinless Bloch functions for both valence and conduction bands, and s is related to the spin space $s = (\uparrow, \downarrow)$, The Hamiltonian obtained has the following form

$$H_{eff}^{\tau,s} = H_0 + H_{k\cdot p}^{\tau,s} + H_{SO}^{\tau,s}, \tag{2.28}$$

where the first term H_0 is the kinetic term, τ and s are the index referring to valley and spin spaces, $H_{SO}^{\tau,s}$ is the Spin-Orbit Coupling Hamiltonian which is proportional to the σ_z matrices and does not depend on the wavevector $\vec{q}$, written as

$$H_{SO}^{\tau,s} = \begin{pmatrix} \tau\Delta_{vb}s_z & 0 \\ 0 & \tau\Delta_{cv}s_z \end{pmatrix}, \tag{2.29}$$

the values that s_z and τ indexes can take are ± 1 and they are the eigenvalues of the the valley and spin operators ± 1. Finally the last contribution is the $k \cdot p$ Hamiltonian which again is made of the following parts,

$$H_{k\cdot p}^{\tau,s} = H_D^{\tau,s} + H_{as}^{\tau,s} + H_{3w}^{\tau,s} + H_{cub}^{\tau,s}, \tag{2.30}$$

In this case,

$$H_D^{\tau,s} = \begin{pmatrix} \varepsilon_{vb} & \tau \cdot \gamma_{\tau,s} q_-^{\tau} \\ \tau \cdot \gamma_{\tau,s}^{*} q_+^{\tau} & \varepsilon_{cv} \end{pmatrix}, \tag{2.31}$$

it basically describes the massive Dirac Hamiltonian, taking $q_\pm$ defined as $q_\pm = q_x \pm i\tau q_y$,$\varepsilon_{vb,cb}$ are the band edges energies and γ is one of the material constants we use as a fitting parameter, note that this parameter depends on both two degrees of freedom (valley and spin). The Asymmetric part is written as

$$H_{as}^{\tau,s} = \begin{pmatrix} \alpha_{\tau,s}q^2 & 0 \\ 0 & \beta_{\tau,s}q^2 \end{pmatrix} \tag{2.32}$$

here again α and β are material parameters depending on τ and s, this part of the Hamiltonian breaks the electron-hole symmetry, result which is in agreement with recent experimental data on observation of photoluminescence peak splitting in magnetic fields [53].
The latter terms are the sum of a cubic term in $\vec{q}$, a required contribution in order to obtain a better fit for a broader region around the K point and claims the fact we have non-parabolicity in the bands. The last one carries the trigonal warping for the bands, these two contributions are the following

$$H_{3w}^{\tau,s} + H_{cub}^{\tau,s} = \begin{pmatrix} 0 & \kappa_{\tau,s}(q_+^\tau)^2 \\ \kappa_{\tau,s}^*(q_-^\tau)^2 & 0 \end{pmatrix}$$

$$-\tau\frac{\omega_s}{2}|q|^3 cos(3\varphi_q)\begin{pmatrix} 1 & 0 \\ 0 & 1 \end{pmatrix} \qquad (2.33)$$

Where κ and ω are material constants, φ_q is the angular variable in reciprocal space.

The Hamiltonian written above, describes the bands and their features, since it includes cubic terms in q and also material parameters. This construction will help us to obtain the new material parameters for the bilayer made from $\mathrm{MoTe_2}$ and Graphene, this is shown in the Results.

In contrast we have from a tight binding approach the following Hamiltonian [48]

$$H_D = \gamma(\tau q_x\sigma_x + q_y\sigma_y) + \frac{E_{bg}}{2}\sigma_z + \Delta_{vb}\tau s_z\frac{\sigma_z - 1}{2}. \qquad (2.34)$$

Where the band gap term(E_{bg}) appears and is proportional to the sub-lattice index σ_z, the indices τ and s_z are the Pauli matrices related to the valley and spin degrees of freedom respectively, γ is the hopping term and Δ_{vb} is the splitting value for the Valence band. This Hamiltonian can explain the large splitting of the valence band and also predicts the valley-dependent optical selection rules which are related to the Valley Hall Effect [57], however it fails when we try to compare with some DFT results, which are the spin splitting in conduction band, the electron-hole asymmetry and trigonal warping.

2.4 Heterostructure Systems

With the acquired knowledge of the three materials presented above, the idea of what would happen if we put together sheets coming from each of them arises naturally. Graphene by itself, being the first 2 dimensional material realized in the last decade, is a common topic in condensed matter physics and also the one who has the more proposals to become a central ingredient in the next generation technologies. Furthermore, every 2 dimensional material that came after Graphene, is always related to the former in such a way that properties coming from the mixture of them, graphene plus other 2d material, enhances Graphene's traits. This is one of the main reasons for the study of Heterostructure systems, where they are stacked together in order to bring new characteristic from them. Before we start the study of such a system, we first need to know what are the main characteristics of the building blocks in this Heterostructure, Fig. 2.17 shows a table carrying some information related to this.

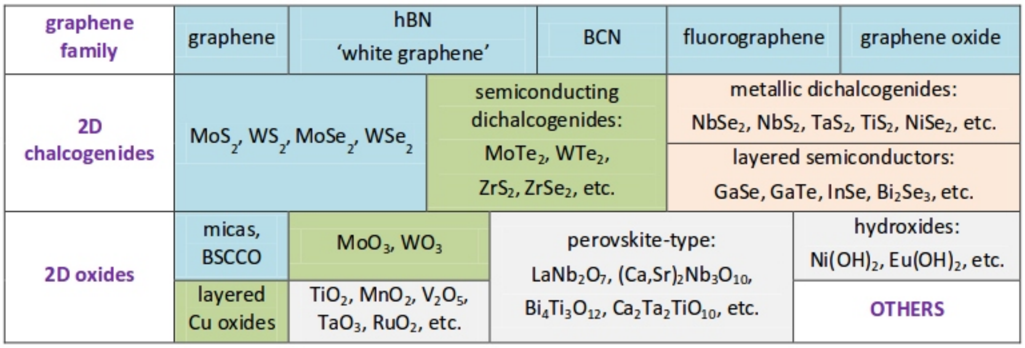

graphene family	graphene	hBN 'white graphene'	BCN	fluorographene	graphene oxide
2D chalcogenides	MoS_2, WS_2, $MoSe_2$, WSe_2	semiconducting dichalcogenides: $MoTe_2$, WTe_2, ZrS_2, $ZrSe_2$, etc.		metallic dichalcogenides: $NbSe_2$, NbS_2, TaS_2, TiS_2, $NiSe_2$, etc. layered semiconductors: GaSe, GaTe, InSe, Bi_2Se_3, etc.	
2D oxides	micas, BSCCO layered Cu oxides	MoO_3, WO_3 TiO_2, MnO_2, V_2O_5, TaO_3, RuO_2, etc.	perovskite-type: $LaNb_2O_7$, $(Ca,Sr)_2Nb_3O_{10}$, $Bi_4Ti_3O_{12}$, $Ca_2Ta_2TiO_{10}$, etc.	hydroxides: $Ni(OH)_2$, $Eu(OH)_2$, etc. **OTHERS**	

Figure 2.17: Current 2D library, table shows in the blue cells the monolayers proven to be stable under ambient conditions(room T in air); in green are the probably stable in air; pink is for the unstable in air but maybe stable in inert atmosphere. Grey cells indicate 3D compounds which have been successfully exfoliated down to monolayers. For others we have many other 2D crystals including borides, carbides, nitrides, etc. have been or can be isolated [13].

There are currently several works dealing with this topic, the most are related to bilayers where one of the sheets is Graphene and the other one can be a Transition Metal Dichalcogenide monolayer or Phosphorene as we took as the systems to work with. Padilha et. al. [60], took a bilayer made of Phosphorene and Graphene stacked by VdW forces where they try to tune the position of the Phosphorene Band Gap with the Graphene Fermi energy fixed, this brings the possibility to manipulate the height of the Schottky barrier and dope the Phosphorene, this enhances the chances to the development of new electronic devices based on this one-atom-thick materials.

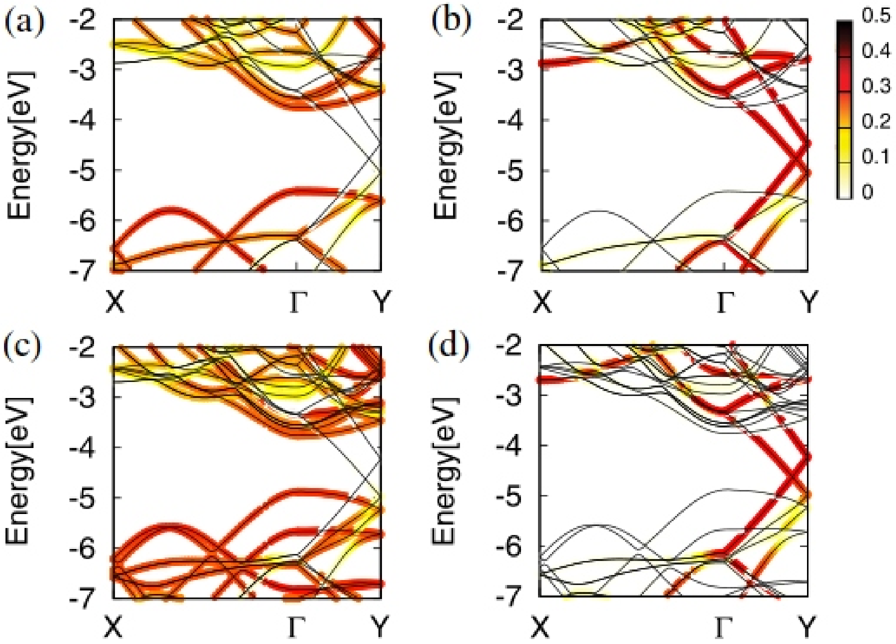

Figure 2.18: Band structure for bilayer Phosphorene/Graphene. (a) and (b) show the Phosphorene and Graphene projections onto the electronic band structure respectively, for the bilayer case. (c) and (d) shows the same projection but in this case the system is formed by a Phosphorene bilayer with a simple Graphene layer [60].

The Fig. 2.18 above shows the Band structure of single-layer phosphorene on top of graphene projected at the (a) phosphorene layer and (b) graphene layer. Band structure of bilayer phosphorene on top of graphene projected at the (c) bilayer phosphorene and (d) graphene layer. The scale besides indicates the magnitude of the projection.

Other works related with the same subject deal with the stability of Phosphorene instead, where it's been found that materials like Borono Nitride (BN) and Graphene can cover and protect the chemical- and environment-sensitive of Phosphorene, without compromising properties as the direct band gap and linear dichroism [50]. In addition, a large redistribution of electronic potential across the interface is observed, which may significantly re-normalize the carrier dynamics and affect the excitonic behaviour of phosphorene. Works like this one were developed e.g by Yongqing Cai et. al. [61] where the Local DOS they obtained is shown in Fig. 2.19.

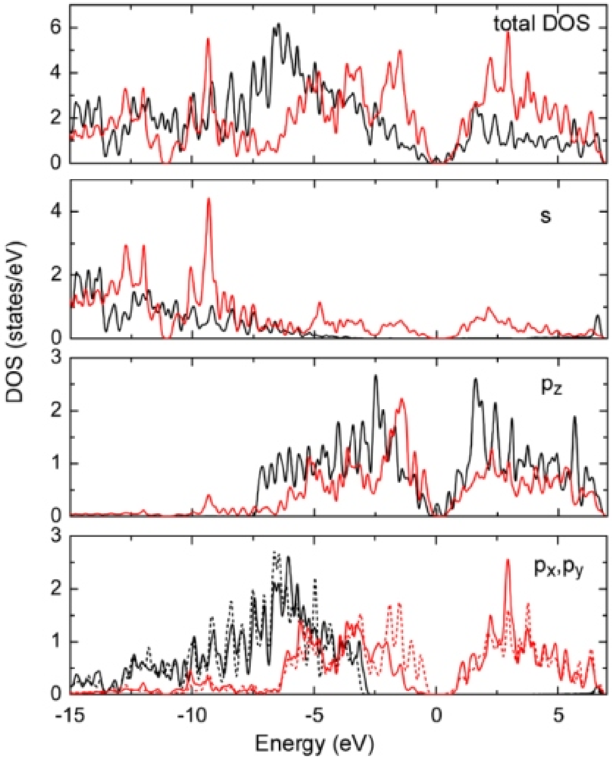

Figure 2.19: LDOS for Phosphorene/Graphene bilayer [61].

For the LDOS shown we have the electronic states from phosphorene and graphene plotted in red and black respectively. In the bottom panel, the p_x and p_y states are represented by the solid and dashed lines respectively.

On the other hand, hybrids of graphene and TMDC have the potential to increase the performance of graphene in the field of spintronics [51], there are several advantages of such hybrids over pristine graphene, for instance, Dirac electrons in Graphene exhibit a sort of proximity spin-orbit coupling, without compromising the semimetallic character of the Heterostructure [52]. A second property of these heterostructure is that, as in Graphene/Phosphorene bilayer, the Fermi level can be tuned by a transverse electric field to cross the TMDC conduction band, creating a system of coupled massive and massless electron gas [62]. Taking into account these features and the previous relation between valley and spin degrees of freedom in TMDC, there is a chance to use these such a heterostructure as a platform for opto-spintronics.
The Fig. 2.20 shows the electronic and spin properties of graphene on MoS_2. The work developed by Gmitra et al. [63], shows that there are two important effects, the first one is the an orbital band gap opens, due the breaking of the graphene pseudospin symmetry, it's like saying that in average atoms in different A and B sublattices see a different environment coming from the MoS_2 layer. The orbital gap opened is there even in the absence of SOC, meaning that it arises from the staggered potential induced by the pseudospin symmetry breaking.

The second consequence is related to the combined effects of SOC and the broken space inversion symmetry, which lifts the spin degeneracy of the Dirac valence and conduction bands, and now there are four distinct bands. The magnitude of the splitting obtained is larger than the value of the SO splitting for pristine Graphene. The spin texture plotted in Fig. 2.20, shows that at K the spins are pointing out of the graphene plane, alternating up and down. Increasing the momentum away from K, the spins acquire a winding in-plane component, either clockwise or counterclockwise, suggestive of the strong Rashba effect because interaction between layers.

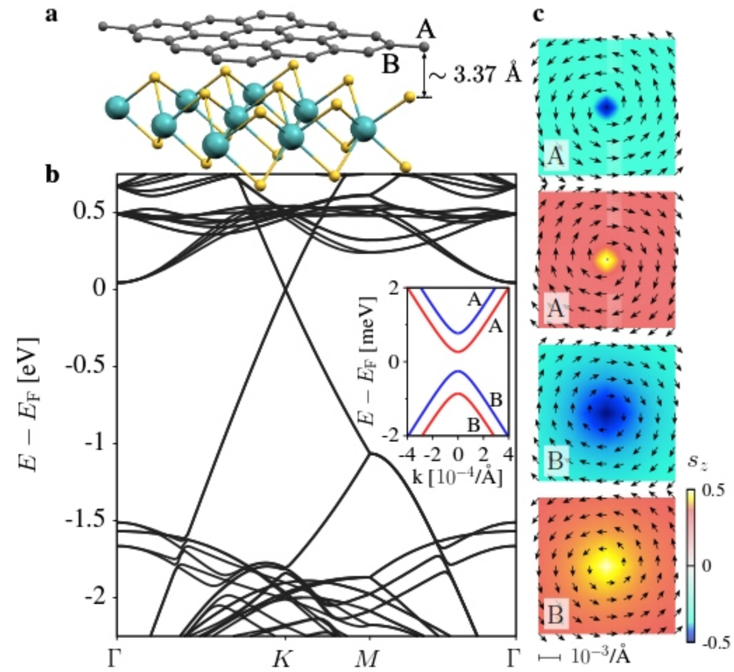

Figure 2.20: MoS_2 on graphene, the supercell is shown in (a), the band structure along the high symmetry points, where also there is a zoom of the low energy bands at the Fermi level around the Dirac point in (b), bands with positive (negative) z component of the spin is shown in red(blue), the letters A and B are related to the sublattice character. In (c) the spin textures are shown for the four bands in the zoomed picture [63].

The opposite happens for the K' point, where the spins are reversed.

2.5 Spin-Orbit Coupling

One of the goals this thesis work intends to cover is the inclusion of the Spin-Orbit Coupling (SOC) effect on the electronic properties of the 2D materials which were exposed before. For this, we give a brief description of what is the SOC and how it can be introduced in the treatment of the electronic properties in solids.

The Spin-orbit coupling (SOC) is the result of the interplay between the orbital momentum and the spin degree of freedom, namely, is a process in which an electron changes simultaneously its spin and angular momentum. This effect can be observed when the electron relativistic motion has taken into account, and can be derived from the Dirac equation. The strength of the SOC is related to the atomic number of the atoms which are involved, then it is large for heavy fermions where the average velocity of the electrons is higher. Due to the Pauli principle, two electrons can have the same energy as long as they have different spin numbers. However, one of the main effects produced by the Spin orbit interaction is a lift in the degeneracy of the electronic energy levels.

The relativistic correction given by the Dirac equation leads to an expression for the SOC as

$$\frac{-\varepsilon\hbar}{4m^2c^2}\vec{\sigma}\cdot(\vec{E}\times\vec{p}) = \varepsilon\ 2m^2c^2\vec{s}\cdot(-\frac{1}{\varepsilon}\frac{\vec{r}}{r}\frac{dV}{dr}\times\vec{p}) = \frac{1}{2m^2c^2r}\frac{dV}{dr}(\vec{s}\cdot\vec{l}), \qquad (2.35)$$

where $\vec{s} = \frac{\hbar}{2}\vec{\sigma}$ represents the spin and $\vec{l}$ the angular momentum. The case of main importance for us is related to the effect SOC can bring for periodic systems as the system we are working with. In a free system, SOC will separate the energy levels with the same orbital wave function but opposite spins. However, in systems with crystal symmetries, as is the case for solids, we might treat the problem carefully.

Time reversal preserves the Kramer's degeneracy [82], a topic which is explained in

Appendix B. This theorem states that a wave function $\psi(r, s)$ only differs from its complex conjugate $\psi^*(r, s)$ by reversal the wave vector (opposite) and the spin. In other words, if we are working in reciprocal space, we'll have

$$E(k, \uparrow) = E(-k, \downarrow). \tag{2.36}$$

As we have mentioned, if our system is periodic, another symmetry is present, namely, spatial inversion symmetry. As a result of this symmetry we have that the lattice does not change under the operation

$$\vec{r} \quad \rightarrow \quad -\vec{r} \tag{2.37}$$

From this, the relation between the energy bands must satisfy

$$E(k, \uparrow) = E(-k, \uparrow). \tag{2.38}$$

The relations (2.36) and (2.38) together lead to the following relation

$$E(k, \uparrow) = E(k, \downarrow). \tag{2.39}$$

This means that even when the SOC is present, for systems having inversion symmetry, the bands will remain degenerate. From this argument, the bands in graphene, besides the fact that SOC has negligible effects for light systems, are degenerate at the K point, while this does not happen for the case of Transition Metal Dichalcogenides. Situations like these are present in our systems as we will see in the results.

Chapter 3

Methodology

Our main aim in this dissertation is to describe the electronic properties of different two dimensional materials. Thus our system consists of a set of nuclei and electrons interacting with each other due to the electrostatic Coulomb repulsion. Since we have a quantum mechanical system, there is a Schrödinger equation describing the system, i.e. the time independent equation to be solved is written as

$$\hat{H}\Psi_n(\vec{R},\vec{r}) = \epsilon_n \Psi_n(\vec{R},\vec{r}) \tag{3.1}$$

Where $\vec{R} = \{\vec{X}_1, \vec{X}_2, ..., \vec{X}_N\}$ is denoting the nuclei coordinates and $\vec{r} = \{\vec{x}_1, \vec{x}_2, ..., \vec{x}_n\}$ the electronic coordinates, meaning that our wave function in principle depends on the nuclei and electronic coordinates. The n index denotes the energy levels of our system, and because we are working with a considerable amount of particles, we'll call this levels as bands.

The Hamiltonian for this problem can be decomposed in the following parts, taking into account kinetic contributions and electronic interactions:

$$\hat{H} = \hat{T}_N + \hat{T}_e + \hat{V}_{Ne} + \hat{V}_e + \hat{V}_N \tag{3.2}$$

where $\hat{T}_N$ and $\hat{T}_e$ correspond to the kinetic energy of the nuclei and electrons respectively. $\hat{V}_{Ne}$ represents the Coulomb interaction between nuclei and electrons, $\hat{V}_e$ is due the Coulomb interaction between the electrons themselves and $\hat{V}_N$ represents the interaction between nuclei. Written in a more explicit fashion, this looks like

$$\hat{H} = -\sum_i^N \frac{\hbar^2}{2m_i}\nabla^2_{\vec{R}_i} - \sum_i^n \frac{\hbar^2}{2m_e}\nabla^2_{\vec{r}_i} - e^2\sum_i^n\sum_j^N \frac{Z_{\vec{R}}}{|\vec{r}_i - \vec{R}_j|} \tag{3.3}$$

$$+\frac{e^2}{2}\sum_i\sum_{j\neq i}\frac{1}{|\vec{r}_i - \vec{r}_j|} + \frac{e^2}{2}\sum_{\vec{R}_i}\sum_{\vec{R}_{j\neq i}}\frac{Z_iZ_j}{|\vec{R}_i - \vec{R}_j|}$$

The $Z's$ and m_N are the charges and masses of the nuclei respectively.
The Coulomb interaction between different particles (electron and nuclei) doesn't let us write the total wave function as a product of electron and nucleus wave functions. This brings to the first problem when we have to find the energy eigenvalues ϵ_n, this means that we need to use some approximation in order to solve the problem.

3.1 Born-Oppenheimer Approximation

One way to tackle the problem posed above is the so called Born-Oppenheimer approximation [64]. This approximation tell us that due to the significantly different masses characterizing electrons and nuclei (and subsequently the velocities), we can solve the problem using two separate time scales. Thus, we can assume the nuclei as fixed and the electrons moving around them in such a way that we can neglect the kinetic contribution of the nuclei. The total Hamiltonian can then be seen as a set of interacting electrons with a background potential, just like in the Jellium model [65], due to the nuclei.
The original proposal in this approximation made by Born and Oppenheimer [64] was to include the nuclei movement using a new set of nuclei variables $\vec{R} = \vec{R}_0 + \vec{u}$, where $\vec{u}$ represents a dislocation around the nucleus equilibrium position. With this, they found the system Hamiltonian as an expansion in terms of $k = (m_e/M_N)^{1/4}$ [79]. Keeping terms from fourth order and higher, they showed that there is no mixing between different electronic states and it was mediated by the interaction with

the nuclei. Then, under appropriate conditions, there are no transitions between stationary electronic states. The picture one has now, is that of electrons adjusting their wave function before the nuclei move to another configuration (and changing their wave function). From this argument, a given set of nuclear positions we write the total wave function as

$$\Psi(\vec{R},\vec{r}) = \sum_m \Phi_m(\vec{R})\psi_m(\vec{R},\vec{r}) \tag{3.4}$$

where the index m refers to a particular configuration of the nuclei which is described by the nuclear wave function Φ.
The Hamiltonian describing the electron dynamics is

$$\hat{H}_e = \hat{T}_e + \hat{V}_{Ne} + \hat{V}_e, \tag{3.5}$$

and satisfies the following eigenvalue problem:

$$\hat{H}_e\psi_n(\vec{R},\vec{r}) = E_n\psi_n(\vec{R},\vec{r}). \tag{3.6}$$

If we include the total wave function (written in eq. 3.4) in the initial Schr$\ddot{o}$dinger equation (3.3) and multiply by the electronic wave function from the left $\langle\psi_m|$, we have

$$\begin{aligned}[i\hbar\frac{\partial}{\partial t} + \sum_{\vec{R}} \frac{\hbar}{2m_N}\nabla^2_{\vec{R}} - V_N - E_n(\vec{R})]\Phi_n(\vec{R},t) = -\sum_{\vec{r}}\sum_{\vec{R}} \frac{\hbar^2}{2m_N}\left\langle\psi_n|\nabla^2_{\vec{R}}|\psi_m\right\rangle \Phi_m(\vec{R},t) \\ -2\sum_{\vec{r}}\sum_{\vec{R}} \frac{\hbar^2}{2m_N}\nabla_{\vec{R}}\Phi_m(\vec{R},t)\left\langle\psi_n|\nabla_{\vec{R}}|\psi_m\right\rangle. \end{aligned} \tag{3.7}$$

From the previous equation we see that there are off diagonals terms. The adiabatic approximation [79] dictates that we can neglect this contributions and find no mixing in the stationary electronic eigenstates, so the total wave function turns out to be:

$$\Psi(\vec{R},\vec{r}) = \Phi_m(\vec{R})\psi_m(\vec{R},\vec{r}), \tag{3.8}$$

This means that we can find independently the electronic and nuclear spectrum. The electronic Hamiltonian will be explained in the next section, since is the main part of this thesis, but let us explain a little bit more about the nuclear part. The previous procedure gives also a part for the nuclear wave function:

$$i\hbar\frac{\partial\Phi(\vec{R},t)}{\partial t} = (-\sum_{\vec{R}}\nabla^2_{\vec{R}} + E_m(\vec{R}) + \sum_{\vec{R}}\langle\Phi_m|\nabla^2_{\vec{R}}|\Phi_m\rangle)\Phi_n(\vec{R},t). \tag{3.9}$$

This equation shows that the nuclear energy has taken into account the total electronic energy too and if we take off the electronic dependence on the nuclear motion, we make the diagonal term vanishes ($\langle\Phi|\nabla^2|\Phi\rangle$). The reason for the previous step is because it has been already found that this term gives negligible corrections since it depends on the electron mass [66]. When such a term is neglected we refer this approximation as the *Born-Oppenheimer* approximation [79], and when the term is included, the approximation is called *adiabatic*.

Even when the problem seems to be simplified, there are still difficulties in its resolution. We are still left with the problem of solving Eq. 3.6 for all electronic degrees of freedom. In order to deal with this problem we'll use a well known approach to find the solution, namely Density Functional Theory (DFT). It has proved to be a great tool when we need to describe the electronic properties and ground states for crystalline solids and complex systems as molecules.

3.2 Density Functional Theory

As we have mentioned before, there is a way to solve the electronic many body system Hamiltonian. The first attempt was a proposal made by Thomas [67] and Fermi [68], when they tried to use the total charge density as a variable in order to find the atomic energy spectrum. Hohenberg and Kohn (HK) [71] showed that the many body wave function is related to the calculation of the equilibrium charge density $\rho(\vec{r})$ [69]. The definition for the charge density is the following

$$\rho^{\sigma_1}(\vec{r_1}) = N\int|\Psi^e(\vec{r_i})|^2 d\sigma_2 d\sigma_3 ... d\sigma_N d\vec{r_2} d\vec{r_3} ... d\vec{r_N} \tag{3.10}$$

$$\rho(\vec{r}) = \int \rho^{\sigma}(\vec{r})d\sigma = \rho^{\uparrow}(\vec{r}) + \rho^{\downarrow}(\vec{r}) \tag{3.11}$$

where the σ letter is denoting the spin degree of freedom, and Ψ^e is the normalized total electronic wave function.

$$\int \rho^{\sigma}(\vec{r})d\sigma d\vec{r} = N \tag{3.12}$$

This fundamentally new approach is based on two theorems which guarantee the validity of this methodology. In what follows there is a brief description of these theorems.

3.2.1 1st Theorem

"The external potential is determined ,up to a constant, by the electronic charge density $\rho(\vec{r})$ for any interacting system embedded in an external potential $v(\vec{r})$, ".

To prove this we can think that there exist two potentials $V^1_{ext}(\vec{r})$ and $V^2_{ext}(\vec{r})$ which differ by more than a constant and also give rise to the same ground state density, $\rho(\vec{r})$. Both potentials belong to distinct Hamiltonians, e.g. $\hat{H}^i_{ext}(\vec{r})$ with $i = 1, 2$, which give rise to distinct wave functions $\Psi^i_{ext}(\vec{r})$. Variational principle ensures that there is no wave function that can give an energy which is less than the energy of $\Psi^1_{ext}(\vec{r})$ for $\hat{H}^1_{ext}(\vec{r})$,

$$E^1 = \langle\Psi^1|\,\hat{H}^1\,|\Psi^1\rangle < \langle\Psi^2|\,\hat{H}^1\,|\Psi^2\rangle \tag{3.13}$$

If we assume that there is not degeneracy in the ground state, then this inequality strictly holds. Because the two Hamiltonians have identical ground state densities, the expectation value can be written also like

$$\langle\Psi^2|\,\hat{H}^1\,|\Psi^2\rangle = \langle\Psi^2|\,\hat{H}^2\,|\Psi^2\rangle + \int d\vec{r}[V^1_{ext}(\vec{r}) - V^2_{ext}(\vec{r})]\rho_0(\vec{r}) \tag{3.14}$$

doing the same exchanging the labels

$$\langle\Psi^1|\,\hat{H}^2\,|\Psi^1\rangle = \langle\Psi^1|\,\hat{H}^1\,|\Psi^1\rangle + \int d\vec{r}[V^2_{ext}(\vec{r}) - V^1_{ext}(\vec{r})]\rho_0(\vec{r}) \tag{3.15}$$

adding these two inequalities, we obtain a contradiction, $E^1 + E^2 < E^2 + E^1$. Thus, the theorem has been proved.

3.2.2 2nd Theorem

"The energy $E[\rho]$ exists and can be written in terms of the charge density. Then, the exact ground state can be obtained variationally and it is related to the global minimum for this density functional".

Due to the fact that the external potential is uniquely determined by the density and also the potential uniquely determines the ground state of the system, all the other observables of the system, such as the kinetic energy, are also uniquely determined. One may write the energy as a functional of the density,

$$E[\rho] = T[\rho] + E_{int}[\rho] + \int V_{ext}(\vec{r})\rho(\vec{r}) = F[\rho] + \int V_{ext}(\vec{r})\rho(\vec{r}) \tag{3.16}$$

where $F[\rho]$ is an universal functional because the treatment of the kinetic and internal potential energies are the same for all the systems. In the ground state the energy is defined by the unique ground state density $\rho^1(\vec{r})$,

$$E^1 = E[\rho^1] = \langle\Psi^1|\,\hat{H}^1\,|\Psi^1\rangle \tag{3.17}$$

Due to the variational principle, a different density $\rho^2(\vec{r})$ will give a higher energy, because it does not describe the ground state,

$$E^1 = E[\rho^1] = \langle\Psi^1|\,\hat{H}^1\,|\Psi^1\rangle < \langle\Psi^2|\,\hat{H}^1\,|\Psi^2\rangle = E^2 \tag{3.18}$$

From this, we get that to minimizing with respect to $\rho(\vec{r})$ the total energy of the system (written as a functional of $\rho(\vec{r})$), we find the total energy of the ground state.

Then the ground state density is the correct density that minimizes the energy.

Now we have presented the first steps that made the birth of DFT possible, we can say formally that DFT allows to write the energy of N interacting electrons in the presence of an external potential as a functional of the total electron density. Thus, we have the scalar field $\rho(\vec{r})$, and DFT brings to us the solution not taking into account the $3N$ electronic variables, but the field ρ with the three coordinates instead. The total energy is thus written as

$$E[\rho] = T[\rho] + U[\rho] + \int dr^3 r \rho(\vec{r}) V_{ext}(\vec{r}) \tag{3.19}$$

here, the first term describes the kinetic contribution, the second is the electron-electron Coulomb repulsion and the third one corresponds to the existence of an external potential that also takes into account the nuclei-electron interaction and other one-particle potentials as well.

The term describing the Coulomb interaction

$$U[\rho] = \sum_{i \neq j} \int d^3 r_1 ... \int d^3 r_N \frac{|\Psi_0|^2}{2|r_i - r_j|} \tag{3.20}$$

represents a difficulty when we need to find the states and energies described by the Electronic Hamiltonian. There are two contributions to this term, one is the classical Coulomb interaction and another one describing the purely quantum effects. We write the Coulomb interaction in the following form

$$U[\rho] = \frac{1}{2}[\int d^3 r_1 \int d^3 r_2 \frac{\rho(\vec{r_1})\rho(\vec{r_2})}{|\vec{r_1} - \vec{r_2}|} + \int d^3 r_1 \int d^3 r_2 \frac{f_2(\vec{r_1}, \vec{r_2})}{|\vec{r_1} - \vec{r_2}|}], \tag{3.21}$$

where f_2 is a function resulting from the difference between the reduced density matrix [70] and the product of the electronic densities

$$f_2(\vec{r_1}, \vec{r_2}) = \gamma(\vec{r_1}, \vec{r_2}) - \rho(\vec{r_1})\rho(\vec{r_2}), \tag{3.22}$$

being the reduced matrix density:

$$\gamma(\vec{r_1}, \vec{r_2}) = N(N-1) \int ... \int d^3r_3 ... d^3r_N |\Psi_0|^2.$$

From Eq. 3.21 we can identify the Hartree term in the Coulomb repulsion term, which is

$$U_{Hartree}[\rho] = \frac{1}{2} \int d^3r_1 \int d^3r_2 \frac{\rho(\vec{r_1})\rho(\vec{r_2})}{|\vec{r_1} - \vec{r_2}|} \tag{3.23}$$

The remaining part is responsible for the quantum effects and it's called the Exchange and Correlation Electronic interaction, whose explicit form is not well known. However, we can write this Exchange term as the difference between the functional associated with the Coulomb interaction $U[\rho]$ and the classical part, which is the Hartree term.

The effects associated to the electronic correlation can be included as taking the result from the difference between the kinetic energy functional $T[\rho]$ and the kinetic energy of N non interacting electrons $T_s[\rho]$. Usually this two terms can be written together as the exchange-correlation functional:

$$E_{xc}[\rho] = U[\rho] - U_{Hartree}[\rho] + T[\rho] - T_s[\rho], \tag{3.24}$$

and is generally the only term taken approximately.
The total energy functional is then

$$E[\rho] = T_s[\rho] + E_{ext}[\rho] + E_{Hartree}[\rho] + E_{xc}[\rho] \tag{3.25}$$

Hohenberg and Kohn showed that we can find the electronic ground state of a N interacting electrons system, however, they did not give a prescription on how we can do that.

3.3 Kohn-Sham Equations

Kohn and Sham (KS) [72] built a formalism for the application of the method that HK showed a year before. The scheme to minimize the ground state energy is based on the fictitious existence of a N non interacting electron System in such a way that the effective potential acting on this electronic system generates an electronic charge density which is exactly the same as in the interacting case. The energy of this non interacting system is

$$E_s[\rho] = T_s[\rho] + \int d^3r\rho(\vec{r})V_{eff}(\vec{r}). \tag{3.26}$$

Keeping the number of particles fixed $N = \int d^3r\rho(\vec{r})$, we can minimize the energy using the variational principle

$$\frac{\delta}{\delta\rho}[E_s[\rho] - \mu(\int d^3r\rho(\vec{r}) - N)], \tag{3.27}$$

resulting in the following

$$\frac{\delta T_s[\rho]}{\delta\rho} + V_{eff}(\vec{r}) - \mu = 0. \tag{3.28}$$

The real system energy $E[\rho]$ is minimized with the constraint $N = \int d^3r\rho(\vec{r})$. Using the variational principle, then we find an analogous equation

$$\frac{\delta}{\delta\rho}[E[\rho] - \mu(\int d^3r\rho(\vec{r}) - N)]. \tag{3.29}$$

The equation we must solve is

$$\frac{\delta T_s[\rho]}{\delta\rho} + V_{Hartree}(\vec{r}) + V_{ext}(\vec{r}) + \frac{E_{xc}[\rho]}{\delta\rho} - \mu = 0. \tag{3.30}$$

Kohn and Sham showed that the non interacting electronic density must be equal to the interacting electronic density, that is, there is an equivalence between the previous equations, which imply an expression for the effective potential in the non interacting case as

$$V_{eff}(\vec{r}) = V_{Hartree}(\vec{r}) + V_{ext}(\vec{r}) + \frac{\delta E_{xc}[\rho]}{\delta\rho}. \tag{3.31}$$

With this, the determination of the electronic charge density in the interacting system is reduced to the solution of the non interacting system under the effective potential V_{eff}. This Schrödinger-like equation is the so-called Kohn-Sham equation

$$[-\frac{1}{2}\nabla^2 - V_{eff}(\vec{r})]\psi_n^{KS}(\vec{r}) = \epsilon_n^{KS}\psi_n^{KS}(\vec{r}). \tag{3.32}$$

Then, as long as the wave function for a set of N non-interacting electrons can be written as a single Slater Determinant, the Total Energy can be written as

$$E_{Total} = \sum_n^N \epsilon_n \tag{3.33}$$

We can define with this the Fermi energy in the system as the highest occupied KS eigenvalue ϵ_F,

$$E_{Total} = \sum_n f(\epsilon_n - \epsilon_F)\epsilon_n \tag{3.34}$$

where f is the Fermi distribution. [*]
The electronic charge density is found by

$$\rho(\vec{r}) = \sum_n^N \psi_n^{KS*}(\vec{r})\psi_n^{KS}(\vec{r}) = \sum_n |\psi_n^{KS}|^2 f(\varepsilon_n - \varepsilon_F). \tag{3.35}$$

Thus, we have changed the original picture into the following, the Khon-Sham equation describes the dynamics of a single particle under the action of the other $N-1$ particles. However, even when this approach solves the many body system problem, we cannot say that the Khon-Sham wave functions $\psi_n^{KS}(\vec{r})$ describe the electrons of the interacting system and strictly speaking the eigenvalues ϵ_n don't correspond to the single particle spectrum. Nonetheless, we will, as it has been consistently done, assume that they provide a good enough approximation [79].

---

[*] Strictly speaking DFT is defined for T=0, but in practical terms a Fermi-Dirac distribution is included in calculations for numerical convergence.

The KS equations, in principle give us the ground state's properties, but as we mentioned before, there is a term (E_{xc}) we do not know exactly and we need to use some approximation to deal with it. There are two types of approximations, which are generally used, they are the *Local Density Approximation* (LDA) and the *General Gradient Approximation* (GGA) [79].

In the first approximation, we consider the E_{XC} to be that of a uniform gas of the electronic density $\rho(\vec{r})$. The exchange-correlation energy is written as

$$E_{xc}^{LSDA} = \int d^3 r n(\vec{r}) e_{xc}(\rho^{\uparrow}, \rho^{\downarrow}) \tag{3.36}$$

where e_{xc} is the exchange-correlation density for a uniform electronic gas provided by the work of Dirac and others [79], It is noted that we wrote the spin polarised case by introducing different charge populations for both spins ($LSDA$).

The second case is an extension of the previous one and takes into account terms depending on the charge density's gradient. The usual expression for this exchange-correlation energy is the PBE parametrization after Perdew-Burke-Ernzerhof [73], which is written as

$$E_{xc}^{GGA} = \int d^3 r \mathcal{D}(\rho^{\uparrow}, \rho^{\downarrow}, \nabla\rho^{\uparrow}, \nabla\rho^{\downarrow}). \tag{3.37}$$

The electronic density of the ground state must satisfies the system's symmetries, then, in the resolution of the KS equation we need to impose those symmetry constraints.

3.4 Kohn-Sham Equations in our Systems

For practical terms, usually the best approach is to write the KS wave function in some basis. Given our periodic system, we also expect the electronic density to be periodic, and using a linear combination of basis functions, the problem simplifies to finding the coefficients that minimizes the Kohn-Sham equations inside a cell using Bloch's theorem.

3.4.1 Plane Waves

Considering the reciprocal lattice vectors at some cell as $\vec{G}_n$, which can be expanded over all the space as waves like $e^{i\vec{G}_n\cdot\vec{R}_n}$, the Plane wave method offers the possibility to expand the effective potential over a Fourier series

$$V_{eff}(\vec{r}) = \sum_{\vec{G}_n} V_{eff}^{\vec{G}_n} e^{i\vec{G}_n\cdot\vec{R}_n}, \tag{3.38}$$

and the same for the KS wave functions

$$\psi_{n\vec{k}}^{KS}(\vec{r}) = \sum_{\vec{G}_n} C_{\vec{k}+\vec{G}_n}^{n} e^{i(\vec{k}+\vec{G}_n)\cdot\vec{r}}. \tag{3.39}$$

Now we have a basis set, replacing them in the original KS equation to find

$$\sum_{\vec{G}_n}[\frac{1}{2}(\vec{k}+\vec{G}_n)^2\delta_{\vec{G}_n,\vec{G'}_n} + V_{\vec{G}_n,\vec{G'}_n}]C_{\vec{k}+\vec{G}_n}^{\alpha} = \varepsilon_{\alpha\vec{k}}^{KS} C_{\vec{k}+\vec{G}_n}^{n}, \tag{3.40}$$

where

$$V_{\vec{G}_n,\vec{G'}_n} = \int_{unit\ cell} d^3r V_{eff}(\vec{r}) e^{i(\vec{G}_n-\vec{G'}_n)\cdot\vec{r}}, \tag{3.41}$$

and the ground state charge density is determined by the calculations of the C^{α} coefficients and the eigenenergies ε_{α}.

Plane waves look as the natural choice since it is equivalent to a complex Fourier expansion of the real-space wave function, besides the fact that we have the availability of techniques with great accuracy that involve FFT (Fast Fourier Transform) calculations. Furthermore, there is only one parameter controlling the quality in this approach, and it's the number of $\vec{k}$ vectors used. This supposes that the number of these vectors depend on the specific system under study, then, the larger the number of vectors we take, the more accurate the calculation will be, but also the more computation power we'll need.

3.5 Localised Basis

Another basis that we can take, is a set of localised orbitals basis. In this approach we take the wave functions as if they are periodic in the reciprocal $\vec{k}$ space. Expanding the KS functions in terms of this localised basis,

$$\psi^{KS}_{\alpha\vec{k}}(\vec{r}) = \sum_{\vec{R}_n} \varphi^{\alpha\vec{k}}(\vec{r} - \vec{R}_n) e^{i\vec{R}_n\cdot\vec{k}}, \tag{3.42}$$

this expansion takes the functions φ as centered in atom contained in the unit cell localised at position $\vec{R}_n$. This expansion is know as the Linear Combination of Atomic Orbitals (LCAO).

With this choice we now get certain advantages such as the fact that: the range of interaction is finite. This means that the Hamiltonian matrix elements go to zero for orbitals that are far apart, therefore the Hamiltonian and Overlap matrix elements, $S_{i,j} = \langle\varphi_i|\varphi_j\rangle$, become relatively sparse, reducing the computational effort.

This kind of approach is used in *SIESTA* [74](Spanish Initiative for Electronic Structure Calculations with Thousands of Atoms), which is the choice we made to study our systems.

3.6 SIESTA Code

Before we get into the description of SIESTA, it's important to comment something about the Pseudopotentials, which is a feature the code uses in order to perform the calculations. The pseudopotential method allows for a significant reduction on the number of degrees of freedom for the problem. Since there will be bonds between atoms, and the existence of them relies on the more external or valence electrons, we can, in principle, treat the core electrons in such as "frozen", this way the wave function for the problem, behaves smoothly in the core region, under the influence of a potential that contains a contribution of the effect of the nuclei and the core electrons.

Philips and Kleinman [75] obtained the first pseudopotentials using the methodology of the OPW (Orthogonalized Plane Wave) Method. Their work was based on the linear combination of valence wave pseudo functions $|\varphi_v\rangle$ and core wave functions $|\varphi_c\rangle$

$$|\psi_n\rangle = |\varphi_v\rangle + \sum_c a_c\,|\varphi_c\rangle \tag{3.43}$$

with $\langle\varphi_c|\psi_n\rangle = 0$ as a constraint.

This gave rise to the *Norm Conserving* proposals [79] which are of importance for our DFT calculations. Zunger and Cohen [76] were the first in the development of these pseudopotentials, which consist in using a Schr$\ddot{o}$dinger-like equation for the free particle ($V(r) = 0$) with the inclusion of the pseudopotential. The radial part of the equations is

$$[-\frac{1}{2}\frac{d^2}{dr^2} + \frac{l(l+1)}{2r^2} + V^l_{\mu s}(r)]P_{\mu s,l}(r) = \varepsilon_l P_{\mu s,l}(r). \tag{3.44}$$

By rewriting it in appropriate form

$$V^l_{\mu s}(r) = \varepsilon_l - \frac{l(l+1)}{2r^2} + \frac{1}{2}\frac{P''_{\mu s,l}(r)}{P_{\mu s,l}(r)}, \tag{3.45}$$

where V^l is the screened pseudopotential component with quantum number l, ε is the valence energy eigenvalue with quantum number l and $P_{\mu s,l}$ are the eigenfunctions in the radial part in this pseudopotential with its second derivative P''_l.

The problem then is to find a pseudo function in such way that its behaviour beyond a cut-off radius is equal to the function in the effective potential

$$P_{\mu s,l} = \begin{cases} r^{l+p}f(r), & r < r_c, \\ P_l(r), & r > r_c, \end{cases} \tag{3.46}$$

where $P_l = rR_l(r)$ with $R_l(r)$ as the radial part of the solution of the system taking the system with all the electrons, and the function $f(r)$ is chosen taking the following form

$$f(r) = exp(\sum_{i=0}^{n} a_i r^i), \tag{3.47}$$

and the parameter p can take values $p = 1$ or $p = 2$. The choice will depend on the system we are dealing with, and also the parameter a_i will be chosen to fits well with the real function in the r_c point. Taking the constraint of the norm conservation we have that this pseudo wave function integrated from zero to r_c must be equal to the real density charge.

The basis set in SIESTA is obtained from the solved Schrödinger equations for isolated atoms immersed in a hard-wall potential (pseudopotential), this solution has the following form

$$\phi_{n,l,m}(r, \theta, \varphi) = R_{n,l} Y_{l,m}(\theta, \varphi) \tag{3.48}$$

where R is the normalised radial part and Y is the real spherical harmonics (n, l and m are the quantum numbers).

We will repeat some notions of the pseudopotential method, but now in the context of the SIESTA code. As we mentioned before, dealing with the pseudopotential framework allows us to neglect the core electrons, so reducing the computational work, and also is a potential smoother than the actual all-electron potential. The pseudopotential was initially written in semi-local form, this is, there was a different radial potential for each angular momentum. This concept finally was modified by Kleinman and Bylander [77] who finally proposed the full non-local form.

The variational freedom offered by SIESTA gives us the chance to include empty orbitals, in order to increase the Hilbert space where our system is represented. For instance it provides the option to include multiple-ζ basis set [74]. In this approach, each of the ζ orbitals has the same spherical harmonics present in the above atoms, but is the radial part which takes a new form constructed from a new function with the split-valence method. Here the radial part of our second-ζ retains the tail of the first-ζ outside a split radius r_l^s and has a polynomial form inside:

$$R_{n,l}^{2\zeta} = \begin{cases} r^l(a_l - b_l r^2), & if \quad r < r_c, \\ R_{n,l}^{1\zeta}(r), & if \quad r > r_c. \end{cases} \tag{3.49}$$

The constants a_l and b_l are determined by matching the wave function and its first derivative.

We can proceed from the other end; where the radial function $R_{n,l}(r)$ remains the same while we can use higher orbital angular momentum for the spherical harmonics, this basis is known as polarised orbitals,

$$\phi_{n,l',m} = R_{n,l} Y_{l+1,m} \tag{3.50}$$

where $-(l+1) < m < l+1$. Besides the fact that the variational freedom becomes larger in the minimisation procedure, it is now allowed to construct basis functions with higher angular momentum than the largest allowed by the pseudopotential. In this framework, the Overlap matrix S_{ij} is defined as

$$S_{ij} = \int d^3r \phi_{i'}(\vec{r} - \vec{R}_A)\phi_{j'}(\vec{r} - \vec{R}_B) \tag{3.51}$$

where $i = \{i', A\}, j = \{j', B\}$ and $\vec{R}_\alpha$ is the position of the atom α.

The calculation is usually initialized with a charge density ρ_0 obtained from the isolated atoms involved in the system and then it's used to obtain the potential in real space. Using FFT (Fast Fourier Transform) techniques, the Hartree potential is obtained by solving the Poisson Equation, with the requirement that this potential must be periodic. The exchange and correlation potentials can be obtained using either the LDA or GGA approaches. The Kohn-Sham Hamiltonian then is written as

$$\begin{aligned} H_{ij} = -\frac{\hbar}{2m} \int d^3r \phi_i(\vec{r} - \vec{R}_A)\nabla^2\phi_j(\vec{r} - \vec{R}_B) + \\ \int d^3r \phi_i(\vec{r} - \vec{R}_A) V_{eff} \phi_j(\vec{r} - \vec{R}_B). \end{aligned} \tag{3.52}$$

Since we are dealing with periodic system we need to write also the coupling to the periodic mirrors of the unit cell

$$H_{ij}(\vec{k}) = \sum_{\alpha} H_{ij}^{\alpha} e^{i\vec{k}\cdot\vec{r}_{\alpha}}, \tag{3.53}$$

where $\vec{r}_{\alpha}$ is the relative position between the 0-th and the α-th unit cells. The Overlap matrix can be obtained by performing the same calculation.

The Hamiltonian is then diagonalised to obtain the coefficients c_{α}^{n} for the eigenvector ψ_n appearing in the KS equation

$$\psi_n(\vec{r}) = \sum_{n} c_{\alpha}^{n} \phi_{\alpha}(\vec{r}). \tag{3.54}$$

This leads us the Density Matrix

$$D = \sum_{m}^{N_{E_F}} \left|\psi_m\right\rangle \left\langle\psi_m\right| = \sum_{m}^{N_{E_F}} \sum_{n} \sum_{p} c_{m}^{n} c_{m}^{p*} \left|\phi_n\right\rangle \left\langle\phi_p\right| \tag{3.55}$$

with N_{E_F} being the number of occupied states up to the Fermi energy. The matrix elements of this Density matrix are

$$D_{np} = \sum_{m} c_{m}^{n} c_{m}^{p*} f(\varepsilon_m - E_F), \tag{3.56}$$

and finally the quantity that describes our system, the charge density, is the sum of the diagonal elements of D in the coordinate representation

$$\left\langle\vec{r}\right| D \left|\vec{r}\right\rangle = \rho(\vec{r}) = \sum_{np} \phi_n(\vec{r}) D_{np} \phi_p(\vec{r}) \tag{3.57}$$

The procedure is performed in a self-consistent way, namely: We initially start with the charge density ρ_0 described above, in order to obtain the effective potential V_{eff}. Once the Hamiltonian H_{ij} is written we can diagonalise it to find the KS eigenstates which will provide us a new density matrix, ergo a new charge density. The procedure is repeated until a convergence criterion is satisfied

$$||\rho^{j} - \rho^{j+1}|| < \delta \tag{3.58}$$

where δ is a tolerance parameter.

3.7 Spin-Orbit Coupling in SIESTA

So far we didn't introduce relativistic effects in the treatment of this many body problem. Therefore, in order to explain the effects related to the SOC in our system, we need to perform a modification in the way SIESTA works. Since now we deal with relativistic effects, as long as we use the Norm Conserved Pseudo-potential approach , we need to address these effects in the generation of such pseudo-potentials, this means that the Schr$o$dinger equation describing the valence electrons must be changed to the Dirac equation.

We start from the radial part of the Dirac equation which is shown in Appendix A. If we consider ε as the energy of the valence electrons under $V(r)$, and we take this effective potential as the potential felt outside the core region, there comes out a relation between the solutions $G(\vec{r})$ and $F(\vec{r})$ for the Dirac equation

$$F(\vec{r}) = \frac{1}{2}\lambda[\frac{dG(\vec{r})}{dr} + (\kappa/r)G(\vec{r})]. \tag{3.59}$$

From this relation, now we can obtain an equation for the G component, associated with the negative energy wave function of the Dirac equation

$$\frac{1}{2}(\frac{d^2G}{dr^2} + \frac{\kappa(\kappa+1)}{r^2}G) + [V(r) - \varepsilon]G = 0, \tag{3.60}$$

In the case of heavy atoms, the negative energy radial part $f(r) = F(r)/r$ is strongly mixed with its positive energy counterpart radial part. The Spin-Orbit Coupling operator has the eigenvalues

$$\kappa = \begin{cases} j + \frac{1}{2} = l, & \kappa > 0, \\ -(j + \frac{1}{2}) = -(l+1), & \kappa < 0, \end{cases} \tag{3.61}$$

this means that for every κ value, there is radial wave function written in terms of angular momentum:$G_{l+\frac{1}{2}}(r)$ and $G_{l-\frac{1}{2}}(r)$.

In a similar way the pseudopotential operator was constructed for the non relativistic case, Kleinman [86] showed that we can solve self-consistently the all-electron Dirac equation for a single atom, in order to obtain the pseudo-potentials V_j where j is the total angular momentum $j = l{+}s$. From that procedure we find the pseudo-potential operator for the relativistic case

$$\hat{V}_{ps}^{ion}(r) = \sum_{l,m}[|\chi_M^J\rangle\, V_{ps}^{ion(l+\frac{1}{2})}(r)\, \langle\chi_M^J| + |\chi_{M'}^{J'}\rangle\, V_{ps}^{ion(l-\frac{1}{2})}(r)\, \langle\chi_{M'}^{J'}|], \tag{3.62}$$

where $J = l + \frac{1}{2}$,$M = m + \frac{1}{2}$,$J' = l - \frac{1}{2}$,$M' = 1 - \frac{1}{2}$, and $V_{ps}^{ion(l\pm\frac{1}{2})}(r)$ is the pseudo-potential that takes the relativistic effects up to first order, and also changes the core potential for each value of the angular moment.

Changing the angular functions, the operator is written

$$\hat{V}_{ps}^{ion} = \hat{V}_{sc} + \hat{V}_{SO} = \sum_{l,m}[V_{sc}^l(\vec{r})\mathbb{I}_\sigma + V_{SO}^l(\vec{r})\vec{L}\cdot\vec{S}]\,|l,m\rangle\,\langle l,m|\,, \tag{3.63}$$

where $\mathbb{I}_\sigma$ is the identity matrix in spin space,

$$V_{sc}^l = \frac{2}{2l+1}[(l+1)V_{ps}^{(2)(l+\frac{1}{2})}(r) + lV_{ps}^{(2)(l-\frac{1}{2})}(r)] \tag{3.64}$$

is the scalar relativistic correction, and

$$V_{SO}^l(r) = \frac{1}{2l+1}[(V_{ps}^{(2)(l+\frac{1}{2})}(r) - V_{ps}^{(2)(l-\frac{1}{2})}(r)]. \tag{3.65}$$

Here $V_{ps}^{(2)(l\pm\frac{1}{2})}(r)$ is the pseudo-potential for every value of the total angular moment and is obtained from the inversion of the radial part of the Dirac equation. Finally the total Hamiltonian for the relativistic case is

$$\hat{H} = \hat{T} + \hat{V}^{sc} + \hat{V}^{SO} + \hat{V}^H + \hat{V}^{xc}, \tag{3.66}$$

where besides the parts involving the SOC and scalar relativistic correction, we also have the kinetic, *Hartree* and exchange contributions.

In general terms, the Hamiltonian matrix can be written in the following matrix block form:

$$\hat{H} = \begin{bmatrix} \hat{H}^{\uparrow\uparrow} & \hat{H}^{\uparrow\downarrow} \\ \hat{H}^{\downarrow\uparrow} & \hat{H}^{\downarrow\downarrow} \end{bmatrix},$$

where the off diagonal blocks arise from the spin-orbit potential as well as from the exchange and correlation potentials whether the system includes a non-collinear spins.

In order to compute and solve this Hamiltonian we can use an approach suggested by Fernandez-Seivane et al. [78], The Spin-orbit LCAO scheme, which takes an on-site approximation. The $|\psi_n\rangle$ is expanded over a set of localised orbitals $|\phi_i\rangle$,

$$|\psi_n\rangle = \sum_i \begin{pmatrix} c^{\uparrow}_{n,i} \\ c^{\downarrow}_{n,i} \end{pmatrix} |\phi_i\rangle$$

,

where i is a collective index representing all the quantum numbers involved for a given ϕ_i orbital.

The Kohn-Sham equation in this basis then is transformed into

$$\begin{bmatrix} H^{\uparrow\uparrow}_{ij} - E_n S_{ij} & H^{\uparrow\downarrow} \\ H^{\downarrow\uparrow} & H^{\downarrow\downarrow} - E_n S_{ij} \end{bmatrix} \begin{bmatrix} c^{\uparrow}_{n,j} \\ c^{\downarrow}_{n,j} \end{bmatrix} = 0.$$

Here $H^{\sigma\sigma'}_{ij} = \langle\phi_i| \hat{H}^{\sigma\sigma'} |\phi_j\rangle$ and $S_{ij} = \langle\phi_i|\phi_j\rangle$, are matrix elements of the Hamiltonian and overlap respectively. The spin-orbit term can be calculated as

$$V^{SO}_{ij} = \langle\phi_i| \hat{V}^{SO} |\phi_j\rangle$$

$$= \sum_{k,l_k,M_k} \langle\phi_i| \bar{V}^{SO}_{l_k} \vec{L} \cdot \vec{S} \,|l_k; M_k\rangle \langle l_k; M_k|\phi_j\rangle \tag{3.70}$$

where index k indicates the atom on which the potential is centered, $\bar{V}_{l_k}^{SO} = \bar{V}_l^{SO}(\vec{r} - \vec{d_k})$ and $|l_k; M_j\rangle$, the spherical harmonic centered at the same atom, it's located at position $\vec{d_k}$. A way to avoid a great computational effort, is constructing fully non-local pseudo-potentials. The short-ranged nature of the spin-orbit pseudo-potential radial part, $\bar{V}_l^{SO}$, makes that we have a quickly decay in the matrix elements with the distances among the three centers [78]. Therefore the only matrix elements considered are ones associated to orbitals on the same atom. As a result now we just need to work with one center integrals whose the matrix elements are given by

$$\begin{aligned} V_{ij}^{SO} &= \frac{1}{2} \sum_{k, l_k > 0, M_k} \langle R_{n_i, l_i} | \bar{V}_{l_k}^{SO} | R_{n_j, l_j} \rangle \langle l_i, M_i | \begin{pmatrix} \hat{L}_z & \hat{L}_- \\ \hat{L}_+ & -\hat{L}_z \end{pmatrix} | l_k, M_k \rangle \langle l_k, M_k | l_j, M_j \rangle \\ &\simeq \frac{1}{2} \langle R_{n_i, l_i} | | \bar{V}_{l_i}^{SO} | R_{n_j, l_i} \rangle \langle l_i, M_i | \begin{pmatrix} \hat{L}_z & \hat{L}_- \\ \hat{L}_+ & -\hat{L}_z \end{pmatrix} | l_i, M_j \rangle \, \delta_{l_i, l_j}, \end{aligned} \quad (3.71)$$

since the $\hat{L}_\alpha$ operators leave each l_i subspace invariant. The angular part of these on-site matrix elements can be calculated.

Finally using symmetry arguments it's easy to show that, besides the hermitian nature of the matrix elements, all the terms in the Hamiltonian satisfy a *spin* box hermiticity,

$$H_{ij}^{\sigma\sigma'} = (H_{ij}^{\sigma'\sigma})^* \quad (3.72)$$

except for the spin-orbit contribution which is *spin* box anti-hermitian, this has direct implications in the calculation of the total energy. The procedure described above has been implemented in SIESTA [74] and can be used to simulate the properties of different systems under the influence of spin orbit interaction.

Chapter 4

Results

In this chapter we present simulations of various two dimensional materials and heterolayers formed by stacking different layers with or without defects. In order to obtain the electronic properties of heterostructure 2D systems, and the later modification in their band structure when spin-orbit coupling is included. We performed *ab initio* density functional theory calculations using SIESTA. In all the cases we used a double-ζ polarized basis set (DZP) for valence electrons, a 250 Ry for Mesh-cut-off and norm-conserving pseudo-potentials. A k-sampling Monkhorst-Pack scheme [81], where depending on the system we use a k-point grid which will be commented for each of the systems. The Local Density Approximation (LDA) as proposed by Ceperly and Alder(CA) [87] for the exchange-correlation functional was employed. As we are dealing with 2D systems, enough vacuum in the direction perpendicular to the sheet was considered as to avoid spurious interaction between images. In all the cases the systems were fully relaxed using a conjugate gradient (CG) method to obtain the equilibrium structures such that on each atom the force experienced was no greater than 0.01 eV/$\AA$.

4.1 Isolated Structures

4.1.1 Graphene

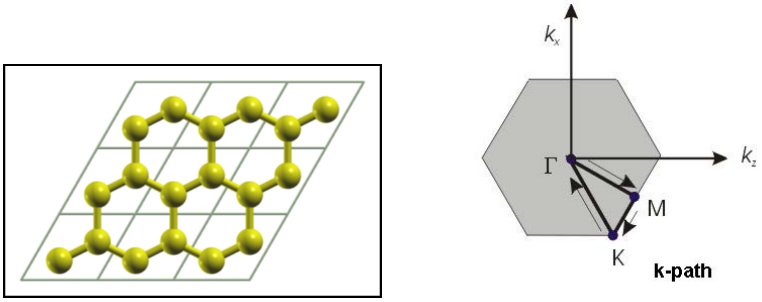

(a) Ball-and-stick representation on graphene, the unit cell containing two inequivalent carbon atoms.

(b) Brillouin zone for a hexagonal cell showing some high-symmetry points.

Figure 4.1: Graphene hexagonal lattice and firt Brillouin zone.

We start with the case of pristine Graphene which exhibits the structure shown in figure 4.1.a The figure shows a 3 × 3 super-cell, where every unit cell on it has two carbon atoms belonging to the two different sub-lattices (A and B). For this case we set a k-point grid of $12 \times 12 \times 1$, mesh-cut-off of 180 Ry and energy shift of 0.01 eV. In the direction perpendicular to the sheet a vacuum region of 20 $\mathring{A}$ was used. Fig. 4.2.a shows the band structure for a general path on the first Brillouin zone, the path selected can be seen in Fig. 4.1.b, the Dirac point is present at K point. For Fig. 4.2.b SOC was included , however in Graphene; a light system, the effects are negligible and no changes are present for the band structure as well as for the Projected density of states. In the Band structure we can see that from the two lines drawing the Dirac cone, blue (solid) and red (dashed) lines are indistinguishable in energy.

The figure 4.3 tries to show the little splitting produced by the inclusion of the Spin

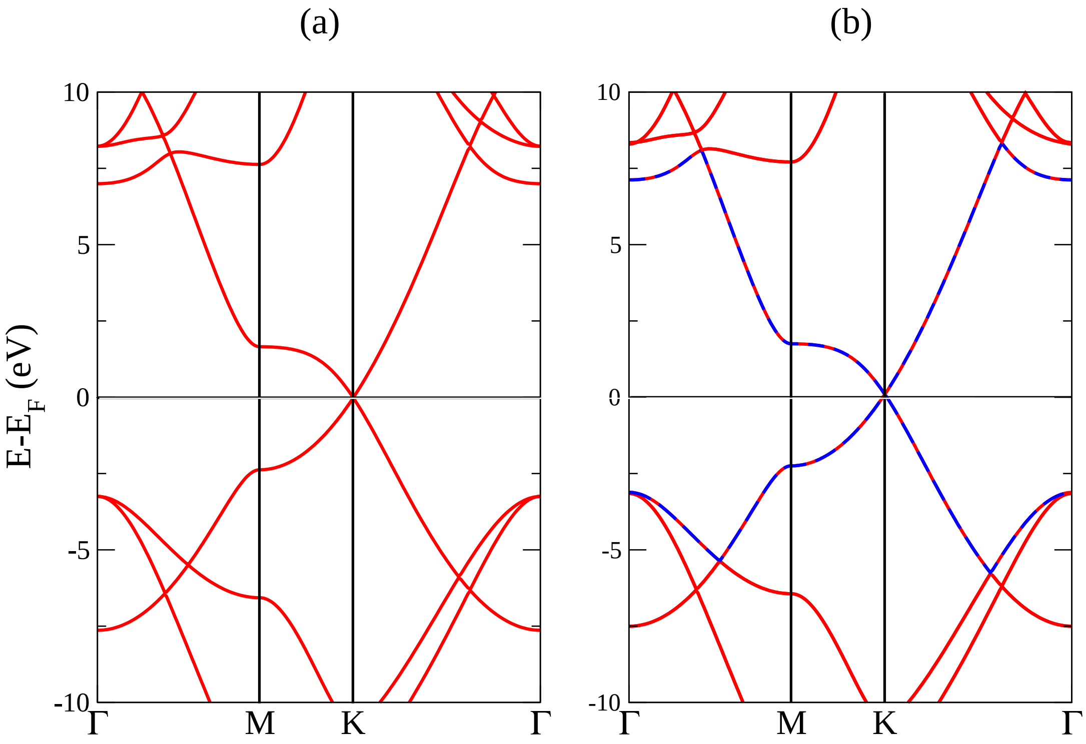

Figure 4.2: Electronic Band structure for graphene (a) with and (b) without spin-orbit coupling.

orbit coupling, to do so, the k points employed were much more than in the previous calculation, because the K point is also invariant under inversion symmetry there are no spin split bands,but a little gap is opened.

Fig. 4.4 shows the Projected Density of states for Graphene. Our results are in accordance with calculations performed by others [17,93]. They show that most of the contribution to frontier bands are associated with p_z orbitals.

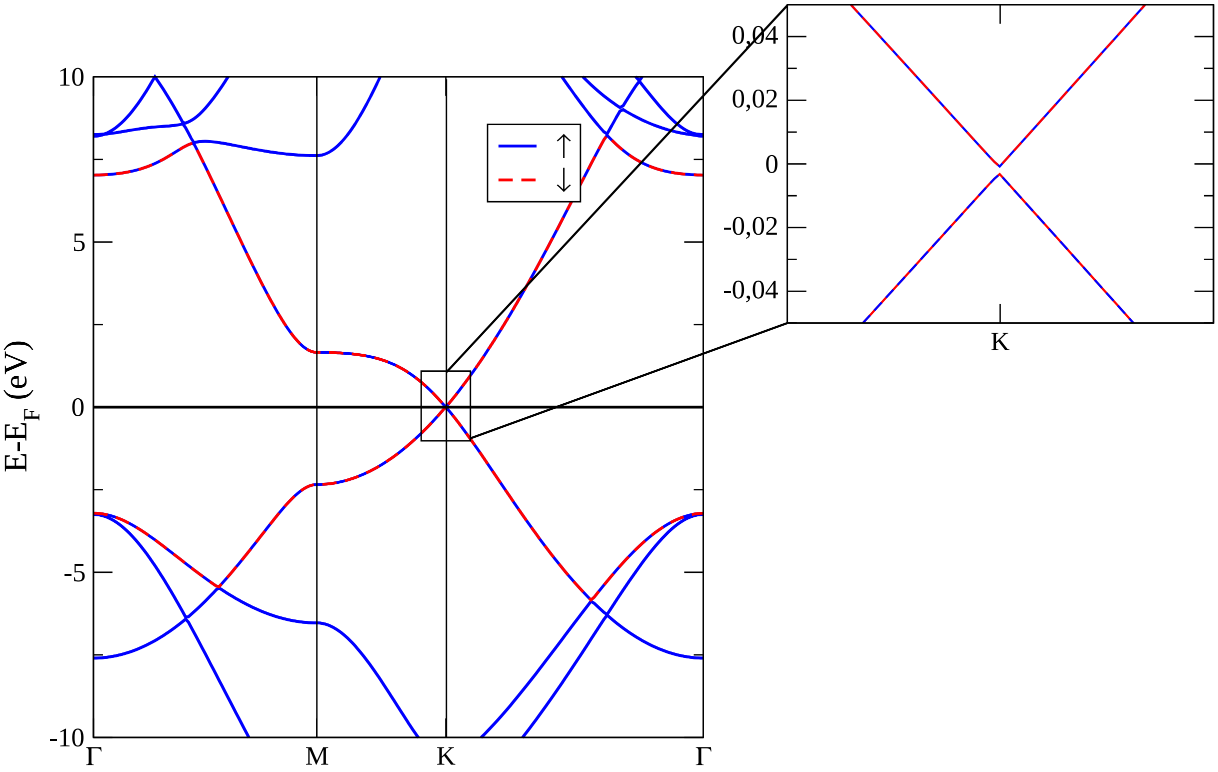

Figure 4.3: Graphene band splitting at K point as the result of the SOC inclusion.

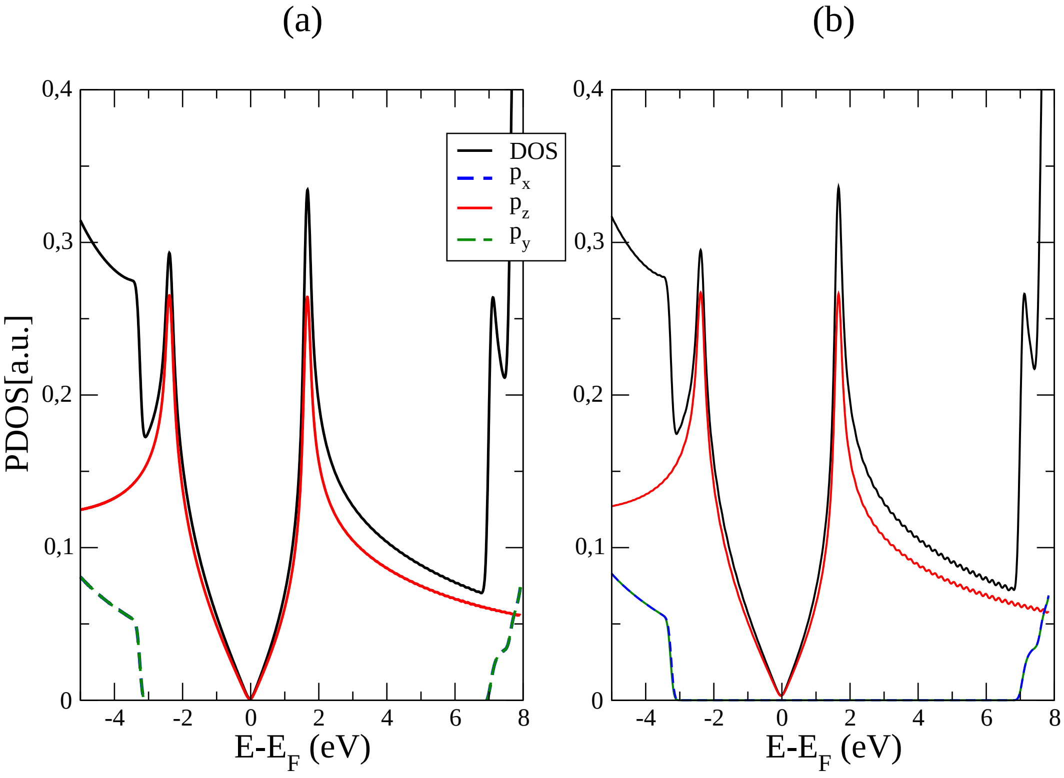

Figure 4.4: Graphene Projected Density of states for (a) without and (b) with spin orbit coupling.

4.1.2 Phosphorene

As mentioned before, phosphorene has a puckered structure. The unit cell comprises four Phosphorus atoms, where two atoms belong to the lower plane and the other two are in the upper one. Fig. 4.5 shows the structure of phosphorene which has an orthorhombic cell. The cell vectors $\vec{a}$ and $\vec{b}$ are shown and also some structural parameters

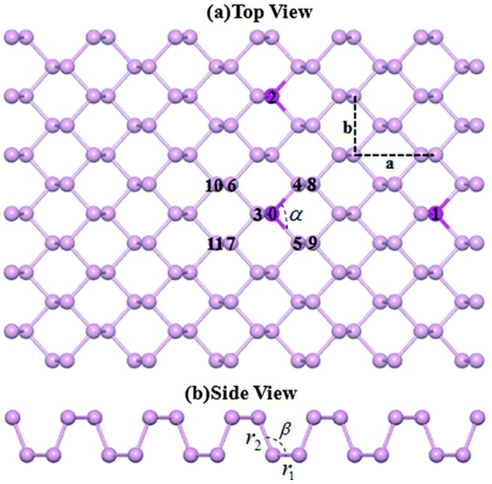

Figure 4.5: (a) Top and (b) side view of phosphorene structure. The lattice parameters as well as other internal structural parameters are shown.

The structure and the electronic properties were calculated employing a k-point grid of $10 \times 10 \times 1$, with a mesh-cut-off of 180 Ry and energy-shift of 0.01 eV. The vacuum region the direction perpendicular to the sheet was taken as 30 $\mathring{A}$. Because Phosphorene is very sensitive to strain we were obliged to ensure that forces on each atom were smaller than 0.001 $\mathring{A}$. Since the unit cell is orthorhombic, so will be the Brillouin zone (shown in Fig. 4.6). The band structure for the cases with and without SOC is shown in Fig. 4.7. As discussed in chapter 1, the band gap is direct at the Gamma point and the bands are highly anisotropic in the Γ-X and Γ-Y directions. We find from the structure a gap near 1 eV present at the Γ point which is near to the experimental value previously commented.

	Our results	Reference Values [89]
α	96.17°	98.15°
β	103.12°	103.69°
r_1 [$\mathring{A}$]	2.22	2.16
r_2 [$\mathring{A}$]	2.25	2.21
r_{05} [$\mathring{A}$]	2.21	2.16
r_{45} [$\mathring{A}$]	3.30	3.27

Table 4.1: Phosphorene structural parameters obtained after relaxation.

Table 4.1 shows the structural parameters obtained after relaxation. The values obtained are in good agreement with the experimental data [94].

One interesting feature about the electronic band structure is that from Y to X points in the Brillouin zone, the bands are glued and remain degenerated, this has to do with the non-symmorphic nature of the symmetry group for this case.

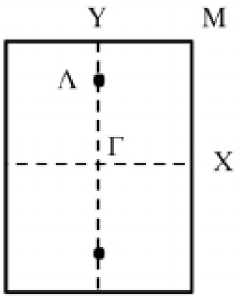

Figure 4.6: Orthorhombic Brillouin zone showin some of the High symmetry points.

In the PDOS there are no changes comparing the SOC free case and the system with SOC. Fig. 4.8 shows the total and projected density of states for phosphorene. Results showed us that major contributions for valence band are coming from p_x and p_z orbitals, while p_y is more present near the bottom of the counduction band,

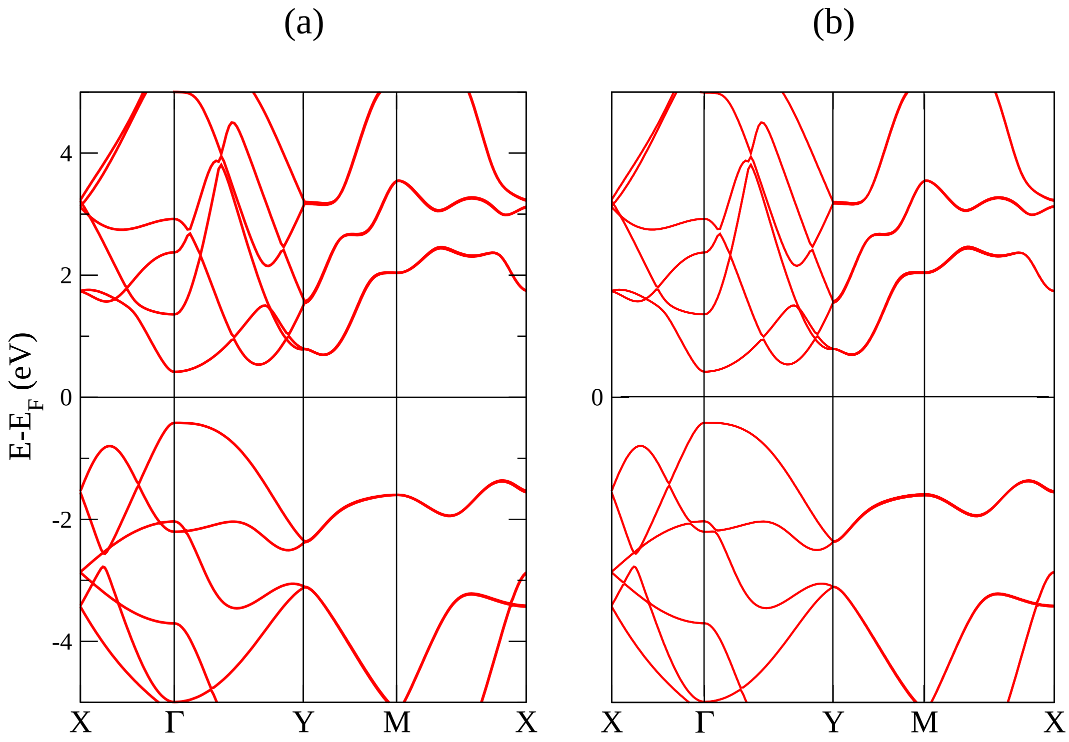

Figure 4.7: Electronic band structure for phosphorene (a) without and (b) with spin orbit coupling.

which is different from the Graphene case. However, our calculations show that SOC has little effect when we are dealing with light atom systems like graphene and phosphorene.

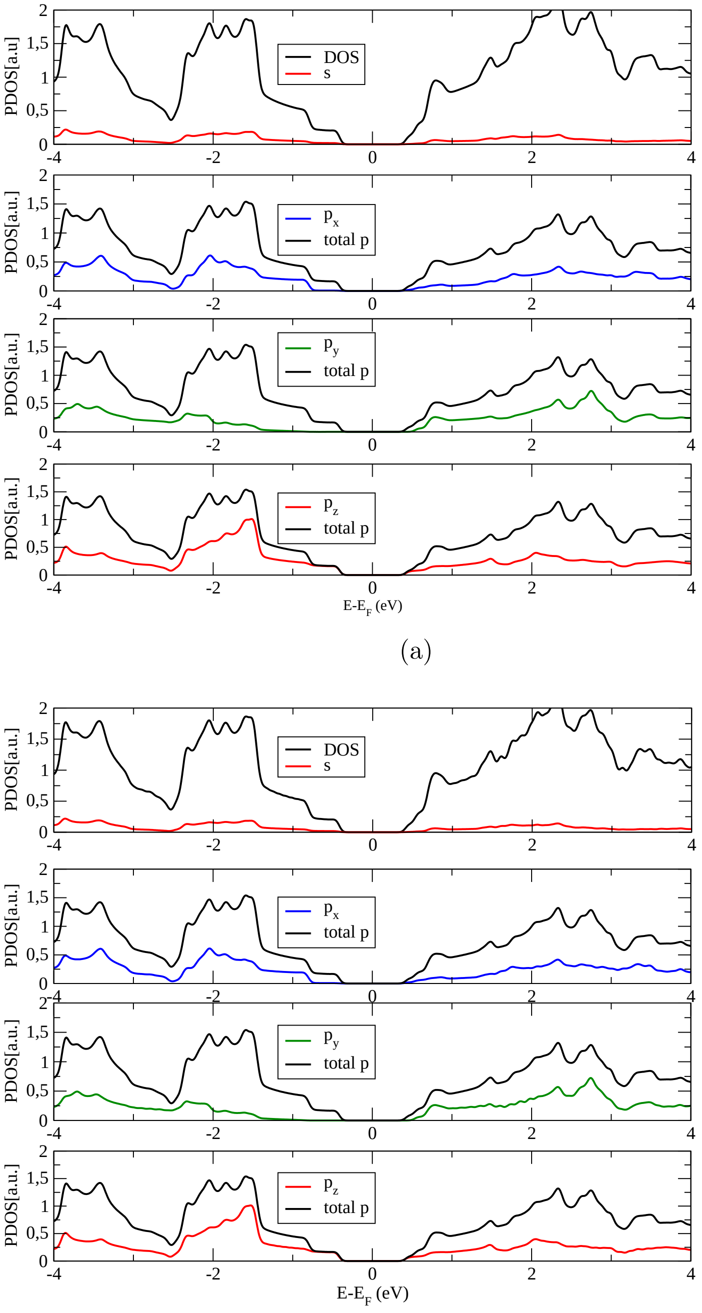

(a)

(b)

Figure 4.8: Total and Projected Density of states for phosphorene monolayer (a) without and (b) with spin orbit coupling.

4.1.3 $MoTe_2$

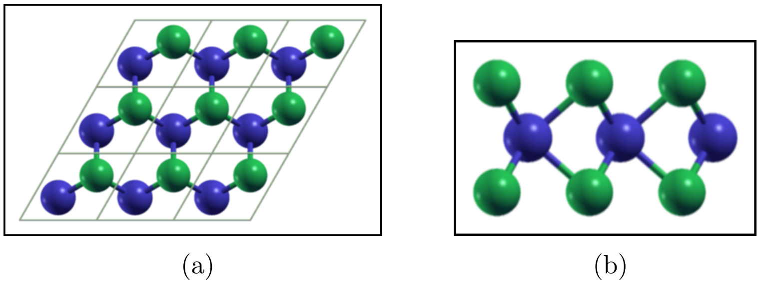
(a)
(b)

Figure 4.9: Top (a) and side (b) view for $MoTe_2$ honeycomb lattice

$[\mathring{A}]$	$MoTe_2$
a_0	3.536
d_{X-X}	3.606

Table 4.2: Values for the lattice parameters a_0 and distance between chalcogenide atoms d_{X-X}.

As mentioned previously, the dichalcogenides form an hexagonal structure such as the one shown in Fig. 4.9. The procedure followed in order to obtain the electronic structure was to use a k-point grid of $12 \times 12 \times 1$ as in the case of phosphorene. The relaxation was performed until the forces were lower than 0.001 eV/ $\mathring{A}$, and the vacuum region in the transverse direction was 30 $\mathring{A}$. The converged lattice parameter a_0 and the height of the sheet d_{X-X} (the distance between two transverse X=Te atoms) are presented in table 4.2.

The band structure without SOC is shown in Fig. 4.10.a. They are in agreement with previous calculations using LDA/GGA [56], while the band gap obtained in our case (around 1 ev) is significantly smaller than experimental values (as well as for other levels of theory such as GW [56]) overall the bands compare well except for a rigid shift. For the SOC-enabled claculations presented in Fig. 4.10.b the results showed modifications in the band structure Indeed, a big splitting at the K

point and significant splitting below the top of the valence band as well as above the bottom of the conduction band.

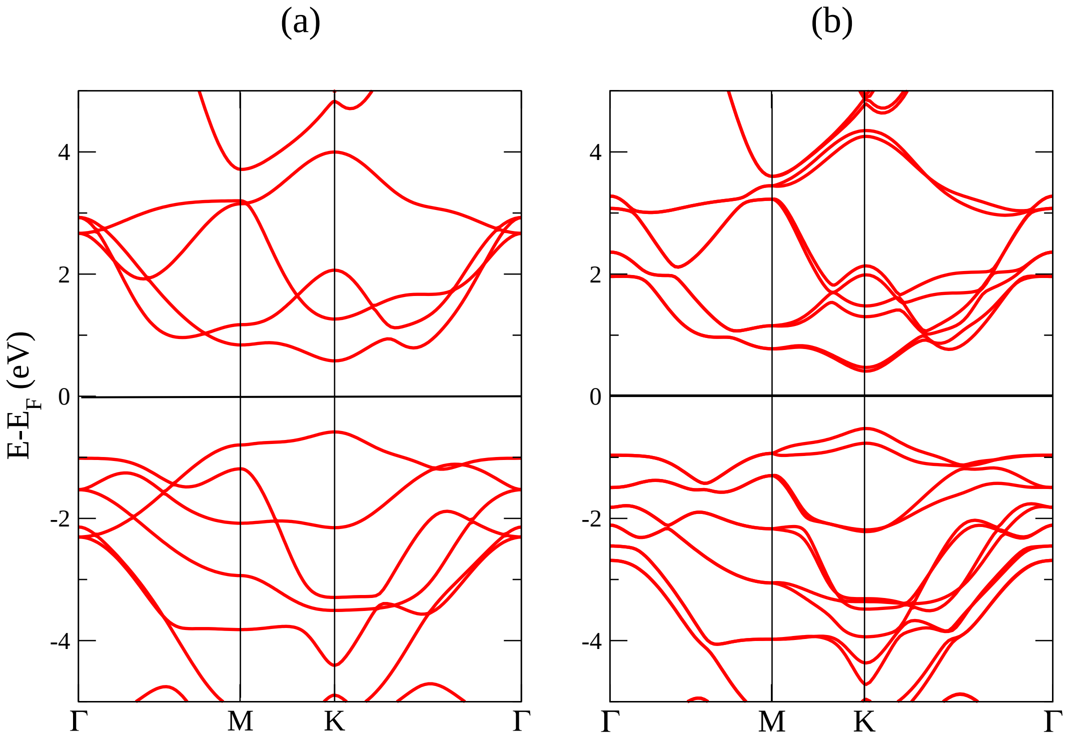

Figure 4.10: Electronic band structure for $MoTe_2$ for the cases (a) without and (b) with spin orbit coupling.

In particular, in Fig. 4.11 (which shows a zoomed in region around K) we can observe a feature that was discussed in section 1.3; there are no crossings for the SOC split conduction bands in the case of $MoTe_2$. This result shows that both split bands have similar reciprocal masses, something diferent from other TDMC's which exhibit such a crossing between bands as it was shown in Fig. 2.16. The reason for that is because the Tellurium atom is heavier than the atoms involved in the

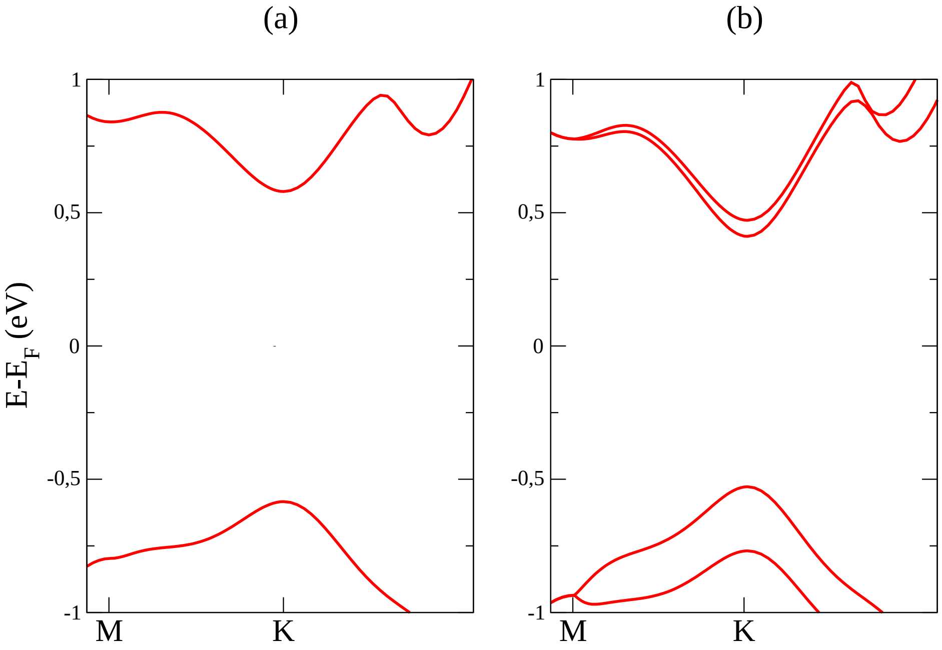

Figure 4.11: Zoomed view around the K point in $MoTe_2$ for the system (a) without and (b) with spin orbit coupling.

systems presented in chapter 2 (Se and S). This makes that the dispersion generated by the SOC inclusion have greater reciprocal mass and the spin split band crossing is avoided [95].

From the PDOS (shown in Fig. 4.12 and 4.13) we can see differences between the cases where the SOC is present or not. The differences are near the top of the valence band and also near the bottom of the conduction band where we can see a splitting. For this case, since the splitting is actually acting on a combination of linear orbitals, we just plot the total contributions from p and d orbitals shown for each of the two atoms, Mo and Te. The plot also shows that the greater contributions come from p orbitals for Te atoms and d orbitals from the Mo atoms.

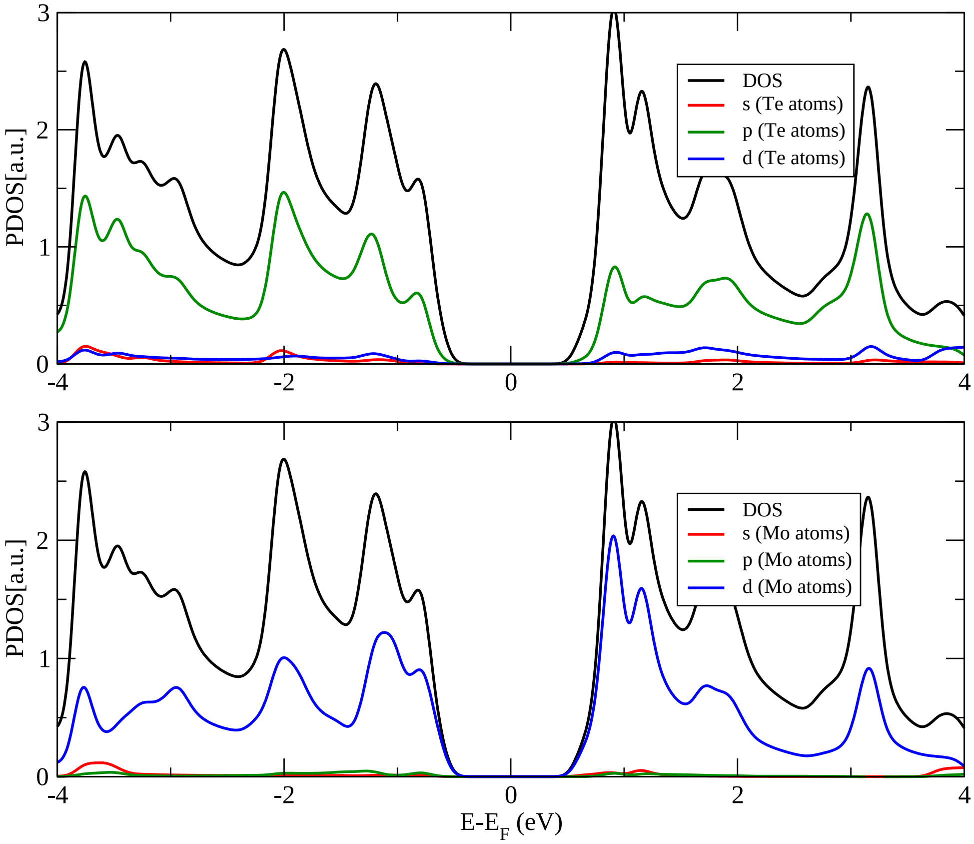

Figure 4.12: Total and projected density of states for $MoTe_2$ without spin orbit interaction.

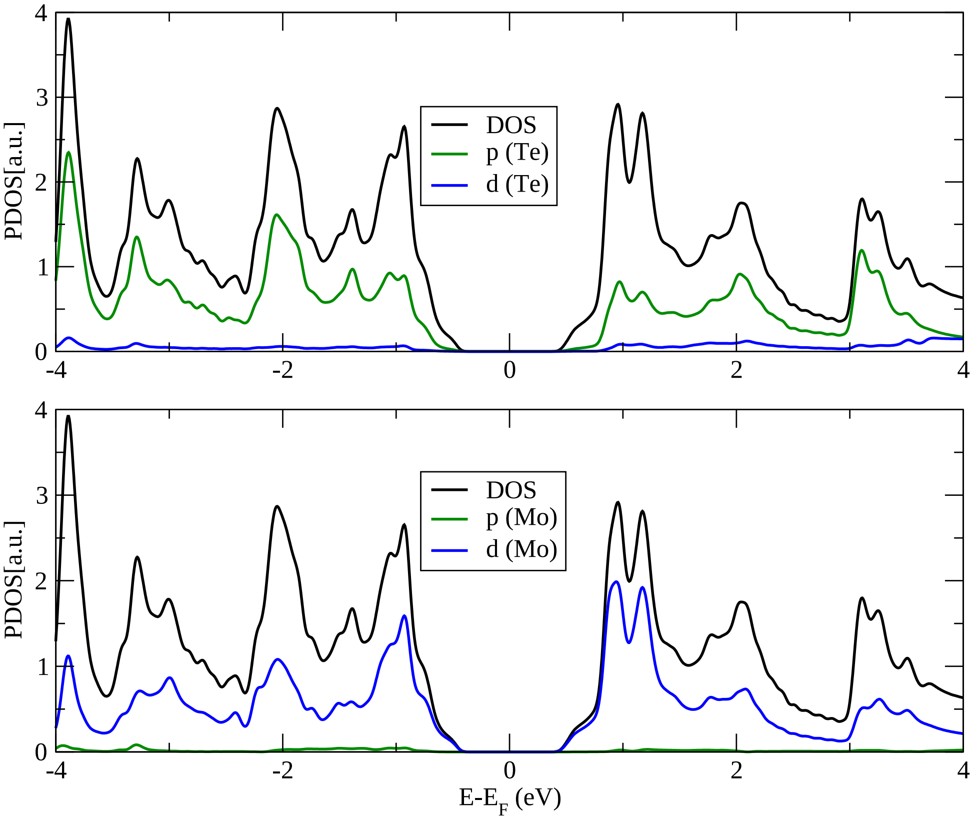

Figure 4.13: Total and projected density of states for $MoTe_2$ witt spin orbit interaction.

4.2 Heterostructure

4.2.1 Graphene & Phosphorene

Once we have the Graphene and Phosphorene results for the individual systems, we proceed to build the heterostructure made of these 2D systems we showed previously. We start by looking at the heterostructure we built with Graphene and Phosphorene. We start from the suggestion made in the work developed by Padilha et al. [65], where the unit cell is composed by two rectangular super-cells, a 1 × 4 Graphene cell with a 1 × 3 Phosphorene cell, as us shown in Fig. 4.14.

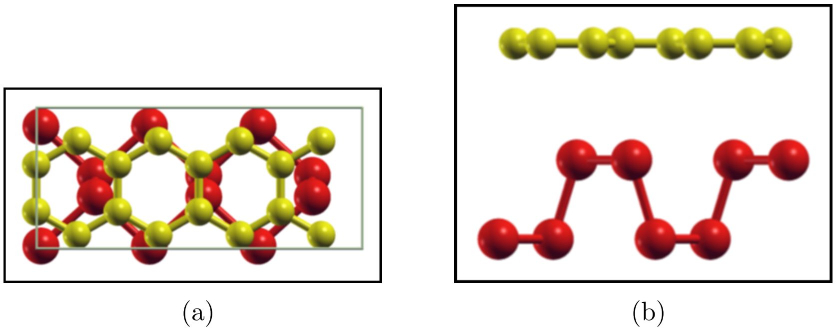

Figure 4.14: Ball-and-stick representation for the heterostructure made of Graphene and Phosphorene monolayers. a) and b) side views Color code: Carbon yellow and Phosphorus red.

In the top view we can see how the Graphene layer is above the Phosphorene layer. The distance we used for the calculations was obtained after a relaxation process where at first the Phosphorene was relaxed until the forces were smaller than 0.001 eV/$\AA$, using the proposed cell. Here, the relaxation was performed using a van der Waals corrected potential. A plot of energy as a function of layer distance is shown in Fig. 4.15. After that, we set the Graphene layer on top of the Phosphorene and the system was relaxed keeping the Phosphorene fixed until again we reached the previous value in force for each of the atoms. The distance we used for this step was taken from the cited reference, which was 3.45 $\AA$.

Once we had the system relaxed at this first distance, we looked for the best distance searching the minimum value in energy as a function of height. The value we found was 3.33 $\AA$as can be seen in Fig. 4.15.

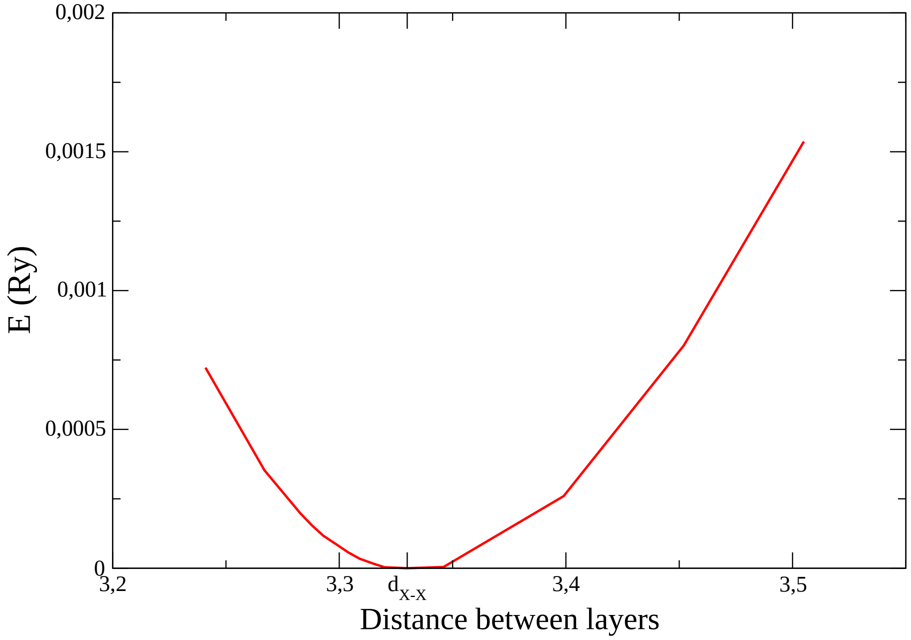

Figure 4.15: Energy vs. Distance between Graphene and Phosphorene monolayers.

For the electronic band structure we set a k-point grid of $8 \times 8 \times 1$, and the energyshift used was 0.001 eV. These parameters are similar to the previous ones used in the phosphorene monolayer case. The results with the inclusion of the spin-orbit coupling were omitted for the cases of the band structure and Projected Density of states since at large energy scales there were no modifications.

Our calculation (Fig. 4.16) shows that the system keeps the p-type nature from the phosphorene monolayer (the Fermi level is closer to the valence band branch),

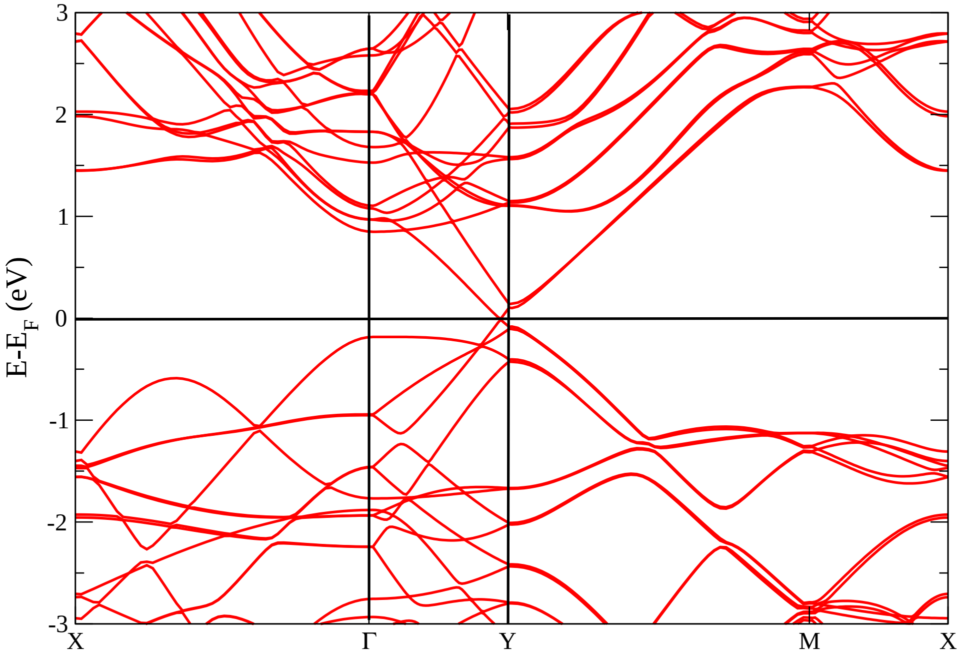

Figure 4.16: Electronic band structure for the bilayer composed by Graphene and Phosphorene monolayers.

having the Dirac cone next to the valence band but we also notice that it's located at no high symmetry point but very close to the Y point. The bottom and top of the conduction and valence bands respectively, remain at the same high symmetry point that was located in the case of the phosphorene monolayer, which was the Γ point. This is due to the folding of the supercell together with the fact that the small lattice mismatch between the two structures requires a 0.35% strain along the y direction for the graphene system.

The PDOS is shown in Fig. 4.17 where the states coming from the valence band

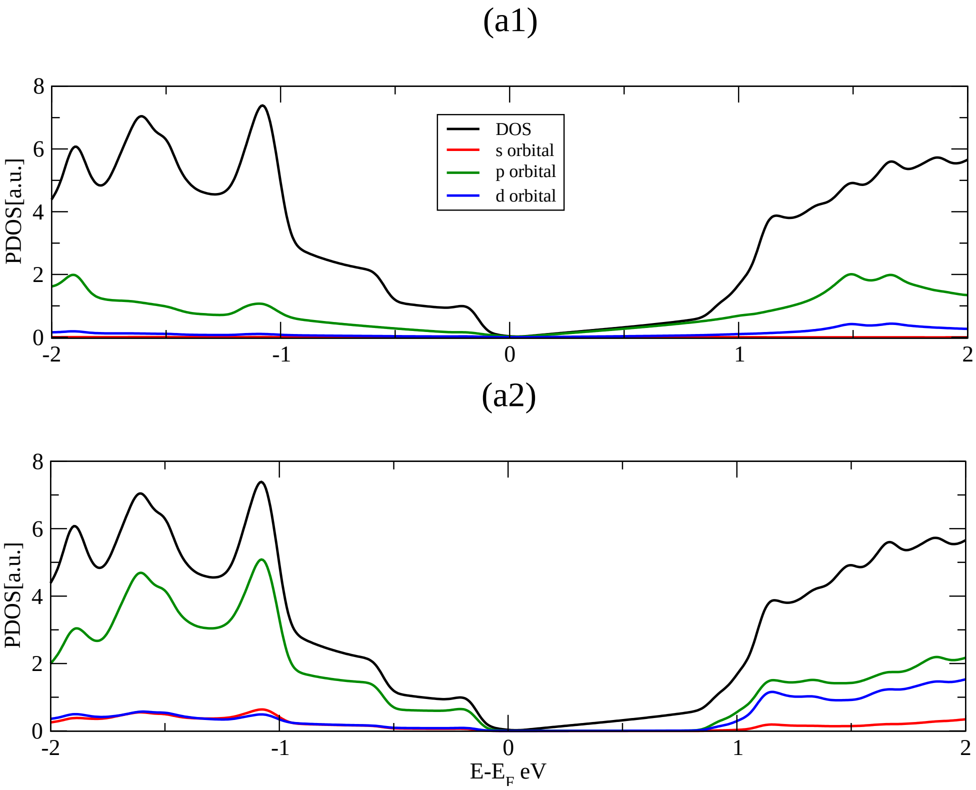

Figure 4.17: Total and Projected Density of states for the bilayer composed by Graphene and Phosphorene monolayers, (a1) is corresponding for graphene while (a2) corresponds to phosphorene.

are closer the the Fermi energy, this is something that can be visualized better in Fig. 4.18. The plot shows the projection of each orbital coming from C and P atoms. While for the case of P atoms, the contribution on each band is just the same Phosphorus p orbitals. In the case of the p_z projection for the Carbon atoms, we can see contributions coming from the Phosphorus p_z orbital.

From the projections visualized in Fig. 4.18, as we have mentioned before, there are contributions coming from phosphorene near the Dirac cone, this results in the split-

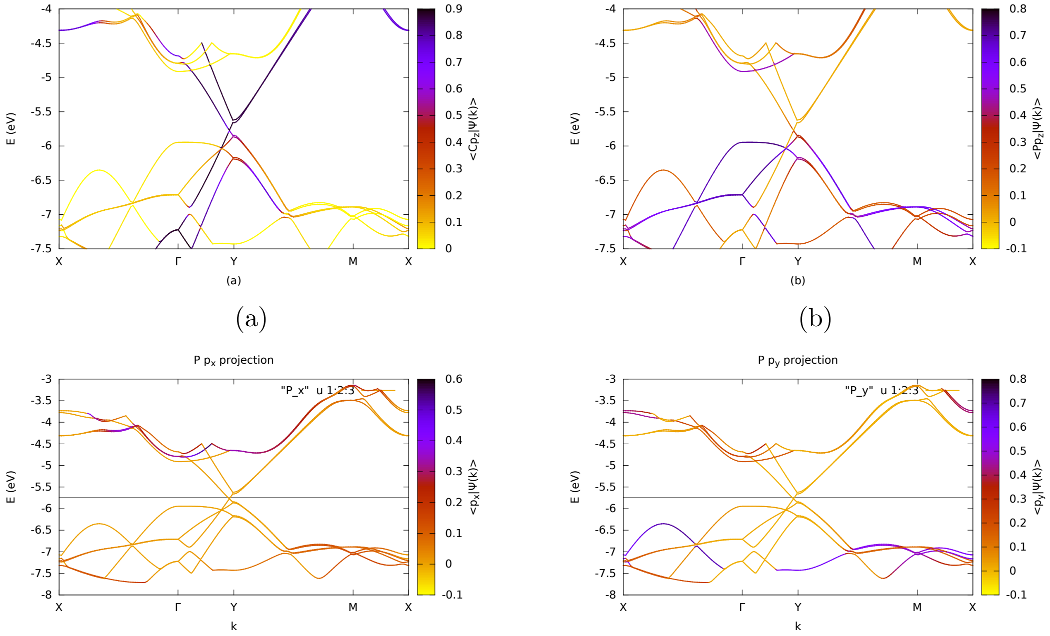

(a) (b)

(c) (d)

Figure 4.18: Orbital projection onto the Band structure for (a) C p_z, (b) P p_z, (c) P p_x and (d) P p_z orbitals.

ting observed in Fig. 4.18 where the larger splitting is coming from the phosphorene p_z split bands, while the part which remains degenerate is coming from graphene p_z orbitals, the reason for such a difference is related to the spin orbit interaction which is stronger in phosphorene rather than in graphene.

The system remains gapless at first sight, even when SOC is activated, however, there is a small gap coming from the staggered potential, because in this case we have no longer the hexagonal Brillouin zone (as shown in Fig. 4.19), and this is related with a sort of broken translation symmetry.

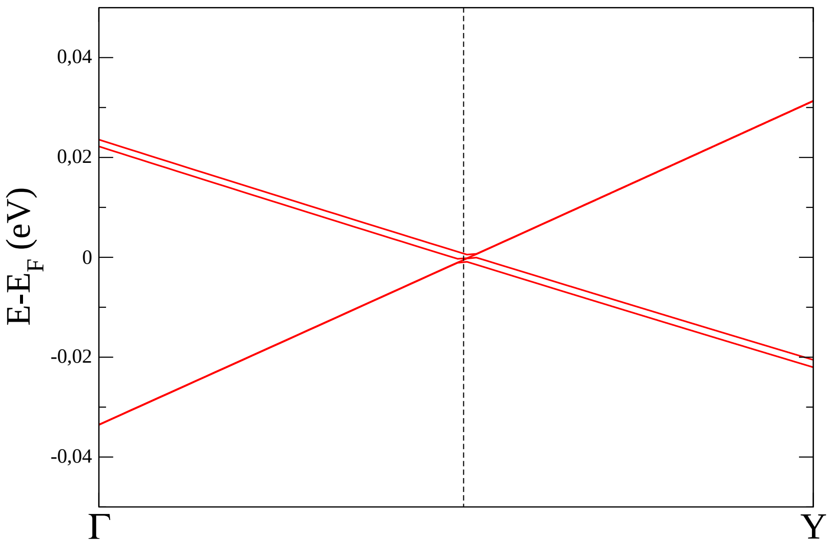

Figure 4.19: Zoomed view around the Dirac Cone in band structure when SOC is taken into account, note that in this case the Dirac cone is not located at any hight symmetry point, the Γ and Y points are not really at the positions, they are just there to visualize that the crossing point does not lie at any symmetry point.

4.2.2 Graphene & $MoTe_2$

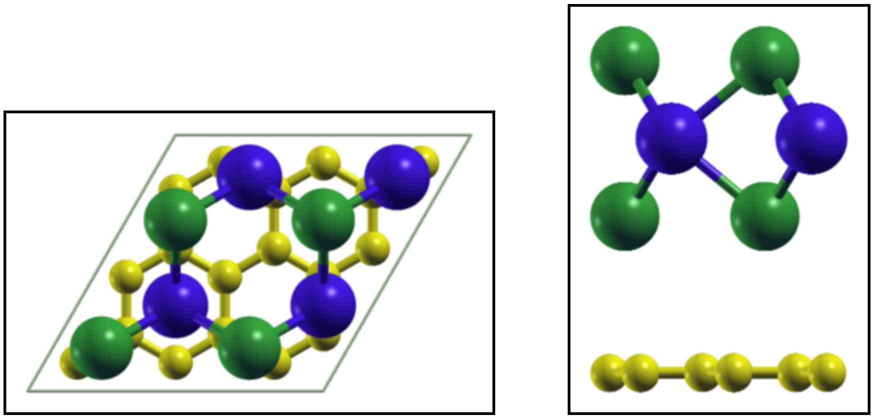
(a) (b)

Figure 4.20: (a) Top and (b) side view for heterostructure made of $MoTe_2$ and Graphene monolayers

For the case of the $MoTe_2$/graphene heterostructure we proceeded in way similar to the previous section, we color code: take a 2×2 super-cell for $MoTe_2$ and 3×3 for graphene. The $MoTe_2$ monolayer was relaxed first and after that, the Graphene monolayer was put on top of it.
The distance chosen for this case was used from reference [68] which was 3.37 $\AA$. The procedure was repeated until we reached the optimal value for the interlayer distance which in this case was found to be 3.54 $\AA$. *

Table 4.3 shows the parameters obtained from the fitting procedure (explained in Appendix C) made taking the effective $k \cdot p$ Hamiltonian which was commented on section 2.3, this is the spinless version of the Hamiltonian that can be extended to the spinful case, which will result in twice the quantity of parameters.

Different from the Phosphorene case, the Dirac cone is located at one high symmetry point which is Γ and the lowest value between bands coming from the $MoTe_2$ systems

---

*These values are quite different because the reference's system takes MoS_2 instead of $MoTe_2$.

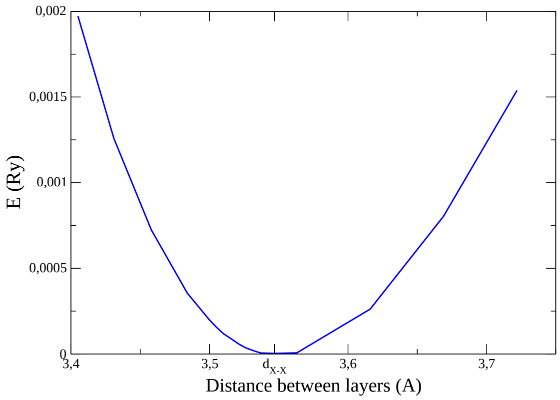

Figure 4.21: Energy vs. Distance between graphene and MoTe$_2$ monolayers.

	Values Calculated
α [eV.$\mathring{A}^2$]	-5.36
β [eV.$\mathring{A}^2$]	-2.12
$\lvert\gamma\rvert$ [eV.$\mathring{A}^2$]	3.65
κ [eV.$\mathring{A}^2$]	-10.75
η [eV.$\mathring{A}^3$]	110

Table 4.3: Low energy $k \cdot p$ Hamiltonian parameters for the Heterostructure made by MoTe$_2$ and graphene monolayers

appears at the same K symmetry point that was found for the monolayer case.
As in the previous case, we used a k-point grid of $8 \times 8 \times 1$. We start by looking at the case without SOC. In Fig. 4.22 we present the overlayed band structure of the heterostructure and of the two isolated 2D layers.

Figure 4.23 shows the projection of the orbitals coming from the three atoms present in the bilayer,there were selected only the projections which show the major contribution near the Fermi level (valence and conduction bands). For this case, since the

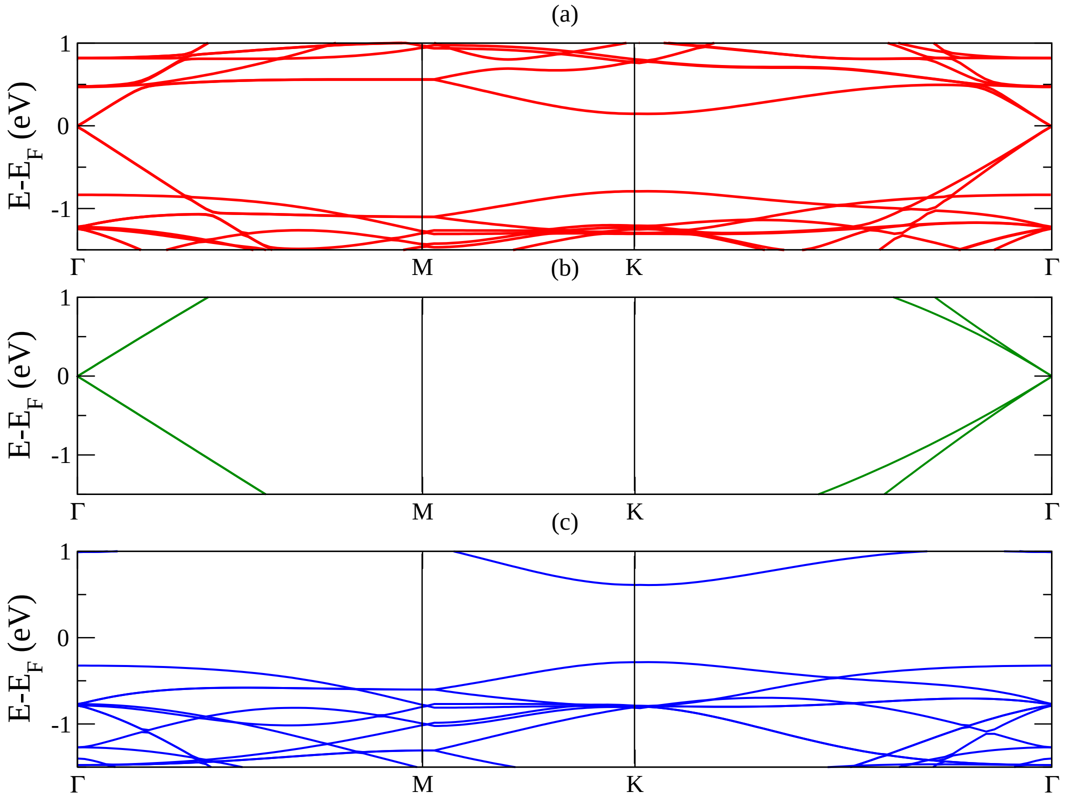

Figure 4.22: Electronic band structure for (a) bilayer made of $MoTe_2$ and graphene, (b) graphene and (c) $MoTe_2$.

translation symmetry is kind of broken, the staggered potential opens a gap for the Dirac point, however the SOC does not give larger corrections.

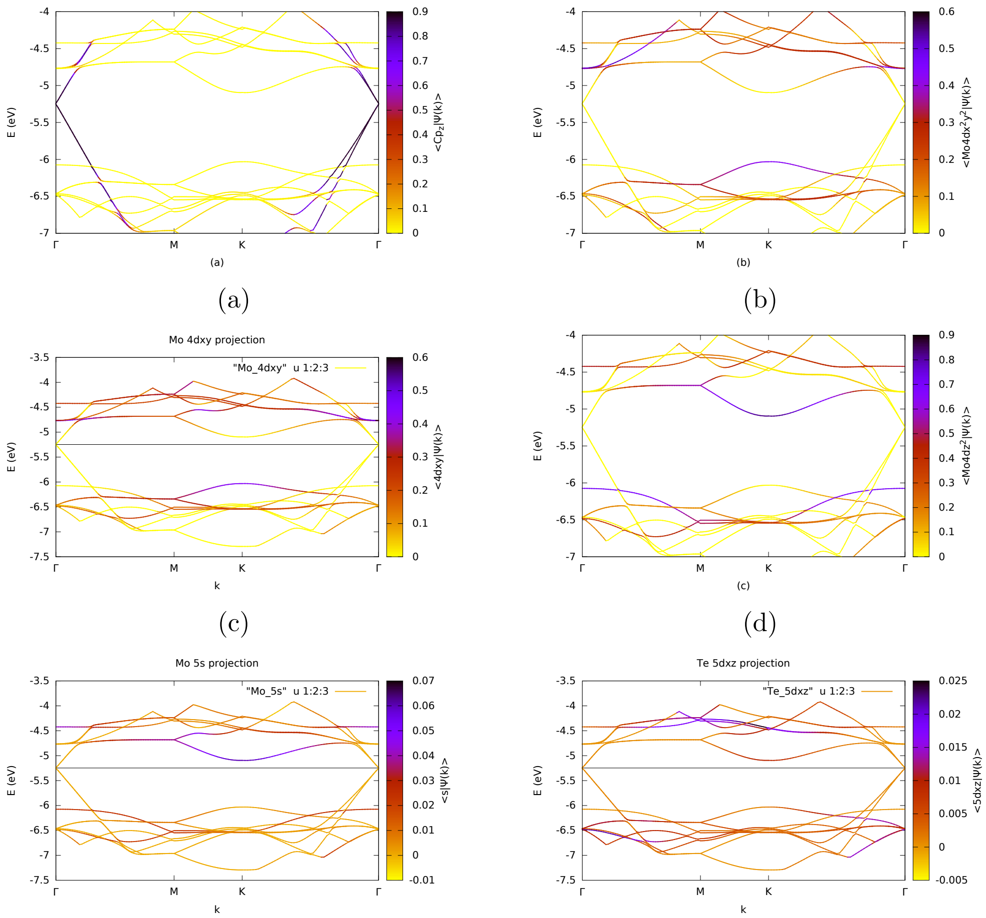

(a) (b)

(c) (d)

(e) (f)

Figure 4.23: Orbital projection onto the Band Structure for (a) C $2p_z$, (b) Mo $4dx^2 - y^2$, (c) Mo $4dxy$, (d) Mo $4dz^2$, (e) Mo $5s$ and (f) Te $5dxz$

The band structure we found for this case show the same pattern that in the case of isolated $MoTe_2$ and graphene. The Bands also show the n-type behaviour of the system, which is the same behaviour of the $MoTe_2$ monolayer, meaning that the Fermi level lies closer to the conduction band.

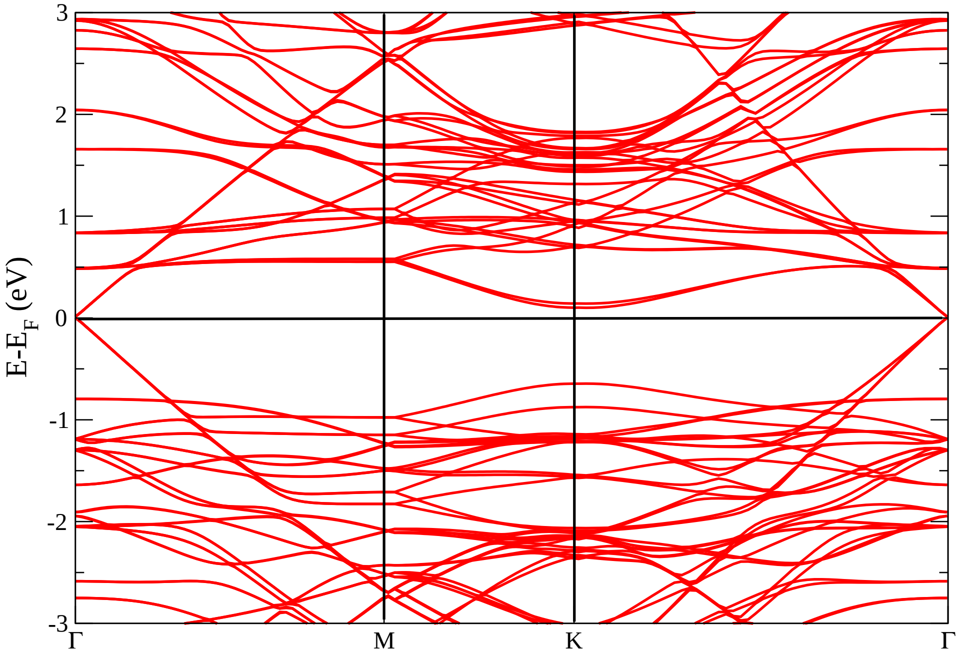

Figure 4.24: Electronic band structure for bilayer made of $MoTe_2$ and graphene whit spin orbit interaction.

Fig. 4.24 and 4.25 show the electronic band structure in the whole Brillouin zone and a zoomed region around the Γ point respectively. The inclusion of SOC interaction leads to a splitting of the bands attributed to $MoTe_2$. As Fig. 4.25 suggests, there is a sort of proximity effect related with the inclusion of the spin orbit coupling for graphene. At the Γ point there is an opened gap, which results in the loss of

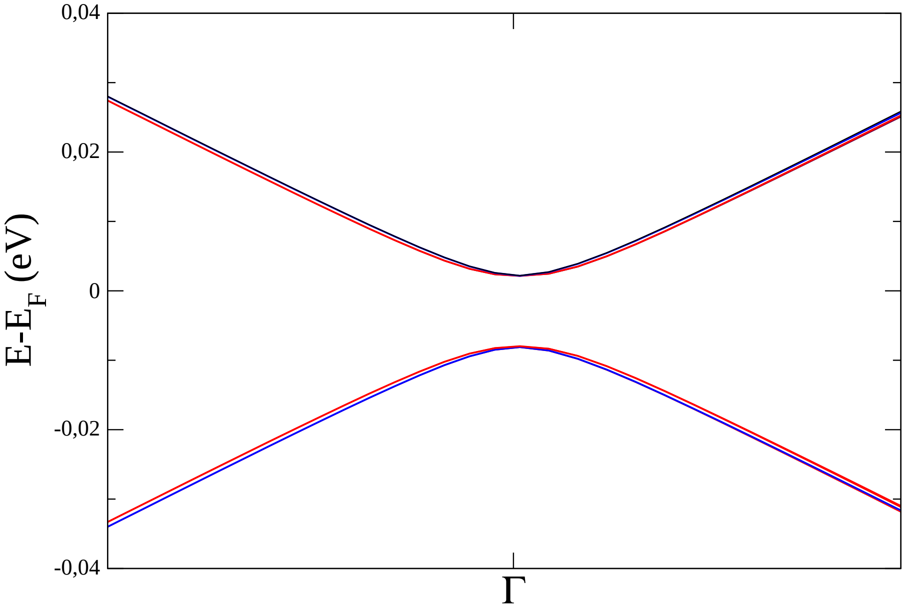

Figure 4.25: Zoomed region around the Γ point, the gap opened suggests an effect related with the inclusion of spin orbit coupling coming from $MoTe_2$.

linearity in dispersion to become quadratic. It also can be viewed that degeneracy has been partially shifted.

The results we obtained for the PDOS are in Fig. 4.26, they show the changes in the density of states for Mo and Te atoms. We plotted here the orbital contribution per chemical species. Thus it is easier to look for the differences between the case when there is no SOC and when there is.

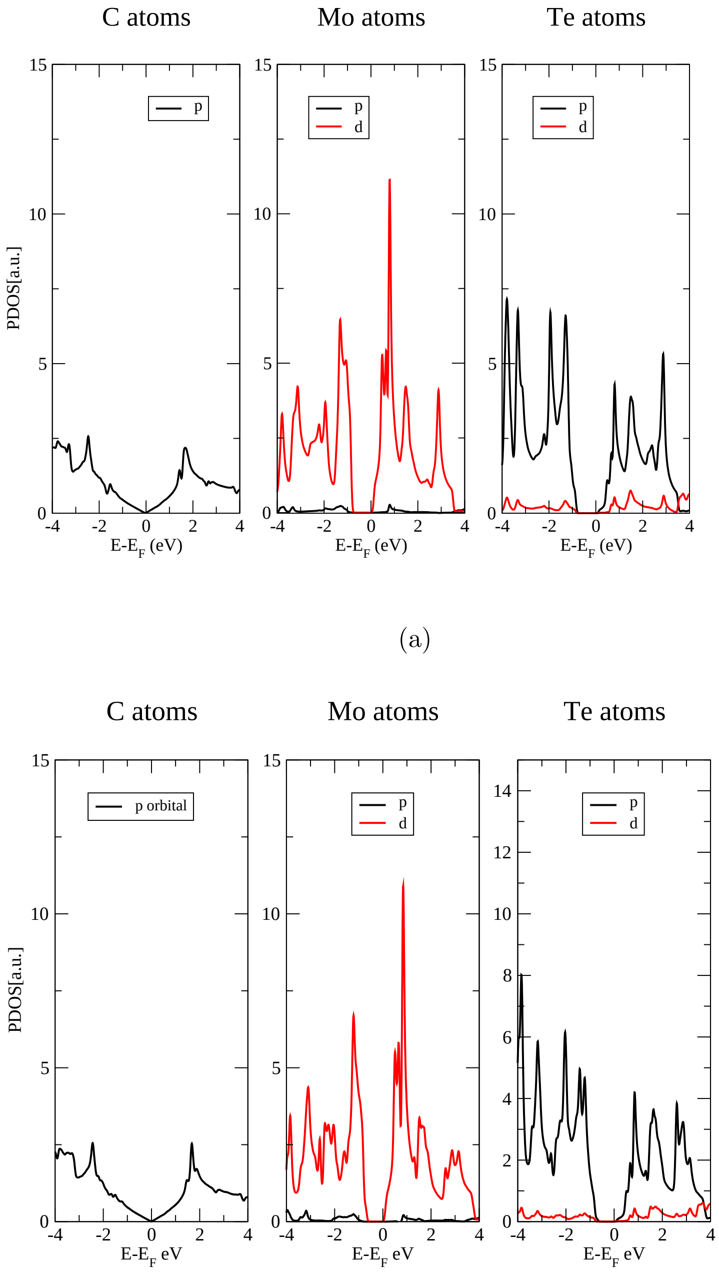

(a)

(b)

Figure 4.26: PDOS for the $MoTe_2$-Graphene bilayer (a) without and (b) with spin orbit interaction.

4.3 Isolated Defects in Graphene

As mentioned in section 2.1.1 the defects with the lowest formation energies are [40]

Defect	E_f [eV]
SW	4.87
Vacancy	7.62
2v-555-777	6.63
2v-585	7.48

Table 4.4: Formation energy for graphene taken from reference [40].

Here, we have considered them in our calculations, first as isolated defects. Their structures are shown in Fig. 4.27.

Every defect presented above was relaxed until the forces on each Carbon atom was less than 0.01 eV/ $\mathring{A}$. We use a k-point grid of $8 \times 8 \times 1$ for this procedure.

In Fig. 4.27 we notice how the distances between the Carbon atoms are larger than in the pristine graphene, this will have implications in our results as we go through the projected density of states.

From Fig. 4.28 we can observe that the total contributions near the Fermi level for the atoms forming the defect are coming from the p_z carbon orbitals. In this case the Dirac cone is precisely at the Fermi level. This happens because the Stone-Wales defect just consists in a reordering of the carbon atoms, meaning that the state describing this configuration has an energy higher than pristine graphene, anyhow its energy is lower compared to the other defects mentioned before.

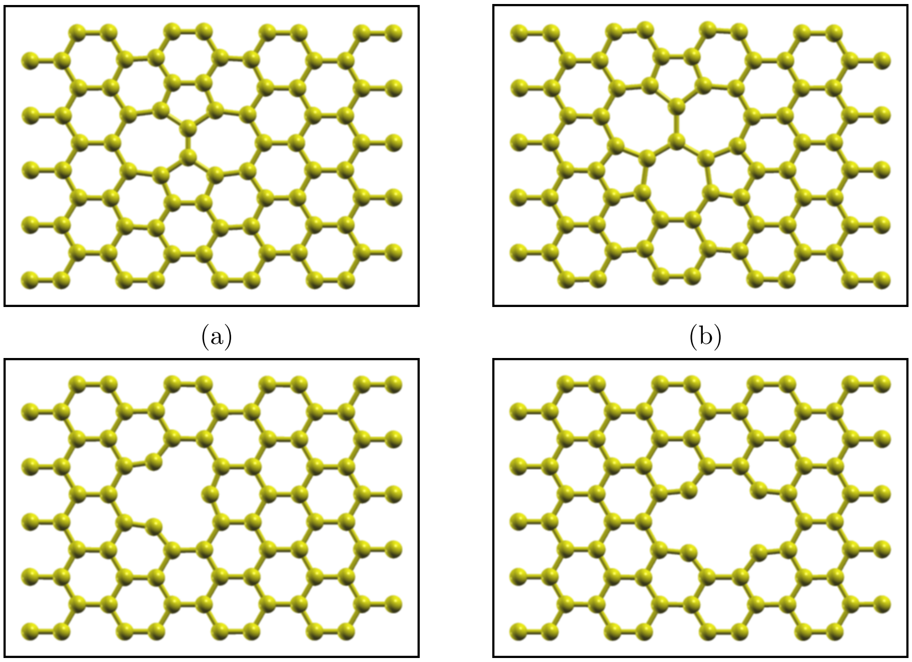

(a)

(b)

(c)

(d)

Figure 4.27: Top view of graphene most likely defects. (a) SW, (b) 2v-555777, (c) single vacancy and (d) 2v-585.

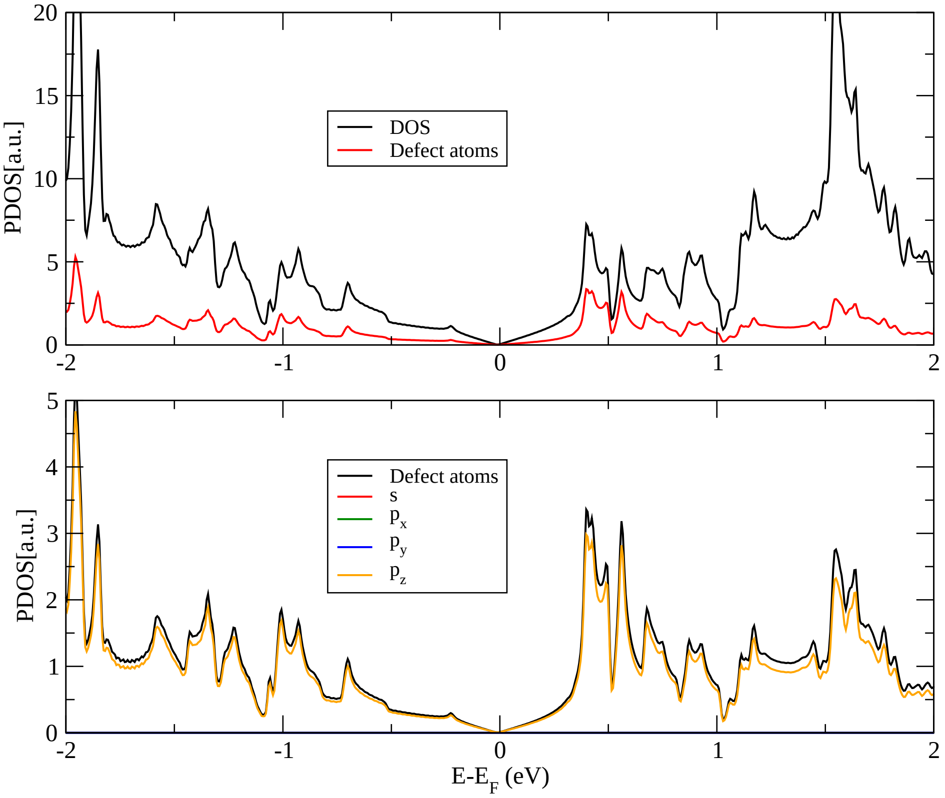

Figure 4.28: Total and Projected density of states for Stone-Wales defect.

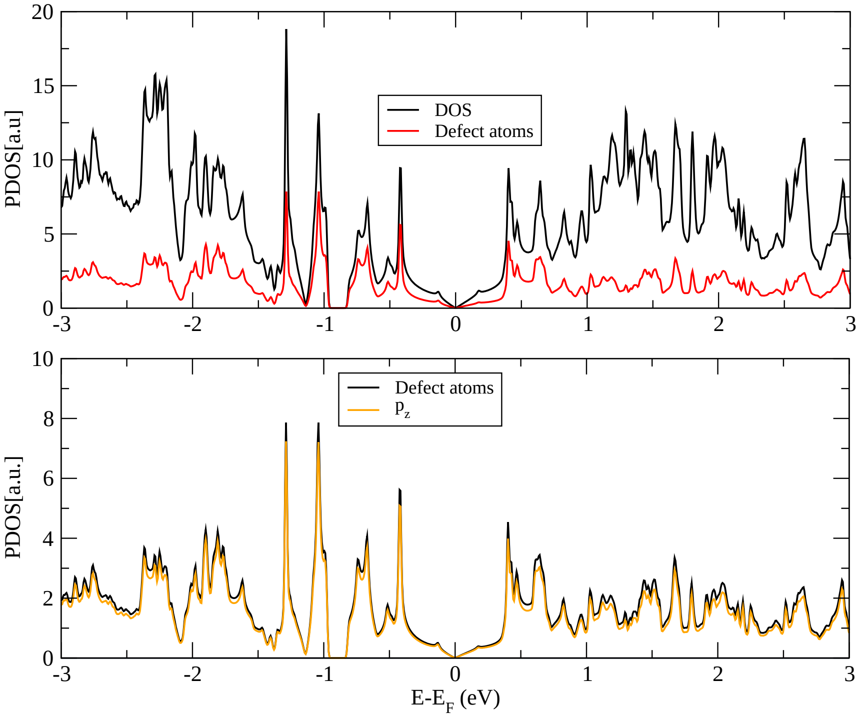

Figure 4.29: Total and Projected density of states for 2v-555-777 graphene defect.

Similar to the case of the Stone-Wales, the projected density of states for the 2v-555777 defect is shown in Fig. 4.29, there we can see that the total contribution, coming from atoms forming the defects, belongs to the p_z carbon orbitals. However, in this case the Fermi level no longer lies near the Dirac cone because we have two carbon atoms less, resulting in the variation of the Fermi level, which in this case lies below the Dirac cone. For the 585 defect in Fig. 4.30, s, p_x and p_y orbitals are present in the zero energy modes, however the splitting of the p orbitals in the former is negligible, different from the case we will see in the vacancy defect. In this case as in the 555-777 defect, the Fermi level lies below the Dirac cone. For the the single vacancy (Fig. 4.31) we can see that even in this case the distance between carbon atoms still bigger than in pristine graphene, the results show a difference as a product of the inclusion of the SOC, this is something remarkable because in

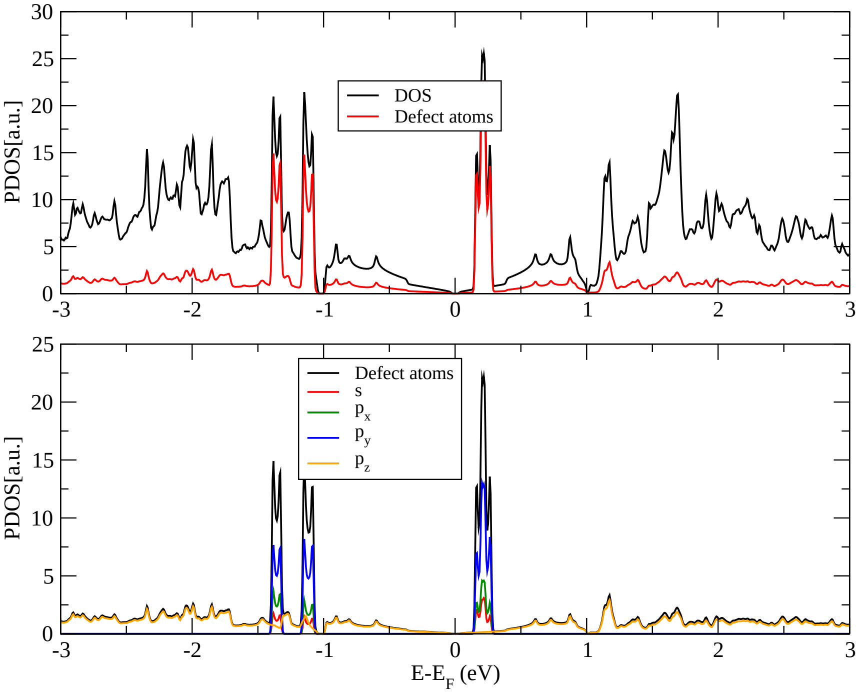

Figure 4.30: Total and Projected density of states for 2v-585 graphene defect.

all the previous cases we have a translation symmetry breaking as in this one, but there were negligible changes. The split is present even in the zero energy modes which are well located in the Fermi level as can be seen in the bands (Fig. 4.31.a), the existence of the pseudo gap is related to the interaction of the defect with its mirror images.

Our results show that except for the case when there is just one vacancy, the effects produced by the inclusion of SOC are negligible. In the case of the vacancy besides the existence of localised states which can be observed in the projected density of states, this means that the existence of the vacancy enhances the effects related to the SOC.

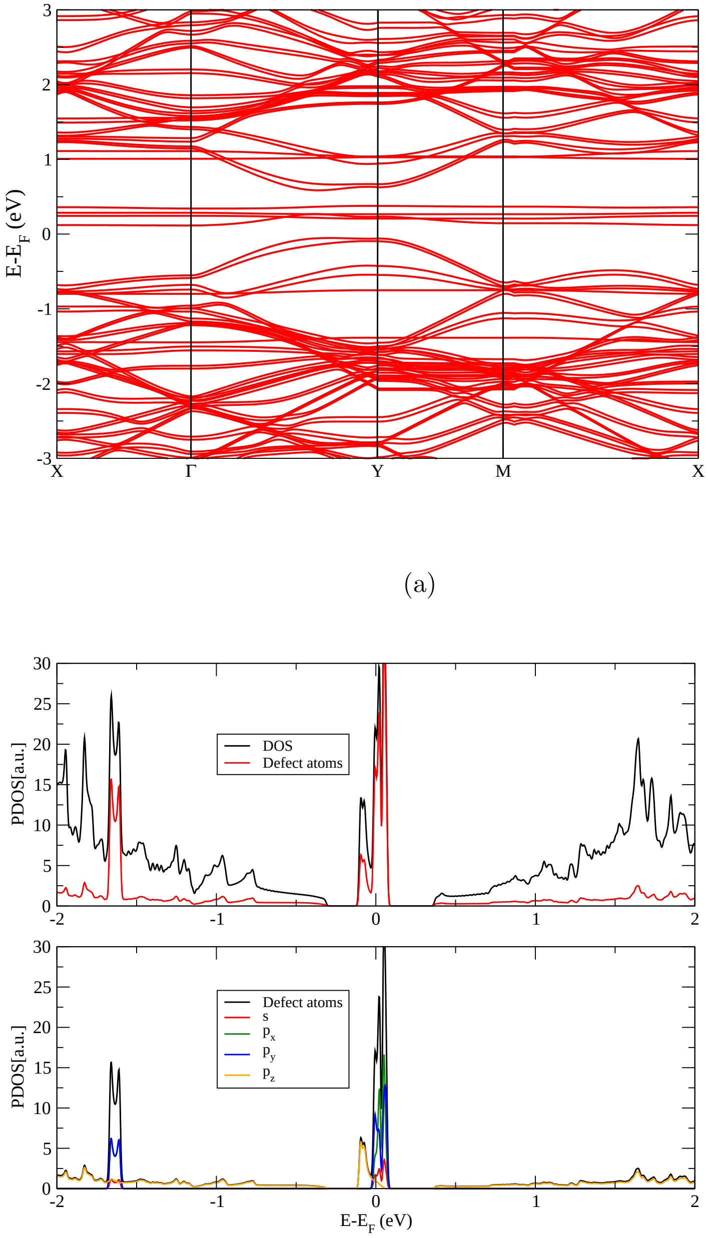

(a)

(b)

Figure 4.31: Single vacancy (a) electronic band structure and (b) projected density of states with spin orbit coupling interaction.

4.4 Phosphorene & Graphene Defects

Following the same ordering found in the previous section, we list the formation energy for each of the bilayers carrying the defects.

Defect	E_f [eV]
SW	0.954
Vacancy	6.018
2v-555-777	10.505
2v-585	8.794

Table 4.5: Formation energy for the system built from Phosphorene and Defects

In table 4.5 we show a list for the formation energies in these systems. The formation energies obtained are quite different from the values listed in reference [41] where the systems consisted only in the defective monolayers. This is something that was expected for many reasons, the first one is the presence of phosphorene and its well known instability. Another reason is because our graphene sheet is stretched and this structural changes leads to electronic changes.

Those values show that is easier obtain an SW like defect for the Heterostructure, this is the same the previous reference has found, however, the system carrying the 2v-555777 defect has the greatest value among all of them, which is in contradiction with the former energy ordering shown in the reference.

The systems shown in Fig. 4.32 are bilayers made of a Phosphorene monolayer above one sheet of graphene monolayer where is present a defect. The distance between those monolayers was taken to be the same in the case of the pristine systems, this was made to simplify the computational effort.

For the relaxation process we proceed as in the previous cases, phosphorene was

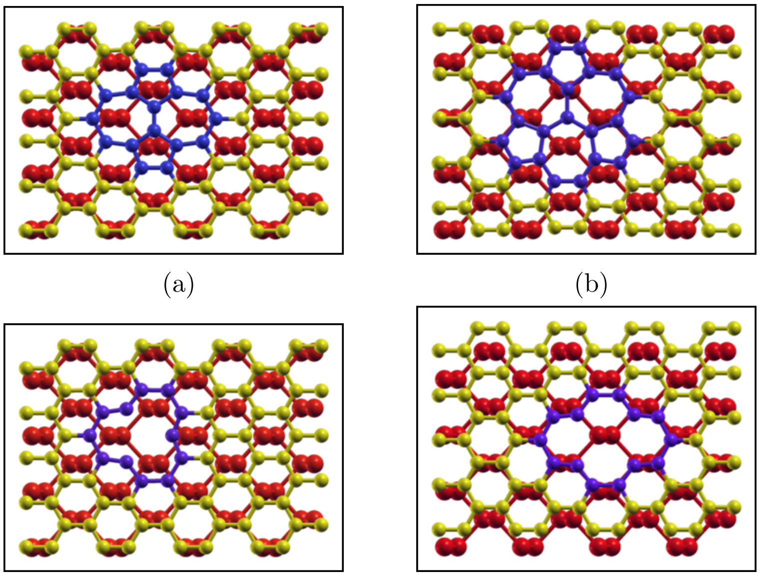
(a)
(b)
(c)
(d)

Figure 4.32: Top view for bilayers made from phosphorene and gaphene most likely defects. Phosphorene monolayer is below (a) Stone Wales, (b) 2v-555777, (c) single vancacy and (d) 2v-585 defects.

kept fixed as well as the border carbon atoms in graphene sheet. Every system was relaxed until the forces on each atom were less than 0.01 eV/ $\AA$. We use a k-point grid of $8 \times 8 \times 1$.

Fig. 4.33 shows the Projected density of states for the system carrying the Stone-Wales defect. As a result of the interaction with the graphene sheet, the phosphorene valence band is closer to the Fermi level, which was set to zero. On the other hand, the projected states for the defective graphene have the same profile that was shown in Fig. 4.28.

In Fig. 4.34 the plot shows the projected density of states for the case where the defect is 2v-555777, the density states for the carbon atoms show the location of the Dirac cone, however the Fermi level is located below since for this case there are two carbon atom missed. For phosphorene we can see that the top of its valence band

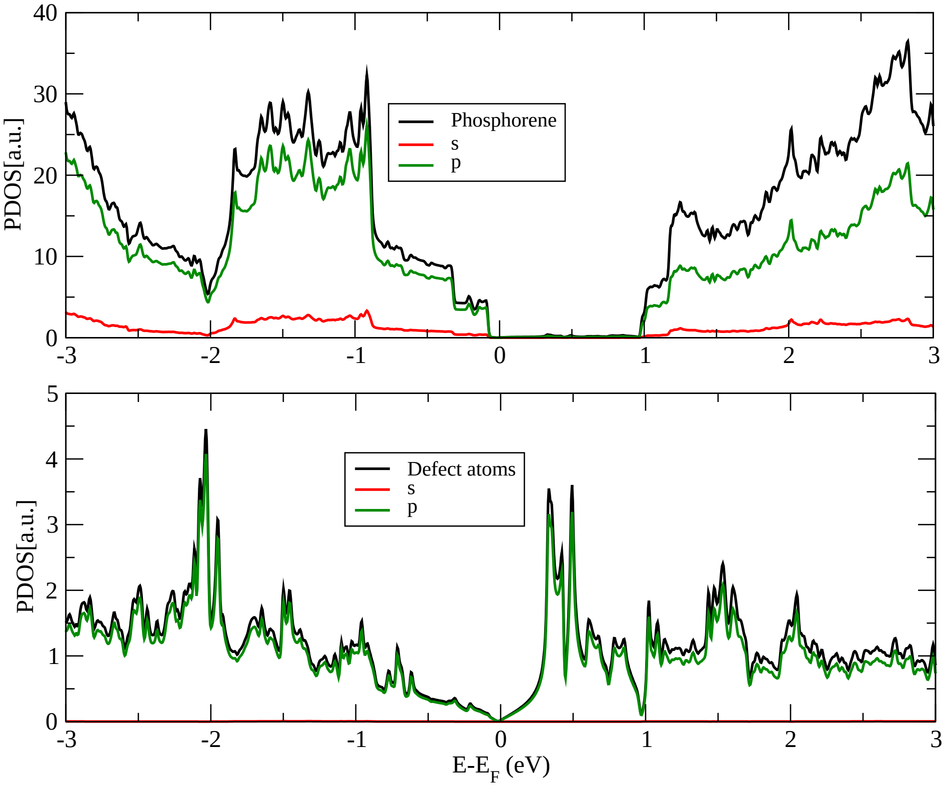

Figure 4.33: Projected density of states for phosphorene and Stone-Wales defect, color code: total PDOS (black), *s* orbital (red) and *p* orbitals (green).

is far from the Dirac cone, but is closer to the Fermi level set below the the zero point. The inclusion of spin orbit coupling interaction leads no modification in the electronic structure.

For the case of mono-vacancy in Graphene (Fig. 4.35), the interaction with mirror defects is a little more reduced, since the defect is smaller in the unit cell. The system presents a pseudo gap as the result of the interaction with its mirror images and also the effect of the SOC is larger than in the other cases, this was also obtained for the Defective Monolayer.

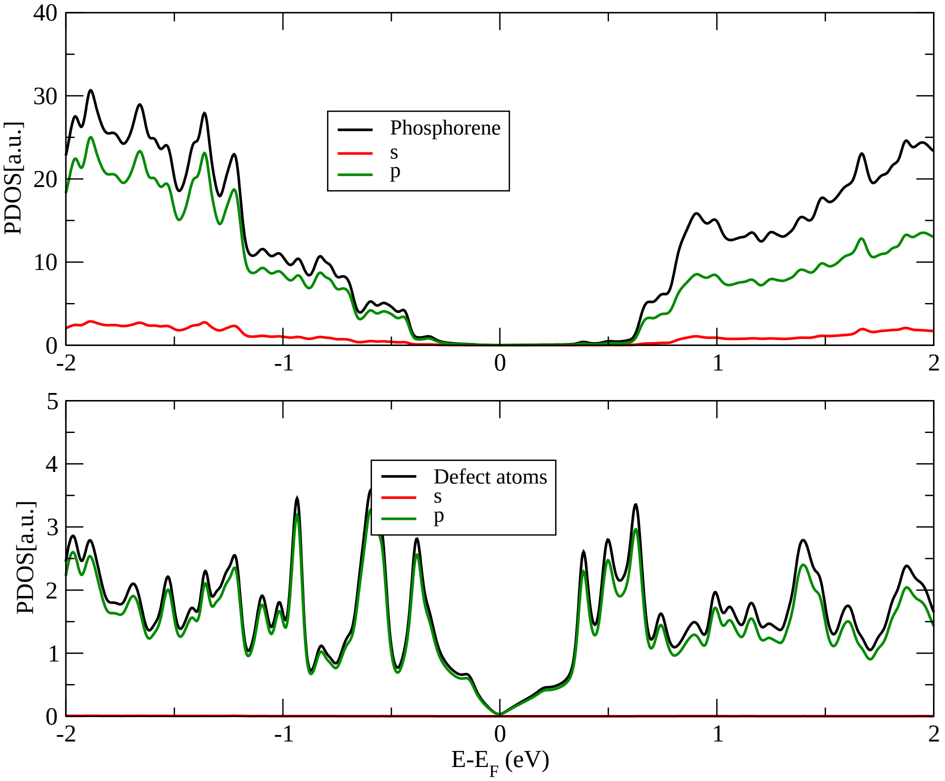

Figure 4.34: Projected density of states for phosphorene and 2v-555777 defect, color code: total PDOS (black), *s* orbital (red) and *p* orbitals (green).

From the PDOS it can be viewed that there are slight modifications in the contributions coming from phosphorus atoms, then the effects related to SOC originated from the defective system induce modifications in the electronic structure of Phosphorene. Figure 4.36 shows the bilayer composed of one sheet of Phosphorene and one Defective Graphene monolayer containing a 2v-585 defect. Different from the case of the other di-vacancy, here there is a shift of the phosphorene valence band, which is located near the resonances in the graphene projected density of states. In this case the Fermi lever is located below the energy we set as zero, then the Fermi level is crossing the phosphorene valence band.

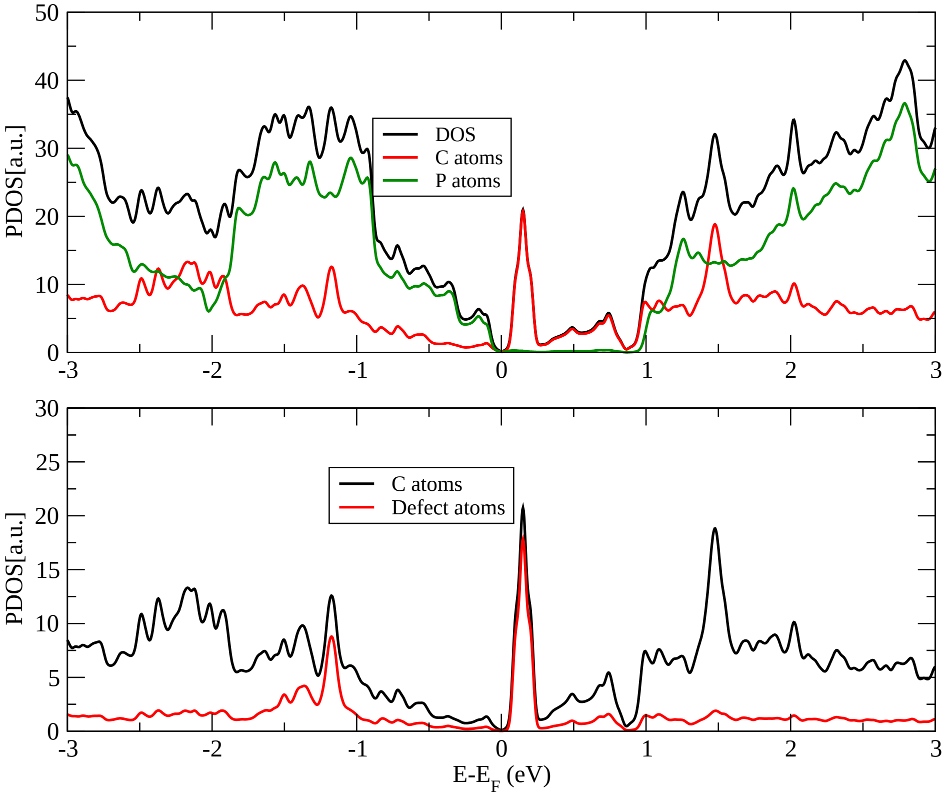

Figure 4.35: Projected density of states for phosphorene and 2v-585 defect, color code: total PDOS (black), *s* orbital (red) and *p* orbitals (green).

The PDOS showed no modifications with the inclusion of SOC in most cases, for this reason the only system plotted with the inclusion of the spin orbit coupling effect was the bilayer carrying a single vacancy.

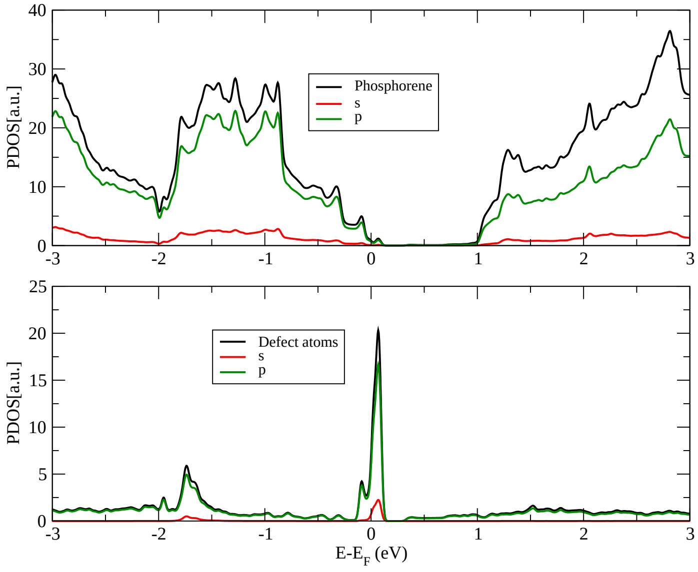

(a)

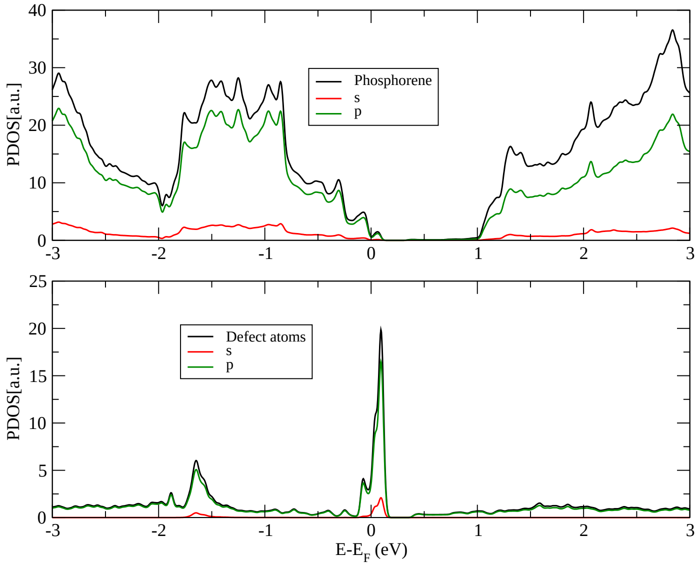

(b)

Figure 4.36: Projected Density of States for bilayer phosphorene and single vacancy (a) without and (b) with SOC with their Orbital Contributions, the color code is shown in the plot.

4.5 $MoTe_2$ & Graphene Defects

Now we move to the other four systems, which were obtained from the stacking of both layers of pristine $MoTe_2$ and the defective graphene layers. The relaxed structures are no more stretched as there were in the case of phosphorene, however the cost is that now we have more atoms in the unit cell and the computational effort increases.

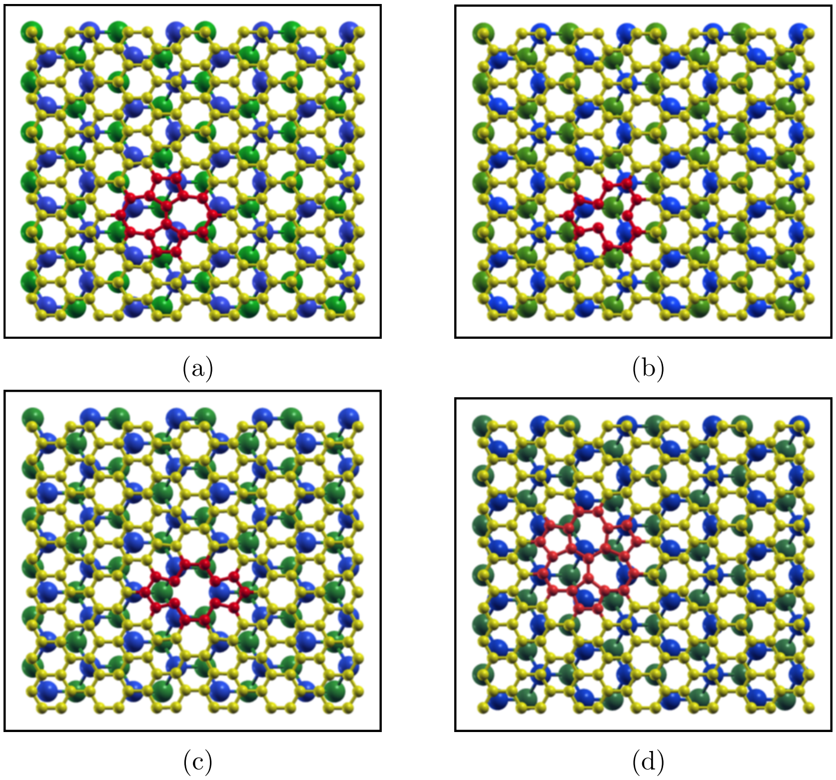
(a) (b) (c) (d)

Figure 4.37: Top view for the heterostructure made of $MoTe_2$ and (a) 2v-585, (b) 2v-555777, (c) vacancy or (d) SW.

The values listed in table 4.6, different from those obtained for the phosphorene case, show the actual energy ordering for the defects present in the system which was listed in reference [41], the lowest formation energy still is the energy coming from the Stone-Wales defect and then is the more likely defect found in this kind

Defect	E_f[eV]
SW	5.977
Vacancy	9.152
2v-555-777	8.192
2v-585	9.145

Table 4.6: Formation energy for the system built from $MoTe_2$ and Defects

of system, after that is the energy obtained for the defect 2v-555-777. The highest formation energy is for the vacancy and it's slightly different from the formation energy for the 2v-585 defect.
The same pattern obtained for the formation energy in this case says that maybe the origin of the great differences found in the phosphorene case is related to the structural modification in graphene, since the sheet is stretched and that changes the electronic configuration of the system.

The structures were relaxed until they reached a force less than 0.04 eV/ $\mathring{A}$, with the same procedure before, the $MoTe_2$ monolayer was kept fixed as well as the border of the defective graphene too. The calculation was performed using a k-point grid of $3 \times 3 \times 1$ because the size of the system and the distance between layers was taken equal to the value for the pristine systems. In this case, because the great amount of atoms, the calculation involving the SOC was not performed.

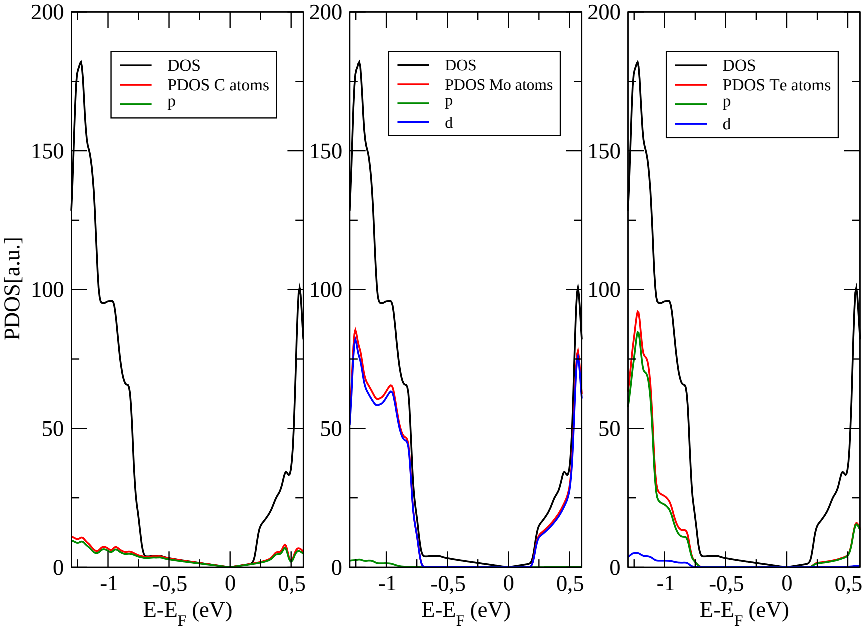

Figure 4.38: PDOS for the bilayer made of a graphene Stone-Wales defect under $MoTe_2$ Monolayer

For the case of the Stone-Wales defect, the PDOS can be observed in Fig. 4.38, and is the only system where there are no resonances in the Gap region of $MoTe_2$, however the systems keeps the n-type character of the monolayer systems, this was expected since the $MoTe_2$ also has the same character.

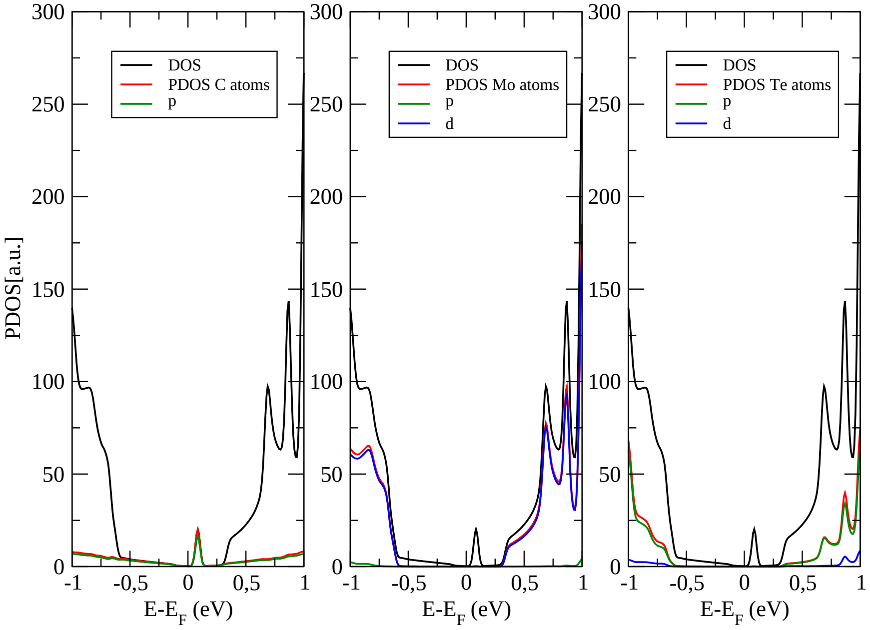

Figure 4.39: PDOS for the bilayer made of a graphene Vacancy defect under $MoTe_2$ Monolayer

Figure 4.38 shows the unit cell for graphene vacancy under the $MoTe_2$ layer. The defect seems to be less stretched than in the phosphorene case and again the distance between mirror images is large. The PDOS can be observed in figure 4.38, where the resonance is well located closed to the Fermi energy.

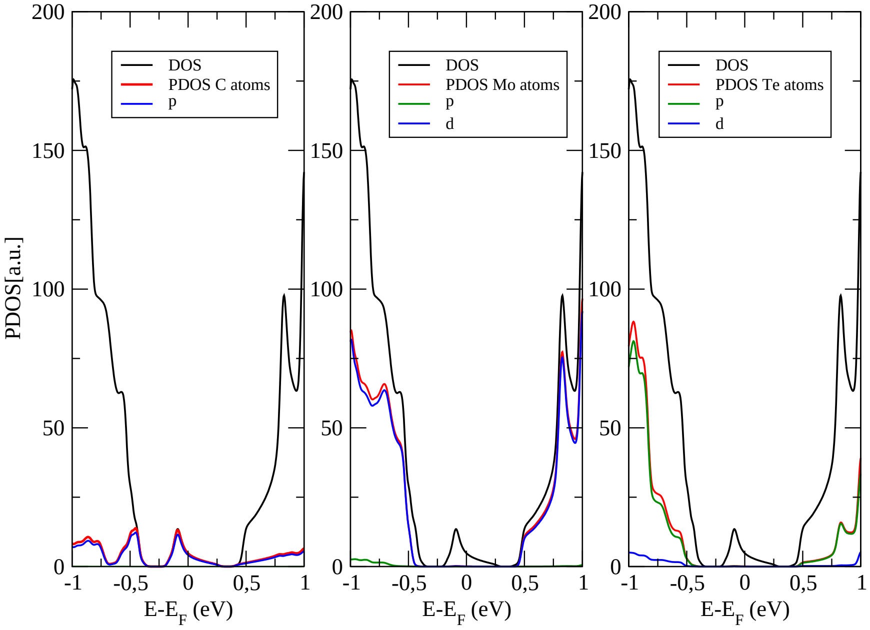

Figure 4.40: PDOS for the bilayer made of a Graphene 555-777 di-vacancy defect under $MoTe_2$ Monolayer

In this case, the defect is also located far from their mirror images, and a negligible interaction is expected. Different from the first case, the PDOS plotted in Fig. 4.40, shows that the resonance coming from the defect in the gap region is closer to the valence band. The contributions coming from Mo and Te remains the same as in the pristine case.

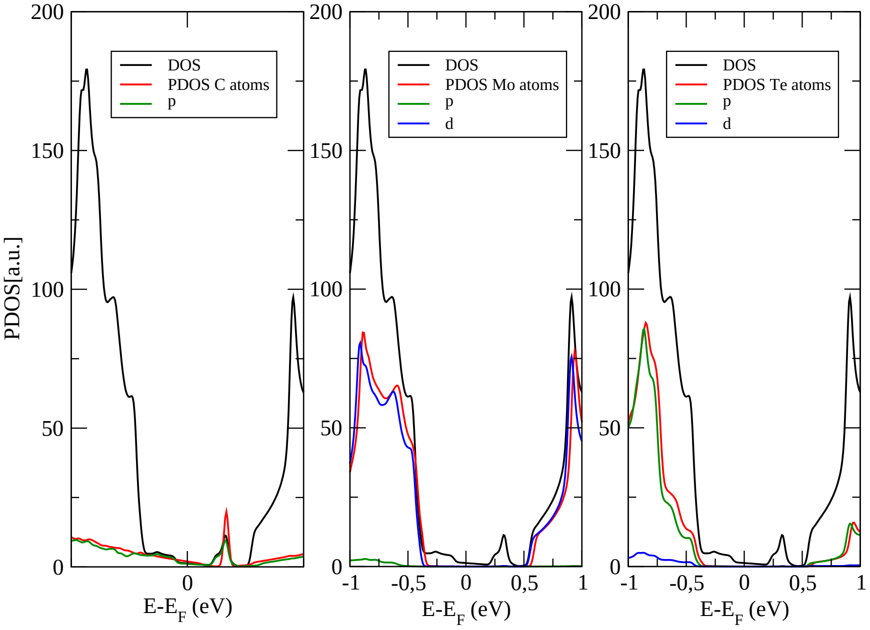

Figure 4.41: PDOS for the bilayer made of a graphene 2v-585 defect under $MoTe_2$ Monolayer

Figure 4.41 shows the unit cell for the first system composed by the divacancy 2v-585 and one sheet of $MoTe_2$. The defect is located well far from the mirror images, this reduces the interaction between them and results can be taken as more realistic since in practice this is what happens in real systems. The PDOS were only plotted about a narrow energy region because the great computational effort needed for such a calculation.
In Fig. 4.42 we can see a sort of charge transfer to the gap region of the $MoTe_2$ system. While in the case of the pristine bilayer of Graphene and $MoTe_2$, there were no observed such a contribution, here in our defective systems, there is a contribution coming from Mo and Te atoms in the regioZoom near the Fermi level for the Projected density of states for (a) SW, (b) single vacancy, (c) 2v-555777

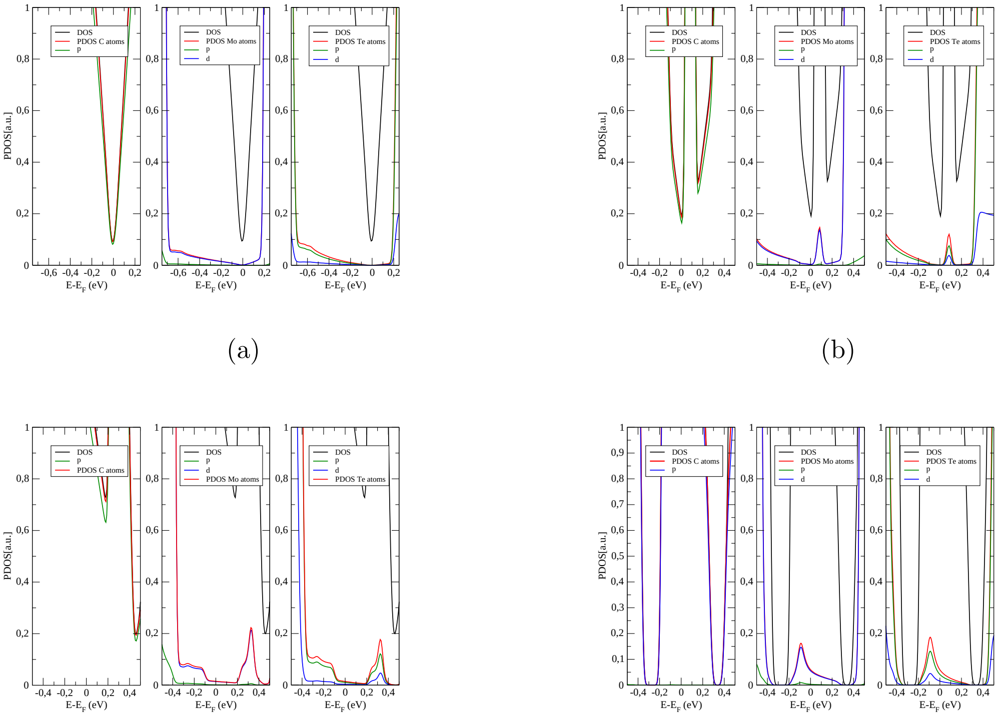

(a) (b)

(c) (d)

Figure 4.42: Zoom near the Fermi level for the Projected density of states for (a) SW, (b) single vacancy, (c) 2v-555777 and (d) 2v-585 defects.

and (d) 2v-585 defects.n where there are no states for the pristine case. The result also shows that these contributions appear in different manners depending on which defect is present in the system.

Chapter 5

Conclusions and Perspectives

In the present work we studied the electronic properties of systems based on graphene, phosphorene and $MoTe_2$. Besides that, since defects are always present in real systems, we took the most likely defects in graphene and studied the properties of such structures where the Spin Orbit Coupling was also addressed. Using Density Functional Theory (DFT) tools, we obtained the Electronic band Structure for most of the systems, and also the Projected Density of States (PDOS), in order to extract the more information about the inclusion of such parameters.

Our calculations have shown that the inclusion of SO coupling is significant only when the atoms involved are really heavy (as expected) as in the case of $MoTe_2$ or when there is a great lack of translation symmetry as in the case of a mono-vacancy in pristine graphene, where also the inversion symmetry is broken. The inclusion of SO coupling leads to small modifications in the band structure for the phosphorene system. The same was obtained in the case of the bilayer constructed from both phosphorene and graphene layers. There we noticed were no changes in the electronic properties of the system and one can consider that this heterostructure has properties which are similar to the individual isolated monolayers.

The results obtained from the defective systems have shown the existence of resonances near the Fermi level. This was something expected for the mono-vacancy case, where one carbon loses a neighbour and their orbitals are left free of binding: forming the so-called zero energy modes.

For the cases of heterostructure built on Graphene, the SO coupling led to modifications just in the case of $\mathrm{MoTe_2}$, something that can be observed in the bands and PDOS, the systems remain as an n-type character material as in the case of Phosphorene, where the system still has a p-type character. However there was no evidence of significant changes in the electronic structure once the SO coupling was taken into account for the latter. For the bilayer $\mathrm{MoTe_2}$/Graphene we obtained the $k \cdot p$ parameters related to an effective low energy Hamiltonian, as procedure that can be extended when the SO coupling is addressed.

Our results for the heterostructure built on defective graphene, have shown that the inclusion of SO coupling is only important in the case of just one vacancy, this is for the case of Defect-phosphorene. For both cases (phosphorene and $\mathrm{MoTe_2}$) it has been found contributions coming from the interaction between the defect atoms and the atoms in the pristine systems, this leading to charge transfer.

As a next step in this project the natural procedure would be to consider SOC in the $\mathrm{MoTe_2}$/defective graphene case (a system which is quite large).

Bibliography

[1] A. H. Castro Neto, F. Guinea, N. M. R. Peres, K. S. Novoselov, and A. K. Geim. "The electronic properties of graphene". Rev. Mod. Phys. **81**, 109 (2009).

[2] K. S. Novoselov, D. Jiang,F. Schedin,T. J. Booth,V. V. Khotkevich, S. V. Morozov, and A. K. Geim. "Two-dimensional atomic crystals". PNAS **102**, 30, 10451-10453 (2005).

[3] L.D. Landau. "Zur theorie der phasenumwandlungen II phys". Z. Sowjetunion **11**, 26-35 (1937).

[4] R.E. Peierls. "Bemerkungen ber umwandlungstemperaturen". Helv. Phys. **7**, 81-83 (1937).

[5] S. Murakami. "Intrinsic Spin Hall Effect". arxiv.org:cond-mat/0504353 (2005).

[6] J.-C. Charlier, X. Gonze and J.-P. Michenaud. "Graphite Interplanar Bonding: Electronic Delocalization and van der Waals Interaction". EPL, **28**, 6 (1994).

[7] A C. Neto, F. Guinea and N. M. Peres. "Drawing conclusions from graphene". Physics World, **19**, 11 (2006).

[8] Daniel R. Cooper, Benjamin D'Anjou, Nageswara Ghattamaneni, Benjamin Harack, Michael Hilke, Alexandre Horth, Norberto Majlis, Mathieu Massicotte, Leron Vandsburger, Eric Whiteway, and Victor Yu. "Experimental Review of Graphene". Condensed Matter Physics, **2012**, 501686 (2012).

[9] K. S. Novoselov, Z. Jiang, Y. Zhang, S. V. Morozov, H. L. Stormer, U. Zeitler,J. C. Maan,G. S. Boebinger, P. Kim, and A. K. Geim. "Room-Temperature Quantum Hall Effect in Graphene". **315**,5817, 1379 (2007).

[10] Tomasz M. Rusin and Wlodek Zawadzki. "Theory of electron Zitterbewegung in graphene probed by femtosecond laser pulses". Phys. Rev. B **80**, 045416 (2009).

[11] Neil W. Ashcroft and N. David Mermin. "Solid State Physics". Holt,Rinehart and Winston, 826 pp (1976).

[12] Dante Gatteschi and Roberta Sessoli. "Quantum Tunneling of Magnetization and Related Phenomena in Molecular Materials". Angew.Chem.Int. **42**, 3 (2003).

[13] A. K. Geim and I. V. Grigorieva. "Van der Waals heterostructures". Nature **499**, 419–425(2013).

[14] M.I. Katsnelson, K.S. Novoselov and A.K. Geim. "Chiral tunnelling and the Klein paradox in graphene". Nature Physics, **2**, 620-625 (2006).

[15] P. R. Wallace. "The Band Theory of Graphite". Phys. Rev. **71**.622 (1947).

[16] Germain Salvato-Vallverdu (2014, April). "Bands diagram using VASP and pymatgen". Retrieved from http://gvallver.perso.univ-pau.fr/?p=587.

[17] G.W. Semenoff. "Condensed-Matter Simulation of a Three-Dimensional Anomaly". Phys. Rev. Lett. **53**, 2449 (1984).

[18] E. McCann, K. Kechedzhi, Vladimir Falko, H. Suzuura, T. Ando and B.L. Althuler. "Weak-Localization Magnetoresistance and Valley Symmetry in Graphene". Phys. Rev. Lett. **97**, 146805 (2006).

[19] F. V. Tikhonenko, D. W. Horsell, R. V. Gorbachev, and A. K. Savchenko. "Weak Localization in Graphene Flakes". Phys. Rev. Lett. **100**, 056802 (2008).

[20] James Shackelford. "Introduction to Materials Science for Engineers". Pearson Prentice Hall (2009).

[21] Vitor M. Pereira, J. M. B. Lopes dos Santos, and A. H. Castro Neto. "Modeling disorder in graphene". Phys. Rev. B **77**, 115109 (2007).

[22] N. D. Mermin and H. Wagner. "Absence of Ferromagnetism or Antiferromagnetism in One- or Two-Dimensional Isotropic Heisenberg Models". Phys. Rev. Lett. **17**, 1133 (1966).

[23] P. C. Hohenberg. "Existence of Long-Range Order in One and Two Dimensions". Phys. Rev. **158**, 383 (1967).

[24] Oleg V. Yazyev and Steven G. Louie. "Topological defects in graphene: Dislocations and grain boundaries". Phys. Rev. B **81**, 195420 (2010).

[25] Ovidiu Cretu, Arkady V. Krasheninnikov, Julio A. Rodríguez-Manzo, Litao Sun, Risto M. Nieminen, and Florian Banhart. "Migration and Localization of Metal Atoms on Strained Graphene". Phys. Rev. Lett. **105**, 196102 (2010).

[26] Oleg V. Yazyev and Lothar Helm . "Defect-induced magnetism in graphene". Phys. Rev. B **75**, 125408 (2007).

[27] P. Esquinazi, D. Spemann, R. Höhne, A. Setzer, K.-H. Han, and T. Butz. "Induced Magnetic Ordering by Proton Irradiation in Graphite". Phys. Rev. Lett. **91**, 227201 (2003).

[28] Ricardo Faccio, Luciana Fernández-Werner, Helena Pardo, Cecilia Goyenola, Oscar N. Ventura Álvaro W. Mombrú. "Electronic and structural distortions in graphene induced by carbon vacancies and boron doping". arxiv:cond-mat.mtrl-sci/1006.0589.

[29] . M. Gallouze, A. Kellou, , M. Drir. "Electronic and magnetic properties of adsorbed H2 on graphene with atomic defects: Ab initio study". Physica E: Low-dimensional Systems and Nanostructures **52**, 127-135 (2013).

[30] Jayeeta Lahiri, You Lin, Pinar Bozkurt, Ivan I. Oleynik Matthias Batzill. "An extended defect in graphene as a metallic wire". Nature Nanotechnology **5**, 326-329 (2010).

[31] Feng Ding. "Theoretical study of the stability of defects in single-walled carbon nanotubes as a function of their distance from the nanotube end". Phys. Rev. B **72**, 245409 (2005).

[32] E. H. Åhlgren, S. K. Hämäläinen, O. Lehtinen, P. Liljeroth, and J. Kotakoski. "Structural manipulation of the graphene/metal interface with Ar+ irradiation". Phys. Rev. B **88**, 155419 (2013).

[33] Aurélien Lherbier, Simon M.-M. Dubois, Xavier Declerck, Yann-Michel Niquet, Stephan Roche, and Jean-Christophe Charlier. "Transport properties of graphene containing structural defects". Phys. Rev. B **86**, 075402 (2012).

[34] K. Suenaga, H. Wakabayashi,M. Koshino,Y. Sato,K. Urita,S. Iijima. "Imaging active topological defects in carbon nanotubes". Nature Nanotechnology **2**, 358-360 (2007).

[35] Miguel M. Ugeda, Iván Brihuega, Fanny Hiebel, Pierre Mallet, Jean-Yves Veuillen, José M. Gómez-Rodríguez, and Félix Ynduráin. "Electronic and structural characterization of divacancies in irradiated graphene". Phys. Rev. B **85**, 121402 (2012).

[36] C. Meyer,C. Kisielowski,R. Erni,M. Rossell,M. F. Crommie, and A. Zettl. "Direct Imaging of Lattice Atoms and Topological Defects in Graphene Membranes". Nano Lett., **8**, 3582–3586 (2008).

[37] A.J. Stone, D.J. Wales.*Theoretical studies of icosahedral C60 and some related species.* Chem. Phys. Letters. **128**, 501-503 (1986).

[38] Daniel Huertas-Hernando, F. Guinea, and Arne Brataas. "Spin-orbit coupling in curved graphene, fullerenes, nanotubes, and nanotube caps". Phys. Rev. B **74**, 155426 (2006).

[39] Jie Ma, Dario Alfè, Angelos Michaelides, and Enge Wang. "Stone-Wales defects in graphene and other planar sp2-bonded materials". Phys. Rev. B **80**, 033407 (2009).

[40] S. Haldar, R. Amorim, B. Sanyal, R. Scheicher, A. Rocha. "Energetic stability, STM fingerprints and electronic transport properties of defects in graphene and silicene". RCS Adv. **6**, 6702 (2016).

[41] Han Liu,Adam T. Neal,Zhen Zhu,Zhe Luo,Xianfan Xu,David Tománek,Peide D. Ye. "Phosphorene: An Unexplored 2D Semiconductor with a High Hole Mobility". ACS Nano, 2014, **8**, 4033–4041 (2014).

[42] Pengke Li and Ian Appelbaum. "Electrons and holes in phosphorene". Phys. Rev. B **90**, 115439 (2014) .

[43] H. Fang. et al. "Degenerate n-doping of few-layer transition metal dichalcogenides by potassium". Nano Lett. **13**, 1991-1995 (2013).

[44] A.S. Rodin, A. Carvalho, and A.H. Castro Neto. "Strain-Induced Gap Modification in Black Phosphorus". Phys. Rev. Lett. **112**, 176801 (2014).

[45] Qing Hua Wang, Kourosh Kalantar-Zadeh, Andras Kis, Jonathan N. Coleman, and Michael S. Strano. "Electronics and optoelectronics of two-dimensional transition metal dichalcogenides". Nature Nanotechnology **7**, 699–712 (2012).

[46] Deep Jariwala, Vinod K. Sangwan, Lincoln J. Lauhon, Tobin J. Marks, and Mark C. Hersam. "Emerging Device Applications for Semiconducting Two-Dimensional Transition Metal Dichalcogenides". ACS Nano, **8**,1102–1120 (2014).

[47] Tianyi Cai, Shengyuan A. Yang, Xiao Li, Fan Zhang, Junren Shi, Wang Yao, and Qian Niu. "Magnetic control of the valley degree of freedom of massive Dirac fermions with application to transition metal dichalcogenides". Phys. Rev. B **88**, 115140 (2013).

[48] Gui-Bin Liu, Wen-Yu Shan, Yugui Yao, Wang Yao, and Di Xiao. "Three-band tight-binding model for monolayers of group-VIB transition metal dichalcogenides". Phys. Rev. B **88**, 085433 (2013).

[49] Timothy C. Berkelbach, Mark S. Hybertsen, and David R. Reichman. "Theory of neutral and charged excitons in monolayer transition metal dichalcogenides". Phys. Rev. B **88**, 045318 (2013).

[50] Jingsi Qiao, Xianghua Kong, Zhi-Xin Hu, Feng Yang Wei Ji. "High-mobility transport anisotropy and linear dichroism in few-layer black phosphorus". Nature Communications **5**, 4475 (2014).

[51] Igor Žutić, Jaroslav Fabian, and S. Das Sarma. "Spintronics: Fundamentals and applications". Rev. Mod. Phys. **76**, 323 (2004).

[52] Chih-Pin Lu, Guohong Li, K. Watanabe, T. Taniguchi, and EvaY. Andrei. "MoS2: Choice Substrate for Accessing and Tuning the Electronic Properties of Graphene". Phys. Rev. Lett. **113**, 156804 (2013).

[53] Andrea Splendiani, Liang Sun, Yuanbo Zhang, Tianshu Li, Jonghwan Kim, Chi-Yung Chim, Giulia Galli and Feng Wang. "Emerging Photoluminescence in Monolayer MoS2". Nano Lett.**10**, 1271–1275 (2010).

[54] Andor Kormányos,Guido Burkard,Martin Gmitra,Jaroslav Fabian,Viktor Zólyomi,Neil Drummond,Vladimir Falko. "k.p theory for two-dimensional transition metal dichalcogenide semiconductors". 2D Mater. **2** 049501 (2015).

[55] A. Molina-Sánchez and L. Wirtz. "Phonons in single-layer and few-layer MoS2 and WS2". Phys. Rev. B **84**, 155413 (2011).

[56] Th. Böker, R. Severin, A. Müller, C. Janowitz, R. Manzke, D. Voß, P. Krüger, A. Mazur, and J. Pollmann. "Band structure of MoS2, MoSe2, and MoTe2: Angle-resolved photoelectron spectroscopy and ab initio calculations". Phys. Rev. B **64**, 235305 (2001).

[57] Di Xiao, Gui-Bin Liu, Wanxiang Feng, Xiaodong Xu, and Wang Yao. "Coupled Spin and Valley Physics in Monolayers of MoS2 and Other Group-VI Dichalcogenides". Phys. Rev. Lett. **108**, 196802 (2012).

[58] R. Roldán,M. López-Sancho,F. Guinea,E. Cappelluti,J. Silva-Guillén,P. Ordejón. "Momentum dependence of spin–orbit interaction effects in single-layer and multi-layer transition metal dichalcogenides". 2D Materials **1**, 3 (2014).

[59] http://www.cs.utexas.edu/ fussell/courses/cs352h/papers/moore.pdf.

[60] J.E. Padilha, A. Fazzio, and Antônio J.R. da Silva. "van der Waals Heterostructure of Phosphorene and Graphene: Tuning the Schottky Barrier and Doping by Electrostatic Gating". Phys. Rev. Lett. **114**, 066803 (2015).

[61] Yongqing Cai, Gang Zhang, and Yong-Wei Zhang. "Electronic Properties of Phosphorene/Graphene and Phosphorene/Hexagonal Boron Nitride Heterostructures". J. Phys. Chem. C **119**, 13929–13936 (2015).

[62] Keun Su Kim, Andrew L. Walter, Luca Moreschini, Thomas Seyller, Karsten Horn, Eli Rotenberg and Aaron Bostwick. "Coexisting massive and massless Dirac fermions in symmetry-broken bilayer graphene". Nature Materials **12**, 887–892 (2013).

[63] Martin Gmitra and Jaroslav Fabian. "Graphene on transition-metal dichalcogenides: A platform for proximity spin-orbit physics and optospintronics". Phys. Rev. B **92**, 155403 (2015).

[64] Max Born, J. Robert Oppenheimer. "Zur Quantentheorie der Molekeln". Annalen der Physik **389**,457-484 (1927).

[65] ttp://itp.uni-frankfurt.de/ valenti/CHAP3.pdf

[66] Handy N. C. and Lee A. M. "The adiabatic approximation". Chem. Phys. Lett. **252**, 425-430, (1996).

[67] L. Thomas. "The calculation of atomic fields". Proc. Cambridge Phil. Soc. **23**,542-548 (1927).

[68] E. Fermi. "Un Metodo Statistico per la Determinazione di alcune Priorprieta dell'Atomo". Rend. Accad. Naz. Lincei. **6**, 602-607 (1927).

[69] Klaus Capelle. "A bird's-eye view of density-functional theory". arXiv:cond-mat/0211443 (2002)

[70] Michel Le Bellac, Fabrice Mortessagne and G. George Batrouni. "Equilibrium and Non Equilibrium Statistical Thermodynamics". University Press, Cambridge (2004).

[71] P. Hohenberg and W. Kohn. "Inhomogeneous Electron Gas". Phys. Rev. **136**, B864 (1964).

[72] W. Kohn and L. J. Sham. "Self-Consistent Equations Including Exchange and Correlation Effects". Phys. Rev. **140**, A1133 (1965).

[73] John P. Perdew, Kieron Burke, and Matthias Ernzerhof. "Generalized Gradient Approximation Made Simple". Phys. Rev. Lett. **77**, 3865 (1996).

[74] J. Soler, E. Artacho, J. Gale, A. Garcia, J. Junquera,P. Ordejon, and D. Sanchez-Portal. "The SIESTA method for ab initio order-N materials simulation". J. Phys. Condens. Matter **14**, 2745 (2002).

[75] James C. Phillips and Leonard Kleinman. "New Method for Calculating Wave Functions in Crystals and Molecules". Phys. Rev. **116**, 287 (1959).

[76] A. Zunger, M. Cohen. Phys. Rev. B **18**, 5449.

[77] L. Kleinman, D. Bylander. Phys. Rev. Lett. **48**. 1425.

[78] L. Fernández-Seivane,M. Oliveira,S. Sanvito,J. Ferrer. "On-site approximation for spin–orbit coupling in linear combination of atomic orbitals density functional methods". J. Phys.: Condens. Matter **19**, 489001 (2006).

[79] Jorge Kohanoff. ”Electronic Structure Calculations for Solids and Molecules: Theory and Computational Methods”. Cambridge (2006).

[80] R. P. Feynman. ”Forces in Molecules”. Phys. Rev. **56**, 340 (1939).

[81] Hendrik J. Monkhorst and James D. Pack. ”Special points for Brillouin-zone integrations”. Phys. Rev. B **13**, 5188 (1976).

[82] J. Sakurai. ”Modern Quantum Mechanics”. Revised Edition. Pearson Education (1994).

[83] Lok C. Lew Yan Voon,Morten Willatzen. ”The k.p Method:Electronic Properties of Semiconductors”. Springer-Verlag Berlin Heidelberg (2009).

[84] H. Ebert, H. Freyer, and M. Deng. ”Manipulation of the spin-orbit coupling using the Dirac equation for spin-dependent potentials”. Phys. Rev. B **56**, 9454 (1997).

[85] B. H. Bransden, Charles Jean Joachain. ”Physics of Atoms and Molecules”. Prentice Hall (2003).

[86] Leonard Kleinman. ”Density functional for noncollinear magnetic systems”. Phys. Rev. B **59**, 3314 (1999).

[87] D.M. Ceperley and B.J. Alder. ”Ground State of the Electron Gas by a Stochastic Method”. Phys. Rev. Lett. **45**, 556 (1980).

[88] J.C. Charlier, P.C. Eklund, J. Zhu and A.C. Ferrari. ”Electron and Phonon Properties of Graphene: Their Relationship with Carbon Nanotubes”.
www-g.eng.cam.ac.uk/nms/publications/pdf/Charlier$_BOOK2008.pdf$.

[89] Andres Castellanos-Gomez, Leonardo Vicarelli, Elsa Prada, Joshua O. Island, K.L. Narasimha-Acharaya, Sofya I. Blanter, Dirk J. Groenendijk, Michele Buscema, Gary A. Steele, and J.V. Alvarez. ”Isolation and characterization of few-layer black phosphorus”. 2D Materials, **1**, 2 (2014).

Appendix A

Dirac equation for a Central potential

In order to introduce relativistic corrections to the SIESTA code, we need to explain some details related to the spin-orbit coupling in the Dirac equation and after that make the link between its role in the construction of the Pseudo-potentials used in the numerical computation.

First of all, we define a set of quantities that are conserved for the Dirac equation. We have to remember that now we are in the relativistic case and we need one more quantity to classify the states of the Dirac Hamiltonian. Besides the operators $\hat{H}$,$\hat{J}^2$, and $\hat{J}_z$, in the four dimensional space-time, another quantity is needed such that it commutes with the three operators above, such a quantity is

$$\hat{K} = \beta\hat{\Sigma} \cdot \hat{L} - \frac{\hbar}{2}\beta = \beta(\hat{\Sigma} \cdot \hat{L} + \hbar\hat{I}) \tag{A.1}$$

this is the so-called $Spin - Orbit$ Coupling operator which fulfil the conditions required, where β is coming from the Dirac equation

$$\hat{H} = c\vec{\alpha} \cdot \hat{p} + \beta mc^2 \tag{A.2}$$

$\hat{L}$ is the orbital momenta operator and $\hat{\Sigma}$ is proportional to spin operator by a constant $\hbar/2$

$$\vec{S} = \frac{\hbar}{2}\Sigma \tag{A.3}$$

which is actually a 4×4 matrix since we are dealing with the Dirac equation. We also remember that in this case just orbital momentum or spin operators are not good quantum number by themselves, and it's taken the total angular moment instead, defined as $\hat{J} = \hat{L} + \hat{S}$.

If we square the SOC operator, we find

$$\hat{K}^2 = \vec{L} + \hbar\hat{\Sigma} \cdot \hat{L} + \frac{3}{4}\hbar^2 + \frac{1}{4}\hbar^2 = \hat{J}^2 + \frac{1}{4}\hbar^2 \tag{A.4}$$

this defines a relation between the eigenvalue of the SOC operator $\hat{\Sigma}$ and the j eigenvalue of the total angular momentum operator

$$\hbar^2\kappa^2 = \hbar^2 j(j+1) + \frac{1}{4}\hbar^2 \rightarrow \kappa^2 = (j + 1/2)^2 \tag{A.5}$$

this leads to the eigenvalues of the SOC operator

$$\kappa = \pm(j + \frac{1}{2}) \tag{A.6}$$

Now we have a set in which we can defined conserved magnitudes in order to obtain the spectrum of the Hamiltonian, going back to the Dirac equation under a central potential

$$[c\vec{\alpha} \cdot \vec{p} + \beta mc^2 + V(\vec{r})]\Psi = E\Psi \tag{A.7}$$

such a Hamiltonian hold the commutation relation with both $\hat{J}$ and $\hat{K}$. Taking the radial and angular solutions for the Dirac equation, we write down its new form

$$\begin{pmatrix} V(\vec{r}) + mc^2 - E & c\vec{\alpha} \cdot \vec{p} \\ \vec{\alpha} \cdot \vec{p} & V(\vec{r}) - mc^2 - E \end{pmatrix} \begin{pmatrix} g(\vec{r})\chi_{jl}^m \\ -f(\vec{r})(\frac{\vec{\sigma} \cdot \vec{r}}{r})\chi_{jl}^m \end{pmatrix} = 0 \tag{A.8}$$

The relation between the eigenvalues κ and j found before, allows to simplify the problem and write the following coupled differential equation

$$-\hbar c\frac{df}{dr}+\frac{\hbar c(\kappa-1)}{r}f(\vec{r})=(E-mc^2-V(\vec{r}))g(\vec{r}) \tag{A.9}$$

$$-\hbar c\frac{dg}{dr}+\frac{\hbar c(\kappa+1)}{r}f(\vec{r})=(E+mc^2-V(\vec{r}))f(\vec{r}) \tag{A.10}$$

where the angular parts χ were suppressed. This equation can be written in a more compact fashion defining, $F(\vec{r})=rf(\vec{r})$ and $G(\vec{r})=rg(\vec{r})$ obtaining

$$\frac{df}{dr}=\frac{d}{dr}\frac{F(\vec{r})}{r}=\frac{1}{r}\frac{dF}{r}-\frac{1}{r^2}F(\vec{r}) \tag{A.11}$$

where F and G are called major and minor solutions for the radial Dirac equation. Calling $\lambda=1/mc^2$ and $\varepsilon=E-\lambda^{-2}$, the coupled differential equations describing the radial Dirac equation under a central potential (and also will be used for the creation of the pseudo potentials) are written as

$$\frac{dF}{dr}-\frac{\kappa}{r}F(r)+(\varepsilon-V(r))\lambda G(r)=0 \tag{A.12}$$

$$\frac{dG}{dr}+\frac{\kappa}{r}G(r)-(\frac{2}{\lambda^2}+\varepsilon-V(r))\lambda F(r)=0. \tag{A.13}$$

Appendix B

Kramer's theorem for spinful electrons

Here we consider how the electron-spin state changes under the time reversal symmetry. Let the Hamiltonian $\hat{H}$ be invariant under time reversal

$$[\hat{H}, \hat{\Theta}] = 0, \tag{B.1}$$

If we have that $|\psi_{k,s}\rangle$ and $\hat{\Theta}|\psi_{k,s}\rangle = |\psi_{-k,-s}\rangle$ are the simultaneous eigenvector of $\hat{H}$ (with eigenvalue E) and $\hat{S}_z$ (which means that the Hamiltonian and the spin operator commute), and its time reversed state respectively, then

$$\hat{H}\hat{\Theta}|\psi_{k,s}\rangle = \hat{\Theta}\hat{H}|\psi_{k,s}\rangle = E_{k,s}\hat{\Theta}|\psi_{k,s}\rangle = E_{k,s}|\psi_{-k,-s}\rangle \tag{B.2}$$

We have now that $\hat{\Theta}|\psi_{k,s}\rangle$ is also eigenvector of $\hat{H}$ with the same eigenvalue E. When we square $\hat{\Theta}^2 = -1$ (half integer spin), $\hat{\Theta}|\psi_{k,s}\rangle$ and $|\psi_{k,s}\rangle$ are orthogonal. This means that the original state ψ and its time reversed counterpart must correspond to distinct states, which means that they are degenerate, this is the so-called *Kramers* theorem, in order to prove that we use

$$\langle\tilde{\beta}|\tilde{\alpha}\rangle = \langle\alpha|\beta\rangle = \langle\beta|\alpha\rangle^* \tag{B.3}$$

where $|\alpha\rangle = \hat{\Theta}\,|\psi_{k,s}\rangle$, $|\tilde{\alpha}\rangle = \hat{\Theta}\,|\alpha\rangle = \hat{\Theta}(\hat{\Theta}\,|\psi_{k,s}\rangle) = \hat{\Theta}^2\,|\psi_{k,s}\rangle$, and $|\beta\rangle = |\psi_{k,s}\rangle$,$|\tilde{\beta}\rangle = \hat{\Theta}\,|\psi_{k,s}\rangle = |\alpha\rangle$. Since $\hat{\Theta}^2\,|\psi_{k,s}\rangle = -\,|\psi_{k,s}\rangle$, we have that $|\tilde{\alpha}\rangle = \hat{\Theta}^2\,|\psi_{k,s}\rangle = -\,|\psi_{k,s}\rangle$. Then we find

$$\langle\tilde{\beta}|\tilde{\alpha}\rangle = -\,\langle\alpha|\beta\rangle = \langle\alpha|\beta\rangle\,, \tag{B.4}$$

or

$$\langle\alpha|\psi_{k,s}\rangle = 0, \tag{B.5}$$

which means that for spinful electrons, time-reversed states are orthogonal. This result has to do with the opposite gaps generated in graphene once the SOC is taken into account.

Appendix C

$k \cdot p$ Approximation

Here we are going to explain some details on the $k \cdot p$ approach, which is going to elucidate some results that we've got taken from our ab-initio calculations. We start from an easy derivation of the $k \cdot p$ Hamiltonian and how this is related to our work.

The $k \cdot p$ equation is obtain from the one-electron Schrodinger equation

$$H\psi_{n\vec{k}}(\vec{r}) = E_n(\vec{k})\psi_{n\vec{k}}(\vec{r}) \tag{C.1}$$

from the Bloch theorem we can write the ψ wave functions as the product of a plane wave times a periodic function which has the periodicity of the lattice

$$\psi_{n\vec{k}}(\vec{r}) = e^{i\vec{k}\cdot\vec{r}}u_{n\vec{k}}(\vec{r}) \tag{C.2}$$

Let the Hamiltonian only consists of the kinetic-energy operator,a local periodic crystal potential, and the spin-orbit interaction term

$$H = \frac{p^2}{2m_0} + V(\vec{r}) + \frac{\hbar}{4m_0^2c^2}(\vec{\sigma} \times \nabla V) \cdot \vec{p} \tag{C.3}$$

Then using the Bloch Theorem in reciprocal space we have

$$H(\vec{k})u_{n\vec{k}} = \mathcal{E}_n(\vec{k})u_{n\vec{k}} \tag{C.4}$$

where now the Hamiltonian is written as

$$H(\vec{k}) = H + H_{k\cdot p} \tag{C.5}$$

$$H_{k\cdot p} = \frac{\hbar}{m_0}\vec{k}\cdot\vec{\pi} \tag{C.6}$$

$$\vec{\pi} = \vec{p} + \frac{\hbar}{4m_0c^2}(\vec{\sigma}\times\nabla V) \tag{C.7}$$

and

$$\mathcal{E}_n(\vec{k}) = E_n(\vec{k}) - \frac{\hbar^2k^2}{2m_0} \tag{C.8}$$

this is why this approach is known as $k\cdot p$, since it has the Hamiltonian proportional to that term which will be taken as a perturbation in order to obtain analytical expressions for the bands near the High symmetry points. If the states $u_{n\vec{k}}$ form a complete set of periodic functions, then a representation of $H(\vec{k})$ in this basis is exact, this means that a diagonalization of this matrix

$$\langle u_{n'\vec{k}}|H(\vec{k})|u_{m\vec{k}}\rangle \tag{C.9}$$

leads to the dispersion relation throughout the whole Brillouin zone. Particularly for the High Symmetry points, such an approximations is good if the semiconductor under study has a fairly isolated band-at least for a finite region in k space. For instance, this is what happens for our phosphorene and MoTe$_2$ systems indeed, where the band gap is located at very specific points in the Brillouin zone, then

$$\frac{\partial E_n(\vec{k_0})}{\partial k_i} = 0 \tag{C.10}$$

and it's allowed for us to make an expansion around these points, taking the $k\cdot p$ factor as a perturbation. Here we are not going through the details and just mention the main results that we can obtain from such a procedure. Starting from the perturbation correction, at the order we choose, we can obtain the relation dispersion and its accuracy will depend on how we choose the order of the perturbation, it is worth mentioning that the more we go into the expansion the more bands we need to add to calculation, and this can be seen from

$$E_n(\vec{k}) = E_n(\vec{k_0}) + \frac{\hbar^2 k^2}{2m_0} + \frac{\hbar \vec{k}}{m_0} \cdot \langle n\vec{k_0}|\vec{\pi}|n\vec{k_0}\rangle + \frac{\hbar^2}{m_0^2} \sum_l \frac{|\langle n\vec{k_0}|\vec{\pi}|l\vec{k_0}\rangle \cdot \vec{k}|^2}{E_n(\vec{k_0}) - E_l(\vec{k_0})} \tag{C.11}$$

where this expansion was made up to second order.

With the approach explained previously we can find the new parameters involved in the bilayer systems made of Graphene and MoTe$_2$, here we'll explain briefly how the calculation was performed for the system where only was the TDMC monolayer, and because the bilayer still has the same group symmetry in the unit cell, we can find an expansion around the K point, which is a point that only has contributions coming from the MoTe$_2$, a result that is shown in the orbital projections in section 4.5. We neglect all the procedure directly related to the calculation of the matrix for the so-called seven band $k \cdot p$ model, and start from the expressions for the valence and conduction bands, we just take into account these bands because they are of main importance in electronic properties, then the eigenvalues of the low energy Hamiltonian read

$$E_{\pm} = E_F + (\frac{\hbar^2}{2m_e} + \frac{\alpha + \beta}{2})q^2 \pm \sqrt{(\frac{E_g}{2} + \frac{\beta - \alpha}{2}q^2)^2 + f(\vec{q})} \tag{C.12}$$

with

$$f(\vec{q}) = |\gamma|^2 q^2 + |q|^3 |\gamma||\kappa| 2cos(\theta_{\kappa,\gamma} + 3\varphi_q) + q^4[|\kappa|^2 - |\gamma||\eta|cos(\theta_{\eta,\gamma})]$$

where E_F is where the Fermi level lies, E_g is the gap between conduction and valence bands, θ are the relative phases between κ and γ, and η and γ, φ is the angle between the vectors in reciprocal space which is in the plane $q_x - q_y$, the signs $+$ and $-$ correspond to the conduction and valence bands. Since the dependence of the energy on the reciprocal vectors is non-linear, we can first take the parameters

$|\gamma|$, α and β to determine, saying that for small $\vec{q}$ the largest energy scale under the square root is the band gap, then

$$E_+ \simeq \tilde{\epsilon}_{cb} + (\frac{\hbar^2}{2m_e} + \beta + \frac{|\gamma|^2}{E_g})q^2$$

$$E_- \simeq \tilde{\epsilon}_{vb} + (\frac{\hbar^2}{2m_e} + \alpha - \frac{|\gamma|^2}{E_g})q^2 \tag{C.13}$$

then if we take as a first approximation the dispersion on conduction and valence bands as parabolic function on the vectors $\vec{q}$, from the DFT results we can obtain by fitting the value of the effective reciprocal masses m_{vb} and m_{cb}, which describe the following

$$E_+ = \frac{\hbar^2 q^2}{2m_{cb}}, \qquad E_- = \frac{\hbar^2 q^2}{2m_{vb}} \tag{C.14}$$

Now if we take an approximation for the valence and conduction bands written as

$$E_F + c_1 q^2 \pm \sqrt{\frac{E_g^2}{2} + c_2 q^2} \tag{C.15}$$

and looking for the best fit that this function along a short range around the K point can give, we can find the relation between the constants c_1 and c_2 with the three parameters taken at first, the relations are

$$\frac{\alpha + \beta}{2} = c_1 - \frac{\hbar^2}{2m_e} \tag{C.16}$$

$$\frac{\beta - \alpha}{2} + |\gamma|^2 = \frac{2c_2}{E_g} \tag{C.17}$$

Now we have the three first parameters, we can take an expansion up to fourth order , and similarly to the function involving the constants c_1 and c_2, we can write a function to fit

$$E_F + c_1 q^2 \pm \sqrt{\frac{E_g^2}{4} + c_2 q^2 + c_3 |q|^3 cos 3\phi_q + c_4 q^4} \tag{C.18}$$

where the plus and minus signs are for the conduction and valence bands. Now we need to take care about the non isotropy in the bands once we take the paths $\Gamma - K$

and $K-M$, the fitting is made in a larger region than in the previous case for the parabolic case in order to obtain the values of c_3 and c_4, and the values that $cos3\phi_q$ takes are 1 for $K-M$ and -1 for $\Gamma-K$. Once we already now the values of α,β,$|\gamma|$,c_1 and c_2, the values for the parameters κ and η are obtained from the following relations

$$\kappa=\frac{c_3}{2|\gamma|}, \qquad \eta=[\frac{(\beta-\alpha)^2}{4}-c_4]/|\gamma| \tag{C.19}$$

In this way, the parameters related to the low energy Hamiltonian can be obtained and we can compare the parameters obtained from a different system such as the bilayer, and how they are changed with respect to the parameters obtained in reference [54] for the monolayer case.